Metal-Organic Frameworks (MOFs) Based on Fluorinated Trimesate Linkers

Inaugural-Dissertation

zur

Erlangung des Doktorgrades

der Mathematisch-Naturwissenschaftlichen Fakultät

der Universität zu Köln

vorgelegt von

Susanna Wenzel

aus Bad Wildungen

Berichterstatter (Gutachter):	Prof. Dr. Uwe Ruschewitz
	Prof. Dr. Mathias Wickleder
Vorsitzende	Prof.'in Dr. Katharina Groß
Schriftführerin:	Dr.'in Corinna Hegemann

Tag der mündlichen Prüfung: 30.10.2024

»It's always darkest before the dawn.«

Abstract

This dissertation explores the preparation and characterisation of fluorinated Metal-Organic Frameworks (MOFs) incorporating divalent zinc, copper, and cobalt cations. Furthermore, the influence of the degree of fluorination on the resulting structures, thermal stabilities, and sorption behaviours of these MOFs was investigated. For this purpose, stepwise fluorinated trimesate linkers (*mF*-/*dF*-BTC^{3-}) derived from benzene-1,3,5-tricarboxylic acid (H_3BTC) were used.

A notable highlight of this work is the synthesis of Zn-UoC-7(1F)[1] and Zn-UoC-7(2F)[1], which are the first anionic MOFs based on fluorinated trimesate linkers. Both MOFs were characterised using single-crystal X-ray diffraction. Their crystal structures show large channels along [001], which accommodate the counter cations ($(CH_3)_2NH_2^+$) as well as solvent molecules. Notably, the $(CH_3)_2NH_2^+$ cations compensating their anionic frameworks were localised and refined. Surface areas (S_{BET}) of 2740 m^2/g (Zn-UoC-7(1F)) and 1643 m^2/g (Zn-UoC-7(2F)) were obtained from N_2 sorption measurements. Moreover, both MOFs exhibit high CO_2 uptakes, with Zn-UoC-7(1F) showing a lower uptake compared to Zn-UoC-7(2F). Remarkably, Zn-UoC-7(2F) achieves an exceptionally high CO_2 uptake of 247 cm^3/g at 273 K, which is among the highest values reported for MOFs to date.[2]

The analysis of their thermal behaviour revealed that a higher degree of fluorination of these MOFs is likely associated with decreased thermal stability. It was generally observed that the decomposition temperatures of anionic MOFs are more difficult to determine, which is attributed to the simultaneous release of uncoordinated solvent molecules and the decomposition of both the cations and the frameworks.

Amongst others, the aforementioned results have been published as a hot paper in *Chemistry – A European Journal*.[1]

In addition, several other anionic MOFs were successfully synthesised and analysed, including the isostructural Co-UoC-7(2F), UoC-13(1F), and GaMOF-1(1F).

Furthermore, the bimetallic MOFs Cu,Zn-UoC-5(1F) and Co,Zn-UoC-5(1F), featuring neutral frameworks, were structurally investigated and compared to Zn-UoC-5(1F)[3]. Their isostructural difluorinated derivatives Cu,Zn-UoC-5(2F)[4] and Co,Zn-UoC-5(2F) were synthesised as phase-pure powders.

A notable aspect of the UoC-5 structure is the presence of two SBUs: a paddlewheel unit $M(COO)_4$ (M = Zn, Cu, Co) and an octahedral $Zn_4O(COO)_6$ unit. Furthermore, the structure possesses channels along [111] and for Cu,Zn-UoC-5(1F) and Cu,Zn-UoC-5(2F) surface areas (S_{BET}) of of 1760 m^2/g (Cu,Zn-UoC-5(1F)) and 1400 m^2/g (Cu,Zn-UoC-5(2F)) were calculated from N_2 sorption measurements, respectively.

Kurzzusammenfassung

Diese Dissertation untersucht die Synthese und Charakterisierung fluorierter Metall-Organischer Gerüstverbindungen (MOFs), die zweiwertige Zink-, Kupfer- und Cobalt-Kationen enthalten. Darüber hinaus wurde der Einfluss des Fluorierungsgrads auf die resultierende Struktur, auf die thermische Stabilität und auf das Sorptionsverhalten dieser MOFs untersucht. Zu diesem Zweck wurden schrittweise fluorierte Trimesat-Linker (*mF-*/*dF*-BTC^{3-}), abgeleitet von Benzol-1,3,5-tricarbonsäure (H_3BTC), verwendet.

Ein zentrales Ergebnis dieser Arbeit ist die Synthese von Zn-UoC-7(1F)[1] und Zn-UoC-7(2F)[1], die die ersten anionischen MOFs auf Basis fluorierter Trimesat-Linker darstellen. Beide MOFs wurden mittels Einkristall-Röntgenbeugung charakterisiert. Ihre Kristallstrukturen zeigen große Kanäle entlang der [001]-Richtung, in denen sich sowohl die Gegenkationen ($(CH_3)_2NH_2^+$) als auch die Lösungsmittelmoleküle aus der Synthese aufhalten. Bemerkenswerterweise konnten die $(CH_3)_2NH_2^+$-Kationen, die die anionischen Gerüste kompensieren, in den Strukturlösungen beider MOFs lokalisiert und verfeinert werden.

Spezifische Oberflächen (S_{BET}) von 2740 m^2/g (Zn-UoC-7(1F)) und 1643 m^2/g (Zn-UoC-7(2F)) wurden durch N_2-Sorptionsmessungen ermittelt und beide MOFs zeigen hohe CO_2-Aufnahmekapazitäten, wobei Zn-UoC-7(2F) eine höhere aufweist als Zn-UoC-7(1F). Mit einer CO_2-Aufnahme von 247 cm^3/g bei 273 K ist es sogar einer der höchsten bisher berichteten Werte für MOFs.[2]

Weiterhin weist die Analyse ihres thermischen Verhaltens darauf hin, dass ein höherer Fluorierungsgrad, die thermische Stabilität dieser MOFs verringert. Es konnte dabei beobachtet werden, dass die Zersetzungstemperatur anionischer MOFs schwierig zu bestimmen ist, da im gleichen Temperaturbereich unkoordinierte Lösungsmittelmoleküle freigesetzt werden und sowohl die Kationen als auch die Gerüste sich zu zersetzen beginnen.

Die oben beschriebenen Ergebnisse wurden mit weiteren als Hot Paper in *Chemistry – A European Journal* veröffentlicht.[1]

Des Weiteren konnten weitere anionische MOFs, einschließlich des isostrukturellen Kobalt-Analogons Co-UoC-7(2F), UoC-13(1F) und GaMOF-1(1F), erfolgreich synthetisiert und analysiert werden.
Außerdem wurden MOFs mit neutralen Gerüsten, die bimetallischen Cu,Zn-UoC-5(1F) und Co,Zn-UoC-5(1F), strukturell untersucht und mit Zn-UoC-5(1F) verglichen[3]. Ihre isostrukturellen difluorierten Derivate, Cu,Zn-UoC-5(2F)[4] und Co,Zn-UoC-5(2F), wurden als phasenreine Pulver synthetisiert. Ein bemerkenswerter Aspekt der UoC-5-Struktur ist das Vorhandensein von zwei SBUs: einer Paddlewheel-Einheit $M(COO)_4$ (M = Zn, Cu, Co) und einem oktaedrischen $Zn_4O(COO)_6$-Cluster. Darüber hinaus verfügt die Struktur über Kanäle entlang der [111]-Richtung. Für Cu,Zn-UoC-5(1F) und Cu,Zn-UoC-5(2F) wurden spezifische Oberflächen (S_{BET}) von 1760 m^2/g (Cu,Zn-UoC-5(1F)) und 1400 m^2/g (Cu,Zn-UoC-5(2F)) durch N_2-Sorptionsmessungen ermittelt.

Contents

List of Abbreviations

BET	Brunauer-Emmett–Teller
H_3BPTC	Biphenyl-3,4',5-tricarboxylic acid
H_3BTB	4,4',4"-Benzene-1,3,5-triyl-tribenzoate
H_3BTC	1,3,5-Benzenetricarboxylic acid
CIF	Crystallographic Information File
CCDC	Cambridge Crystallographic Data Centre
d	Doublet
DESY	Deutsches Elektronen Synchrotron
DMA	*N,N*-Dimethylacetamide
DMF	*N,N*-Dimethylformamide
DMSO-d_6	Hexadeuterodimethyl sulfoxide
DSC	Differential Scanning Calorimetry
DTG	Derivative Thermogravimetry
DUT	*Dresden University of Technology*
equiv.	equivalent
FMOF	*Fluorous Metal-Organic Framework*
GooF (S)	Goodness of Fit
ht	*High Temperature*
h	Hour
HKUST	*Hong Kong University of Science and Technology*
IUPAC	*International Union of Pure and Applied Chemistry*
IRMOF	*Isoreticular Metal-Organic Framework*
lit.	Literature
MF	Molecular Formula
MFM	*Manchester Framework Material*
MIL	*Matériaux de l'Institut Lavoisier*
MOF	*Metal-Organic Framework*
MTBE	Methyl-*tert*-butylether
MW	Molecular Weight
NMR	*Nuclear Magnetic Resonance*

n.s.	Not Specified
NU	*Northwestern University*
p.	Page
RDF	*Radial Distribution Function*
PXRD	Powder X-ray Diffraction
R_F	Retention Factor
r.t.	Room Temperature
s	Singlet
SBU	Secondary Building Unit
SCXRD	Single Crystal X-ray Diffraction
t	Triplet
TCM	Tetrachloromethane
Temp.	Temperature
TFA	Trifluoroacetic Acid
TGA	Thermogravimetric Analysis
THF	Tetrahydrofuran (Oxolane (IUPAC))
TMS	Tetramethylsilane
UiO	*Universitetet i Oslo*
UHM	*University of Hamburg Materials*
UoC	*University of Cologne*
ZIF	*Zeolitic Imidazolate Framework*

1 Motivation

Porous materials have always played a significant role in nature, such as porous rocks or as channel systems found in plants and biological tissues. Humans have been utilizing these materials for centuries due to their sorption capacity, with the earliest documented application being the use of activated carbon in ancient Egypt.[5,6] Systematic research into porous adsorbents began in 1773 with the work of *Scheele, Priestley, and Fontana.*[7,8] The first industrial application was charcoal in sugar refinery at the beginning of the 19th century.[9] By the late 19th century, large-scale industrial production of porous materials had commenced. Today, these materials have a wide range of applications and are an integral part of our daily lives. Well-known examples are zeolites used as dehumidifiers or as ion exchangers in detergents.[10,11] However, traditional porous materials, such as zeolites, have limitations in terms of chemical modification. The increasing demand for porous materials with greater structural diversity has led to a growing interest in Metal-Organic Frameworks (MOFs) since the discovery of MOF-5[12] and HKUST-1[13] in 1999. MOFs are like the LEGO® of the scientific world due to their modular nature. Their building blocks are the metallic nodes and the organic linkers that can be flexibly modified. The principle of modular synthesis enables customized materials for specific applications. These applications often address global issues, such as the selective capturing and storing of pollutants to mitigate climate change, as well as storing clean energy gases for renewable energy applications. MOFs also enable controlled drug delivery[14,15] in healthcare, support sustainable agricultural practices, and their catalytic and biosensing capabilities enhance green manufacturing and disease detection. In summary, MOFs have the potential to address various global challenges that the society is currently facing. Therefore, further research on MOFs is crucial.

2 Scientific Objective

The low thermal stability of MOFs compared to zeolites remains a significant drawback for potential industrial applications. In 2007, FMOF-1[16], a fluorous MOF based on a 1,2,4-triazolate linker with CF_3 substituents, was introduced. It demonstrates enhanced thermal, light, and air stability, along with a high H_2 gas uptake. *Banerjee et al.* investigated the effect of linker fluorination in a series of isostructural MOFs and found out that the effect of fluorination varies depending on the system.[17,18] This shows the importance of such systematic studies to understand the effect of fluorination on structural and physical properties.

In this work, the focus was on synthesising isostructural MOFs with linkers that vary in their degree of fluorination. Specifically, it was targeted to synthesis a series of isostructural MOFs based on fluorinated linkers derived from trimesic acid (H_3BTC): trimesate (BTC^{3-}), monofluorinated trimesate (mF–BTC^{3-}), difluorinated trimesate (dF–BTC^{3-}), and perfluorinated trimesate (pF–BTC^{3-}). Additionally, efforts were made to synthesise isostructural MOFs with trimesate linkers that carry amino substituents (mA-BTC^{3-} and dA-BTC^{3-} (A = NH_2), (see Figure 2.1)).

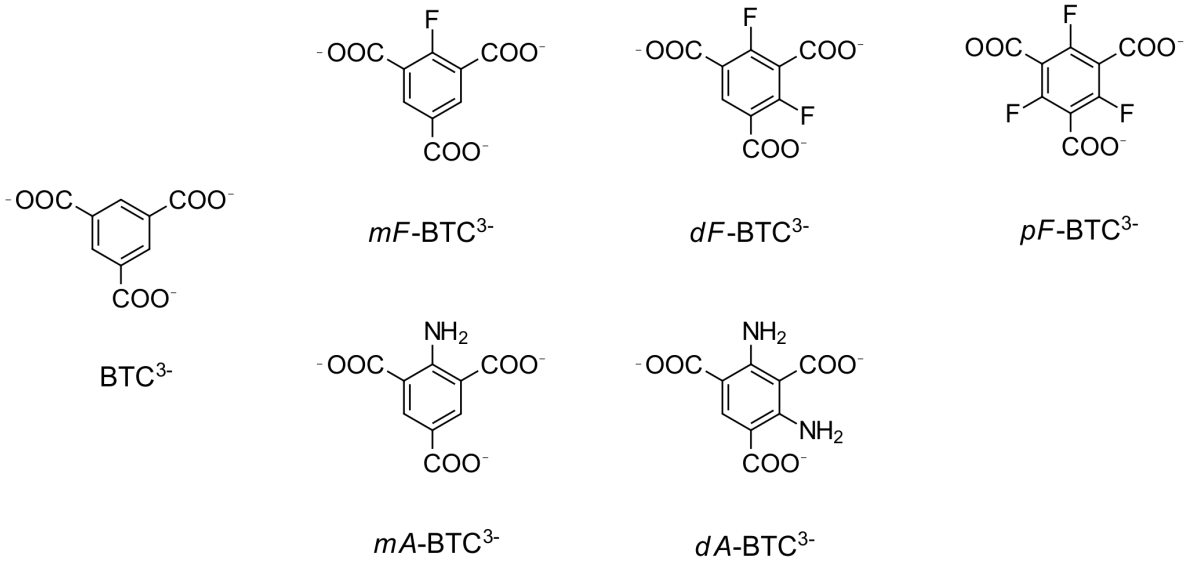

Figure 2.1: Fluorine and amino substituted trimesate linkers used in the course of this work.

Unlike fluorine substituents, which are electron withdrawing (-I-effect), amino substituents have the opposite effect (+M-effect).
Moreover, it was aimed to synthesise isostructural MOFs with larger pores using the isoreticular approach. For this purpose, fluorinated linkers derived from biphenylic tricarboxylic acid (H_3BPTC) and 4,4',4"-benzene-1,3,5-triyltribenzoate (H_3BTB) were used. These linkers are shown in the following Figure 2.2.

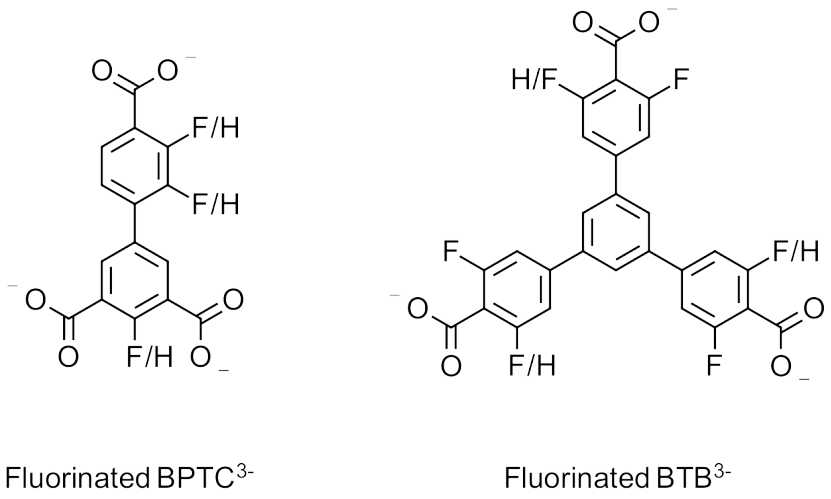

Figure 2.2: Linkers used instead of fluorinated trimesates for the aim to synthesise MOFs with larger pores: fluorinated $BPTC^{3-}$ and fluorinated BTB^{3-}.

Overall a particular focus was on characterising the resulting structures and investigating how the substituents influence them. Additionally, their impact on the thermal and chemical stability of the resulting MOFs was examined. Finally, the MOFs must be activated in order to record N_2 and CO_2 sorption isotherms, which will then be used to investigate the influence of the substituents on the sorption behaviour of the MOFs.

3 Fundamentals

The research interest in MOFs has greatly increased over the last two decades. This growth is underlined by over 100,000 MOF structures, which have been catalogued in the Cambridge Crystallographic Data Centre (CCDC) and by the thousands of publications each year dealing with their synthesis, structural analysis, and diverse applications.
According to the International Union of Pure and Applied Chemistry (IUPAC), MOFs are defined as coordination networks that feature potential pores.[19,20] These pores are initially occupied by solvent molecules and reactants used during the synthesis. If the frameworks remain stable after removing these molecules, the resulting accessible pores can be utilised for a wide range of applications.

3.1 Structure and Building Units of MOFs

MOFs, a subgroup of coordination polymers, are formed through the coordination of metal cations or oxoclusters with organic linkers.[19,20]
Each MOF structure has an underlying topology[21] that describes its complex structure in terms of a simplified net. Determining this underlying topology involves deconstructing the MOF structure into its constituent building units.
The building units of MOFs are often referred to as secondary building units (SBUs), which is explained in more detail later in this chapter, and organic linkers. Common organic linkers, which generally have a rigid backbone and must contain at least two functional groups, include azolates, sulfonates, phosphonates, and carboxylates. Among these, aromatic polycarboxylates are very likely used linkers in coordination polymers and MOFs.
The other building unit of MOFs is the 'Secondary Building Unit' (SBU). This term was originally used to describe the structural chemistry of zeolites and has since been adapted to MOF chemistry to refer to the inorganic building units within MOF structures.

SBUs are (polynuclear) clusters of metal ions, where the polydentate binding groups of the linkers are a crucial component of these units as they fix the positions of the metal cations.
Figure 3.1 shows three examples of SBUs found in MOF structures namely those of GaMOF-1,[22] HKUST-1[13] and MOF-5[12].

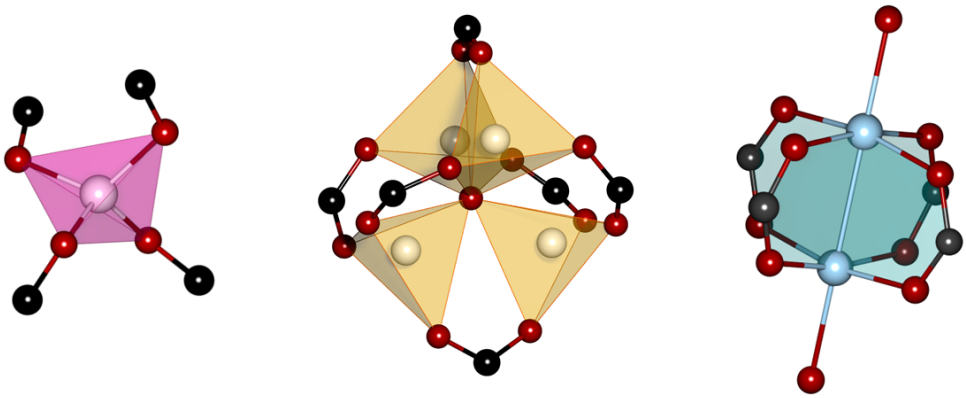

Figure 3.1: The SBUs of GaMOF-1,[22] HKUST-1,[13] and MOF-5[12] are shown from left to right: tetrahedral $Ga(COO)_4$, $Cu_2(COO)_4$ paddlewheel, and octahedral $Zn_4O(COO)_6$. Colour code: Ga (white), Zn (white), Cu (blue), O (dark red), C (black).

The SBU of HKUST-1 is a Cu_2-paddlewheel. Such dinuclear paddlewheels $M_2(COO)_4$ ($M = Cu^{2+}$, Zn^{2+}, Co^{2+}) are the most common 4-connected (4-c) SBU motifs in MOF chemistry.
In the HKUST-1 structure, each Cu^{2+} cation is coordinated in a square-pyramidal geometry by four oxygen atoms from bridging carboxylates and one terminal neutral ligand. The terminal ligand is most frequently a water molecule, which can be removed by heating and replaced by other molecules.[13]
Another common SBU in MOF chemistry is the octahedral $Zn_4O(COO)_6$ cluster. It can be found in the structure of the well-known MOF-5[12], whose stepwise construction is shown in the following Figure 3.2.

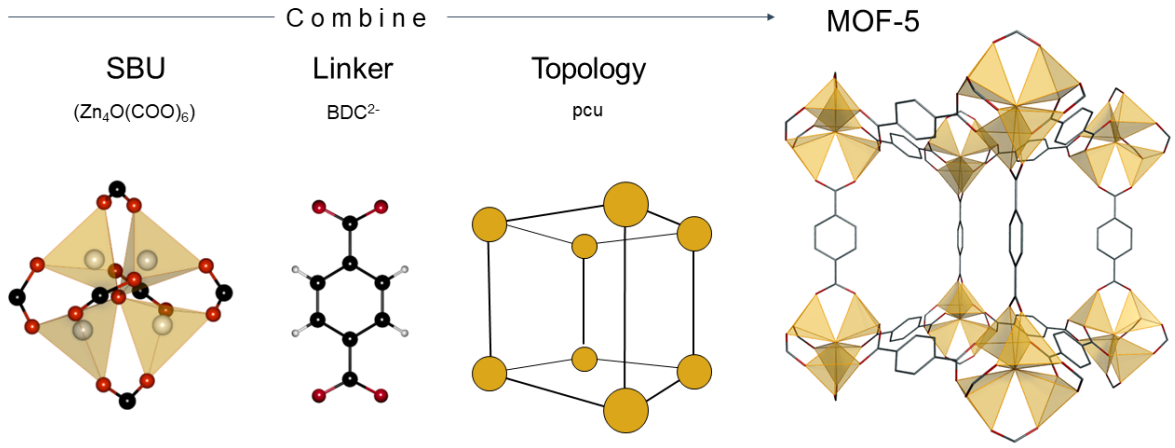

Figure 3.2: The stepwise construction of a MOF is exemplified by MOF-5.[12] Crystallographic data were taken from *Yaghi et al.*[12] Colour code: Zn (white), O (dark red), C (black), H (light grey).

3.2 Functionalisation of MOFs

The demand for MOFs customised for specific applications is steadily increasing. This demand is met through reticular chemistry, derived from the Latin 'reticulum' signifying 'having the form of a net' or 'netlike'.

Reticular chemistry relies on an understanding of topological nets and the ability to modify node and linker structures to achieve a desired topology.[23–29]

Several synthetic strategies have been employed in this context, including the molecular building block (MBB) approach pioneered by *Yaghi et al.*, the two-step crystal engineering method reported by *Zaworotko et al.*, and the supermolecular building block (SBB) approach established by *Eddaoudi et al.*[30–37]

Examples of reticular chemistry applied to MOF synthesis include MOF-5,[12,38] MOF-101,[39] MOF-177,[36] and MOF-1[40].

Significant milestones have been achieved with NU-110[41] and DUT-60[42], which established new porosity records, and with IRMOF-74-XI,[43] which realised ultra-large channels, measuring $85 \cdot 98\,\text{Å}$.

The following Figure 3.3 provides a schematic illustration of isoreticular MOFs (IRMOFs) differing in their linker length and therefore in their pore sizes. The illustration is based on the IRMOF series of MOF-5, described by *Yaghi et al.*[12,38]

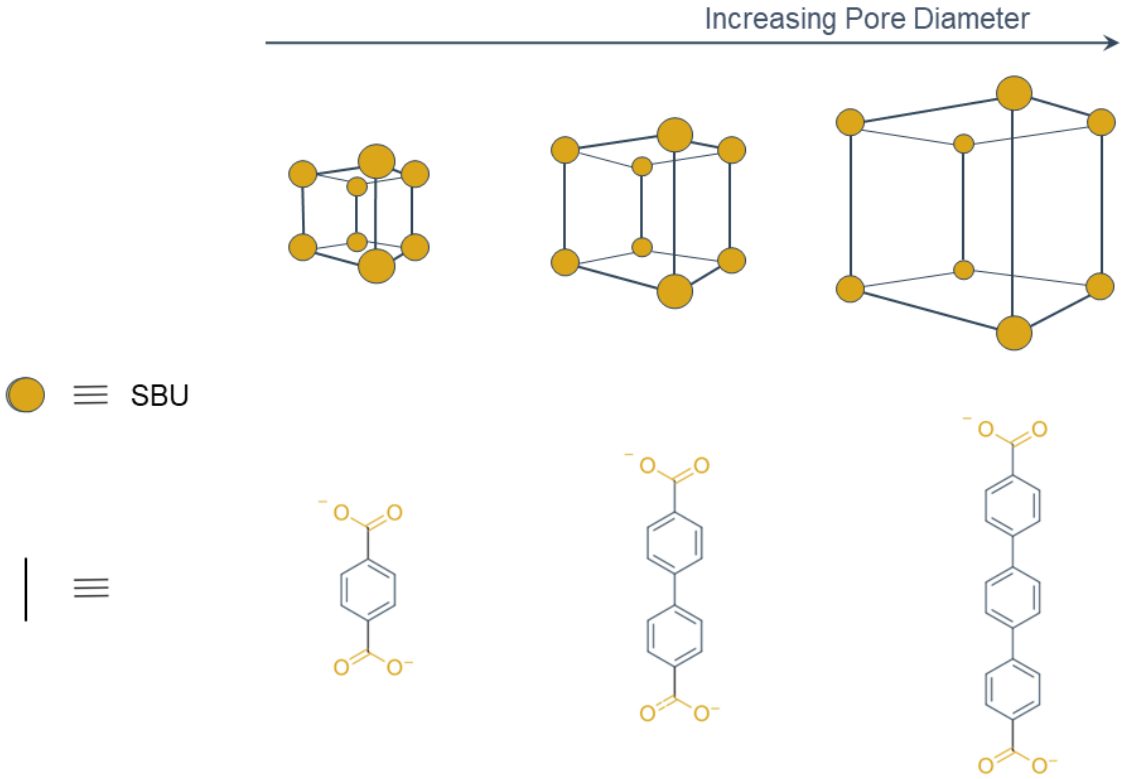

Figure 3.3: AA schematic illustration of three IRMOFs based on the IRMOF series of MOF-5.[12,38] All structures in this series have the same cubic network as MOF-5, featuring a 6-connected **pcu** net, differing only in the length of the linker.

In addition to altering the linker size or pore dimensions, reticular synthesis allows for modifications to the side-chain functionalities of the linkers, thereby affecting the pore surface and various physical properties, as well as the metal cations.[44]
Regarding the latter, the choice of the metal cation can also influence the size and shape of the pores, the stability, and the adsorption properties of the MOF. Furthermore, it can also affect the synthesis and growth of the MOF.

The properties of the metal cation, such as polarity, size, and charge, influence its interaction with the organic linker and the formation of coordination bonds.
Moreover, the selection of metal cations significantly impacts the adsorption properties of MOFs by modifying their affinity for specific molecules or ions. *Avci et al.* demonstrated substantial improvements in adsorption characteristics by substituting zinc cations with other metal cations.[45]
As previously mentioned, the side-chain functionalities of linkers play a crucial role in modulating the pore surface and other physical properties of MOFs. Substituents with either electron-donating or electron-withdrawing effects (through -/+ I- or M-effect) can significantly impact the electron density and polarity of aromatic carboxylate-based linkers. These changes, in turn, can alter the overall structure and adsorption characteristics of the MOF.[44] For instance, substituents like methoxy or amino groups can increase the electron density within the phenyl ring, while fluorine can decrease it (see Figure 3.4).

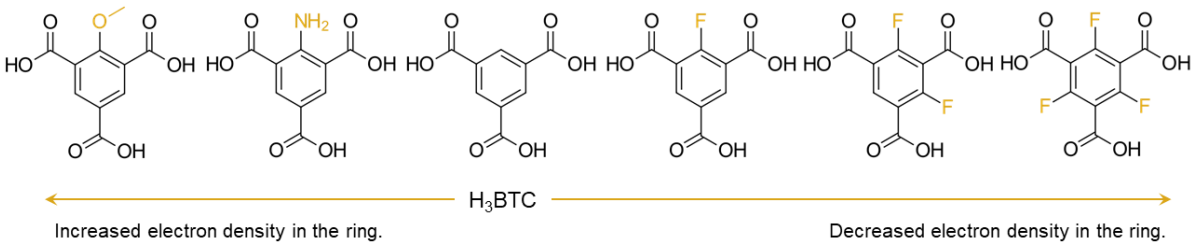

Figure 3.4: The functionalisation of H_3BTC with either a methoxy or an amino group, which enhances the electron density in the ring (+M-effect), as well as the incorporation of fluorine atom(s), which reduces the electron density in the ring (-I-effect).

3.3 Fluorinated MOFs (FMOFs)

Fluorinated MOFs (FMOFs) represent a special example of functionalisation in metal-organic frameworks, where hydrogen atoms in the linkers are (partly) replaced by fluorine substituents.[46,47]

The research interest in FMOFs can be traced back to FMOF-1, which was introduced by *Yang et al.* in 2007.[16] FMOF-1 features a 1,2,4-triazolate linker with CF_3 substituents, resulting in pores lined with fluorine atoms. This MOF exhibits remarkable superhydrophobicity, demonstrated by a contact angle of 158°, and remains stable even in boiling water. The strong C−F bonds contribute to its enhanced resistance to thermal, light, and air degradation.[48] Notably, FMOF-1 also shows impressive hydrogen storage capabilities, with a volumetric H_2 storage capacity ($41\,\mathrm{kg\,m^{-3}}$ at 77 K and 64 bar), one of the highest reported at that time.

The suitability of FMOFs for hydrogen storage has been further supported by other experimental work[49] and theoretical studies.[50] *Zhang et al.* described the substitution of protons by fluorine atoms or CF_3 groups in MOF-5, which showed an increased hydrogen uptake capacity compared to unfluorinated MOF-5[50].

Beyond hydrogen storage, FMOFs like FMOF-1 have shown high and selective CO_2 adsorption, even in humid conditions, making them promising candidates for carbon capture from industrial wet gas streams.[16,46,47,51] This property has been observed in other FMOFs as well. For instance, *Pachfule et al.* and *Peikert et al.* reported a 30-47 % increase in CO_2 uptake in fluorinated MOFs (Co-FINA-2 and UHM-31) compared to their non-fluorinated analogues (Co-INA-2 and HKUST-1).[17,52]

However, it should be noted that these effects are not universal among FMOFs.[53] Other experimental work in this area has produced varying results. For example, the perfluorinated analogue of UiO-66 exhibits a diminished CO_2 uptake compared to the unfluorinated UiO-66.[54]

Pachfule et al. reported the effect of linker fluorination in a series of isostructural MOFs.[17,18] They concluded that the effect of fluorination varies depending on the system.[17,18]

A number of factors may influence the observed effects, including pore size, shape, accessibility and the positioning of fluorine atoms within the pores. In order to gain a deeper understanding of the influence of fluorine atoms, it is essential to synthesise

isostructural systems of fluorinated and unfluorinated MOFs.
However, the synthesis of isostructural MOFs with fluorine-functionalised linkers is challenging, particularly for aromatic carboxylate linkers, due to a number of factors.
Firstly, the synthesis of fluorinated linkers is challenging due to the limited availability of fluorinated starting materials and the potential hazards associated with direct fluorination methods, such as the generation of hydrofluoric acid (HF).
Secondly, fluorinated linkers based on aromatic carboxylates with an otherwise planar geometry, such as trimesic acid, exhibit significantly increased interplanar angles between the carboxylate groups and the phenyl rings (see the following Figure 3.5).
This phenomenon is particularly pronounced for carboxylate functions in the ortho position relative to fluoro substituents. Such a geometrical alteration influences the structural chemistry of these compounds, thereby complicating the synthesis of isostructural MOFs.[55,56] Moreover, the electron-withdrawing effect of fluorine can reduce the thermal stability of fluorinated linkers and their corresponding frameworks, primarily due to an increased tendency for decarboxylation.[55,56]

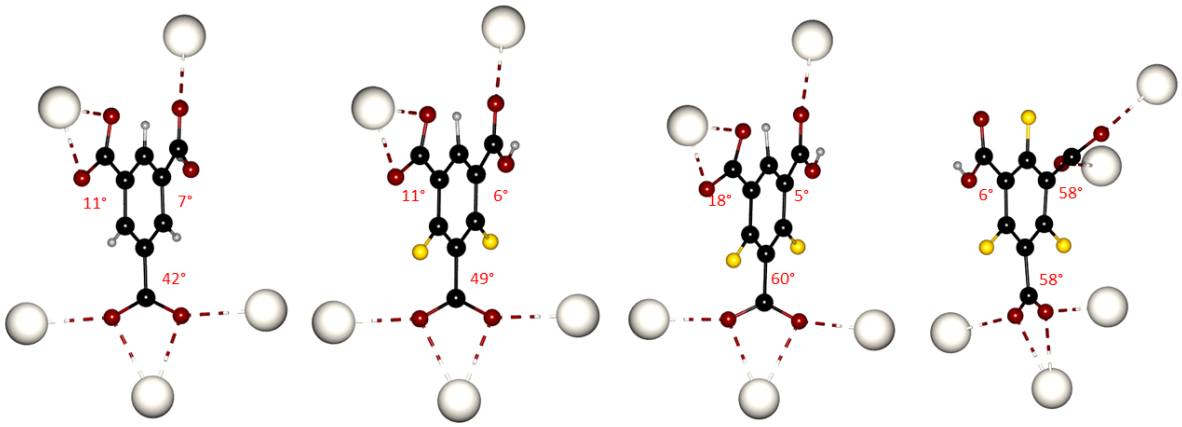

Figure 3.5: Compilation of the interplanar torsion angles of trimesate (BTC^{3-}) with different degrees of fluorination in the crystal strutures of ${}^{3}_{\infty}[Sr(H\text{-}BTC)_{5/5}(H_2O)_{2/1}]\cdot 0.5\,H_2O$, ${}^{3}_{\infty}[Sr(H\mathit{m}F\text{-}BTC)_{5/5}(H_2O)_{2/1}]\cdot 0.5\,H_2O$, ${}^{3}_{\infty}[Sr(H\mathit{d}F\text{-}BTC)_{5/5}(H_2O)_{2/1}]\cdot 0.5\,H_2O$ and ${}^{3}_{\infty}[Sr(H\mathit{p}F\text{-}BTC)_{5/5}(H_2O)_{2/1}]\cdot 1.5\,H_2O$ (from left to right), as published by *Smets et al.*[55] F is is disordered over two positions in ${}^{3}_{\infty}[Sr(H\mathit{m}F\text{-}BTC)_{5/5}(H_2O)_{2/1}]\cdot 0.5\,H_2O$. Colour code: Sr (white), O (dark red), C (black), F (yellow), H (light grey).

3.4 Anionic MOFs

Anionic MOFs represent only a small percentage of the total number of MOF structures documented in the CSD database.[57] They consist of a negatively charged framework with uncoordinated counter ions present within the framework to balance the charge.[58] Targeting the synthesis of anionic MOFs is challenging and is often described as occurring accidentally.[58] Four different design strategies have been discussed. The first strategy involves post-synthetic modification (PSM). The second strategy is the use of linkers with uncoordinated negatively charged functional groups, such as carboxylate or sulfonate. The third strategy involves using solvents that generate cations.[59] For example, N,N-dimethylacetamide (DMA), N,N-dimethylformamide (DMF), or N,N-diethylformamide (DEF) can undergo hydrolysis and subsequent decarbonylation in the presence of water to form $(CH_3)_2NH_2^+$ or $(C_2H_5)_2NH_2^+$ cations under solvothermal conditions.[60] This hydrolysis and decarbonylation can be facilitated by adding a strong acid, such as HNO_3 or HCl, to the solvent. These $(CH_3)_2NH_2^+$ or $(C_2H_5)_2NH_2^+$ cations can then act as counter cations for anionic frameworks. Many anionic MOFs contain a $(CH_3)_2NH_2^+$ cation or another dialkyl congener. Nevertheless, most of the more than 100,000 published MOFs have a neutral framework, even though they were synthesized under solvothermal conditions using DMA, DMF, or DEF.

The fourth strategy, widely regarded as the prime method for synthesising anionic MOFs, involves employing negatively charged SBUs. *Karmakar et al.* provided a detailed analysis of the SBUs and network topologies of the resulting anionic MOFs.[58] This approach has led to the development of various mono-, di-, tri-, and polynuclear negatively charged SBUs, which in turn result in the formation of anionic MOFs.[61–63]

Interestingly, it has been shown that certain metal nodes, such as In^{3+}, Ga^{3+}, or UO_2^{2+}, are more likely to form anionic SBUs. This behaviour has been exploited by *Eddaoudi et al.* in the design of anionic indium-based ZMOFs (zeolite-like metal-organic frameworks), which have demonstrated high tunability through cation exchange.[64,65]

It is noteworthy that for only a small number of anionic MOFs, the positions of the charge-compensating cations have been confirmed through single crystal X-ray diffraction. One reason for this is the low scattering power of carbon and nitrogen adjacent to a heavy metal cation, which hampers stable refinement. Additionally, the disorder of the cations, similar to the solvent molecules present within the pores, contributes to this

problem. Unfortunately, this inherent issue is rarely resolved by measurements conducted at low temperatures or using intense and focused synchrotron radiation.

For most anionic MOFs, the cation positions were not found or refined. Instead, the *SQUEEZE*[66] routine was used to account for their electrons within the pores of the respective MOF.

Several review articles discuss potential applications of anionic MOFs.[58,67–71]

One notable example is UoC-3, which demonstrates excellent Cs^+ exchange properties[72] and could be applied in the decontamination of seawater, an issue highlighted by the nuclear disaster at the Fukushima Daiichi nuclear power plant.

Another example of a cation exchanger is GaMOF-1, introduced by *Banerjee et al.*.[22] In GaMOF-1, each gallium cation (Ga^{3+}) is tetrahedrally surrounded by four BTC^{3-} linkers. These isolated Ga^{3+} tetrahedra are then connected by the BTC^{3-} linkers, forming an overall three-dimensional anionic porous network, as illustrated in Figure 3.6.

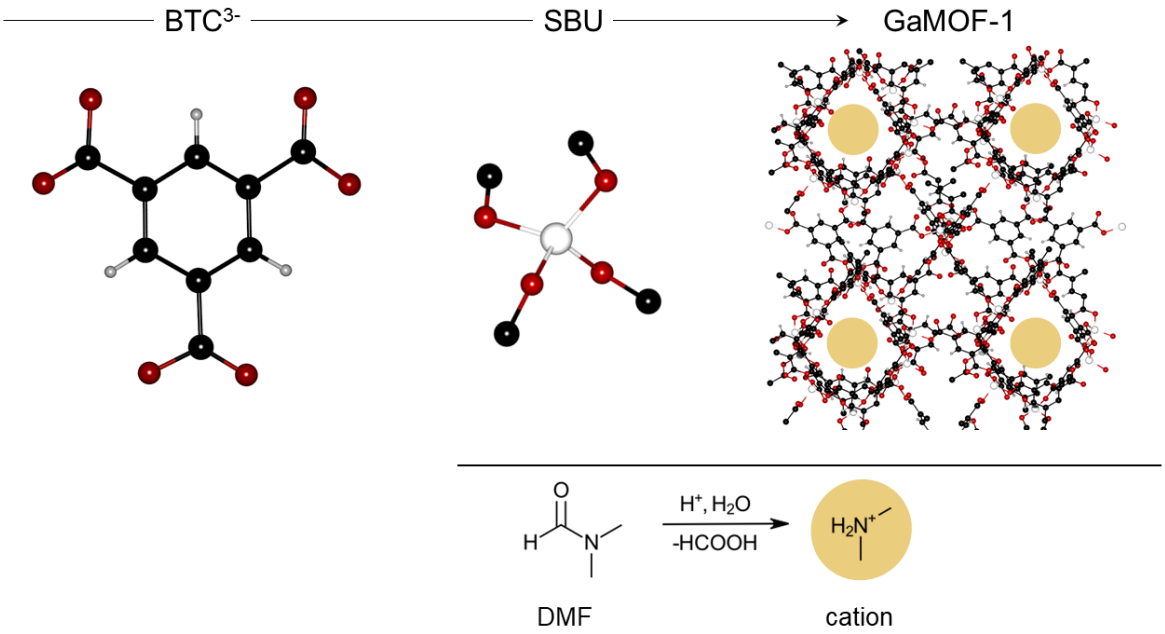

Figure 3.6: BTC^{3-} linker and Ga^{3+} tetrahedron forming the GaMOF-1[22] framework, from which a cross section is shown. DMF undergoes hydrolysis, forming $(CH_3)_2NH_2^+$ cations that are located in the pores of GaMOF-1.[22] Crystallographic data were sourced from Banerjee et al.[22] Color code: Ga (white), O (dark red), C (black), H (light grey).

Dimethylammonium cations were postulated as the counter ions. Attempts to synthesise GaMOF-1[22] using the larger tetrapropylammonium cation resulted in the formation of a different anionic framework structure, referred to as CAUMOF-11[73].
This phenomenon is known as the template effect, where the presence of specific molecules, which are not part of the framework, influences the topology of the resulting compound.[74] The template molecules typically remain within the pores of the prepared MOF but can sometimes be removed if the framework is sufficiently stable.

3.5 Porosity of MOFs

A classification system for porous materials based on their pore sizes has been established by IUPAC. This system distinguishes between the following categories: ultramicroporous, denoting materials with pore sizes smaller than 0.7 nm; microporous, denoting materials with pore sizes between 0.7 and 2 nm; mesoporous, denoting materials with pore sizes between 2 and 50 nm; and macroporous, denoting materials with pores larger than 50 nm in diameter.
MOFs are characterised by their remarkable sorption properties, which are attributed to their porosity and specific surface area. Their pore size ranges from ultramicroporous to mesoporous, and they demonstrate high Brunauer–Emmett–Teller (BET) surface areas, reaching up to $S_{BET} = 10.000\,m^2\,g^{-1}$, significantly surpassing those of zeolites and activated carbons.[41,75,76]
These properties can be quantified through sorption measurements, providing a comprehensive analysis of adsorption and desorption phenomena. A widely used method is volumetric nitrogen N_2 sorption analysis. In this method, the quantity of gas adsorbed by the MOF is measured as a function of the relative pressure p/p_0, where p represents the equilibrium pressure and p_0 denotes the saturation vapour pressure of the gas. The resulting adsorption isotherm is used to determine the pore size distribution and surface area of the material.

To ensure accurate measurements, a careful sample preparation is essential. This involves heating the MOF samples under vacuum until they reach a stable mass, ensuring that the pores are fully accessible and free from any adsorbates that could affect the results. Tens of thousands of gas adsorption isotherms measured on a wide range of solids are documented in the literature on porous materials. IUPAC has delineated six types of isotherms: types I to VI, as illustrated in the following Figure 3.7. This classification was expanded in 2015 to incorporate two additional subtypes, with type I and type IV isotherms each subdivided into type I(a) and type I(b), as well as type IV(a) and type IV(b), based on different substances and their corresponding porosities.
Type I isotherms exhibit a steep initial slope, indicative of high uptake at low pressures, followed by a plateau as saturation is reached. This behaviour is characteristic of microporous materials, where the total adsorption is constrained by the pore volume of the solid being studied. MOFs with pore sizes typically smaller than 20 Å often display Type I isotherms.

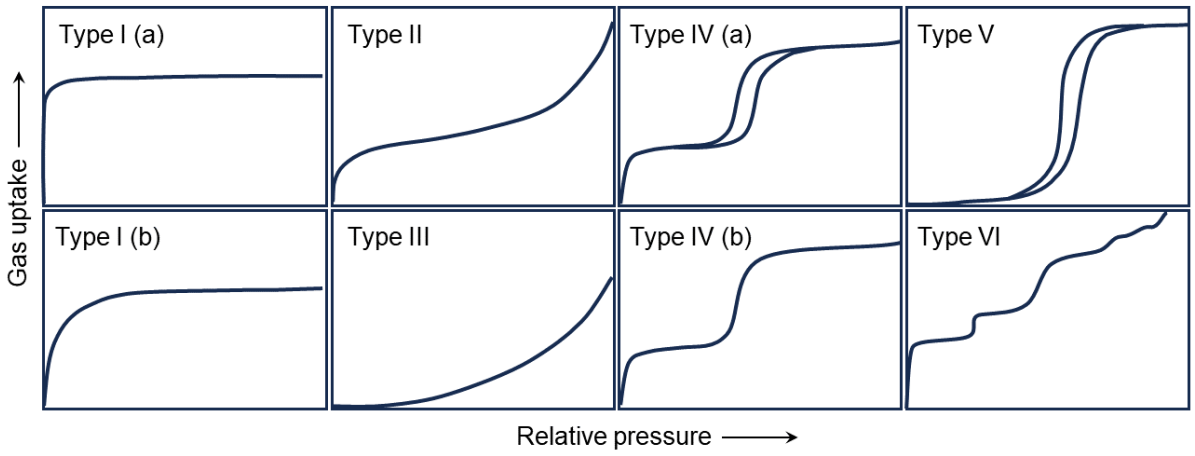

Figure 3.7: A schematic representation of IUPAC-classified sorption isotherms.[77]

Type II isotherms are typical of non-porous solids or macroporous materials, where multilayer sorption is not restricted by pore size. Monolayer adsorption occurs at low pressures, followed by continuous uptake through successive layers.
Type III isotherms signify materials where adsorbate-adsorbate interactions prevail over adsorbent-adsorbate interactions.

Type IV isotherms are also common in mesoporous materials, featuring monolayer formation. Notably, for Type IV(a) isotherms, a distinctive hysteresis loop appears at higher pressures due to capillary condensation of the adsorbate. As with Type I, the adsorption capacity is limited by the pore volume.
Type V isotherms resemble Type III isotherms at low pressures, indicating weak adsorbent-adsorbate interactions relative to adsorbate-adsorbate interactions. Additionally, an extra hysteresis loop may indicate the presence of mesopores.
Type VI isotherms are characteristic of non-porous adsorbents, depicting a stepwise multilayer adsorption process.

The mathematical computation of specific surface area is proposed by *S. Brunauer, P. H. Emmett*, and *E. Teller* (BET method) or the Langmuir model.
Gas adsorption within MOFs is typically governed by weak interactions (physisorption) and can, to a certain extent, be elucidated by both models. The primary disparity between the two models lies in the fact that, unlike the Langmuir model, the BET model accommodates multilayer adsorption, which is particularly significant when addressing larger pores ($> 2\,\mathrm{nm}$).
The determination of specific surface areas using the multilayer adsorption method devised by the BET method is prescribed for type II and type IV isotherms. This method is based on the assumption of the formation of a closed adsorbate monolayer on both the outer and inner pore surfaces before the commencement of multilayer adsorption. Typically, the BET method is applied within a relative pressure range of approximately 0.05 to 0.3 for these isotherms.
However, in the context of microporous compounds characterised by type I isotherms, distinguishing between micropore filling, monolayer adsorption, and multilayer adsorption poses considerable challenges. Type I isotherms are characteristic of microporous materials and show a rapid increase in adsorbed gas at very low relative pressures, which makes it complex to separate these adsorption stages. Additionally, the relative pressure range that meets the criteria for the BET equation shifts to substantially lower pressures for type I isotherms. Consequently, the determination of specific surface area for type I isotherms using the BET method should be regarded as an approximation.

To improve accuracy in such cases, it is important to explicitly specify the chosen relative pressure range for the analysis. *Rouquerol* plots can be employed to determine the appropriate pressure range for BET analysis and to better assess the limitations of the method for different isotherm types.

3.6 Potential and Actual Applications of MOFs

In recent years, a multitude of companies have initiated the commercialisation of MOFs for a diverse array of applications. These enterprises encompass small spin-offs from academic laboratories, start-ups specifically dedicated to MOFs, and large multinational corporations incorporating MOF technologies into their existing research and development divisions. The following Table 3.1 presents a selection of examples and three examples will be presented in more detail below.

Table 3.1: Selected companies in the MOF industry.

Company	Description of the MOF Activity
BASF	Large scale production
Bosch	Sensors
Merck KGaA	Crystallography
MOF Technologies	MOF R&D services and synthesis
Molecule	Atmospheric water harvesting
NuMat Technologies	Integrated MOF solutions provider
Rimo Therapeutics	Therapeutics
Sikemia	MOF ligand supplier
SyncMOF	MOFs and new gas utilization systems
Water Harvesting Inc.	Atmospheric water harvesting

Hydrogen (H_2) is emerging as an environmentally friendly energy carrier, while methane (CH_4) from natural gas is an attractive fuel due to its abundance and relatively clean combustion process.

Both H_2 and CH_4 are promising and viable alternatives to conventional fossil fuels. However, one of the most significant challenges currently facing scientists in the 21st century is the development of energy storage solutions. In this context, BASF, in collaboration with *Yaghi*, is developing a storage solution for natural gas vehicles using MOFs. Extensive research has been conducted to identify suitable MOF materials to facilitate the storage of these gases, particularly for automotive applications, while meeting stringent criteria. The results of trials conducted by BASF have demonstrated that these materials can effectively double the tank capacity while maintaining stability throughout the vehicle's operational lifespan.[78]

Another promising MOF technology is the adsorptive dehumidification from BASF.[79] An air-conditioner is tasked with cooling external air to a comfortable level, whereby the humidity then begins to condense. The process of dew-pointing air is energy-intensive. An energy-efficient alternative could involve a system wherein moisture is selectively adsorbed by a MOF,[80] resulting in reduced power consumption of the device. In optimal settings, the implementation of a MOF based air-drying system could result in an approximate 50–60 % reduction in energy consumption.

The third impressive example is being developed by a company called *Water Harvesting Inc.* They are currently developing market-ready devices for the commercialisation of atmospheric water harvesting. In a field trial conducted in the Mojave Desert, the Al^{3+} based MOF-303 demonstrated the ability to adsorb water at night, and release it during the day when exposed to sunlight. This process yielded approximately 0.7 litres of water per kilogram of MOF per day.

The preceding examples show the potential of MOFs to serve as foundational elements of green technologies that could contribute to a sustainable world, a matter of significant importance in the light of the current climate crisis. As these materials become more accessible, it is probable that additional applications will emerge in the future.

4 Results and Discussion

4.1 Synthesis of the Linkers

As stated in the objective, the aim of this work was to synthesise and characterise isostructural MOFs based on fluorinated BTC^{3-} and $BPTC^{3-}$ linkers (see chapter 2, p. 2 and following).
H_3BTC was used as it is commercially available, while all other trimesate linkers had to be synthesised in advance. $K(H_2BTC)\cdot H_2O$[81], $K(H_2mF\text{–}BTC)$[82], and $K(H_2dF\text{–}BTC)$[83] were successfully reproduced (see chapter 4.1.1, p. 18), whereas $K(H_2pF\text{–}BTC)$ could not be reproduced during this work. Further details of the attempted synthesis can be found in Chapter 4.1.2 (on p. 20).
Additionally, H_3mA-BTC was successfully synthesised, unlike its diamino congener H_3dA-BTC (see Chapter 4.1.3 on p. 24).
In an attempt to synthesise isostructural MOFs with elongated linkers, H_3mF/dF–BTB could be used as synthesised in the working group. Additionally, fluorinated BPTC was sucessfully synthesised. (see Chapter 4.1.4 on p. 25).

4.1.1 Synthesis of $K(H_2BTC)\cdot H_2O$, $K(H_2\boldsymbol{mF}\text{–}BTC)$ and $K(H_2\boldsymbol{dF}\text{–}BTC)$

$K(H_2BTC)\cdot H_2O$ is described in literature by *Li et al.*,[81] but in the course of this work, it was synthesised in a different way. In fact, it was synthesised by adding potassium hydroxide to a suspension of H_3BTC and water (see Figure 4.1), $K(H_2BTC)\cdot H_2O$ was then recrystallised in an EtOH/water mixture and obtained as a colourless solid.

Powder X-ray diffraction (PXRD) pattern revealed the phase pure formation of $K(H_2BTC)\cdot H_2O$ (see appendix, p. 139) NMR spectroscopy confirmed its purity (see appendix, p. 131).

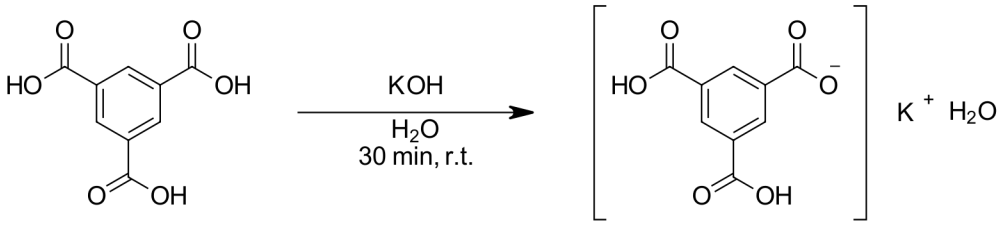

Figure 4.1: The reaction equation of the synthesis of $K(H_2BTC)\cdot H_2O$.

$K(H_2mF\text{–}BTC)$ and $K(H_2dF\text{–}BTC)$ were reproduced on the basis of the synthesis procedure described by *Krautwurst et al.*[56,82] The corresponding mesitylenes were oxidised by potassium permanganate ($KMnO_4$) in water (see Figure 4.2).

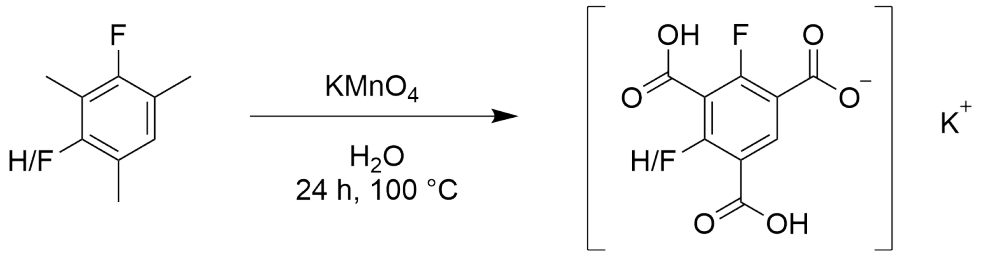

Figure 4.2: The reaction equation of the synthesis of $K(H_2mF\text{–}BTC)$ and $K(H_2dF\text{–}BTC)$.[83,84]

The yield of both reactions was slightly increased by changing some of the work-up steps. A detailed description of the synthesis procedure can be found in the experimental section from p. 96.

Both linkers were obtained as colourless powders. Their purity was confirmed by PXRD and by NMR spectroscopy (see appendix from p. 132 and following). $K(H_2mF\text{-}BTC)$ was obtained in a yield of 70 % (Lit. 58 %)[82] and $K(H_2dF\text{-}BTC)$ in a yield of 66 % (Lit. 45 %).[83]

4.1.2 Attempted Synthesis of K(H_2pF–BTC)

The synthesis of the perfluorinated trimesate linker (pF-BTC^{3-}) would complete the series of fluorinated BTC^{3-} linkers used in this work (see Chapter 2, p. 2).
For this purpose, a synthesis must be found that makes this linker accessible either as a free acid H_3pF-BTC or as a respective salt like K(H_2pF–BTC).
Unlike K(H_2mF–BTC) and K(H_2dF–BTC), K(H_2pF–BTC) cannot be synthesised by the oxidation of 1,3,5-trifluoro-2,4,6-trimethylbenzene with $KMnO_4$.
The literature describes the oxidation of 2,4,6-trifluoro-3,5-dimethylbenzoic acid giving K(H_2pF–BTC) in a low yield as shown in the following Figure 4.3.[83,84]
This Figure 4.3 also shows that 2,4,6-trifluoro-3,5-dimethylbenzoic acid can be prepared from
3,5-dimethyl-2,4,6-trifluorobenzoyl chloride or 1,3,5-trifluoro-2,4-dimethylbenzene.[55]

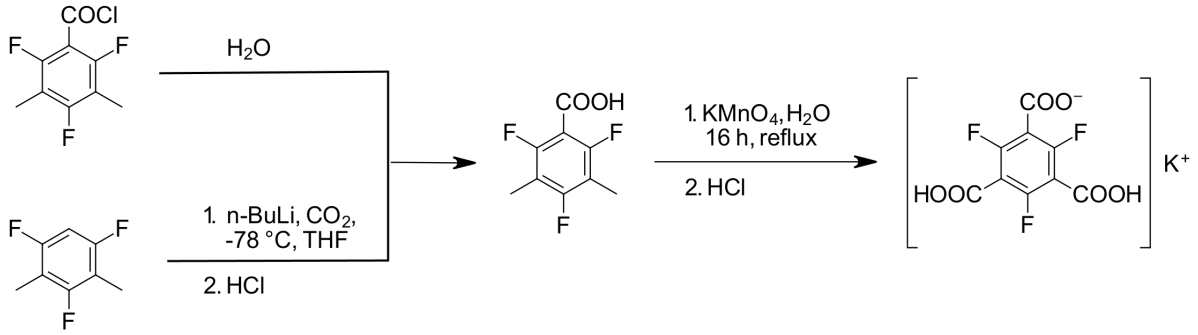

Figure 4.3: Synthesis of K(H_2pF–BTC) described in the literature.[55,83,84]

A challenge associated with fluorinated aromatic carboxylate linkers is the limited availability of commercially accessible fluorinated reactants. Indeed, all reactants reported in the literature are expensive and challenging to procure. The cost of 2,4,6-trifluoro-3,5-dimethylbenzoic acid, 3,5-dimethyl-2,4,6-trifluorobenzoyl chloride and 1,3,5-trifluoro-2,4-dimethylbenzene has fluctuated significantly in recent years, reaching several hundred euros per gram. However, these reactants were commercially entirely unavailable during the period of this thesis. As a result, this work sought to identify an alternative synthetic route.

Lamann has already made several attempts to develop other synthetic routes for K(H_2pF–BTC) without success.[84] The results presented in this chapter build on his work. The retrosyntethic analysis is shown in Figure 4.4.

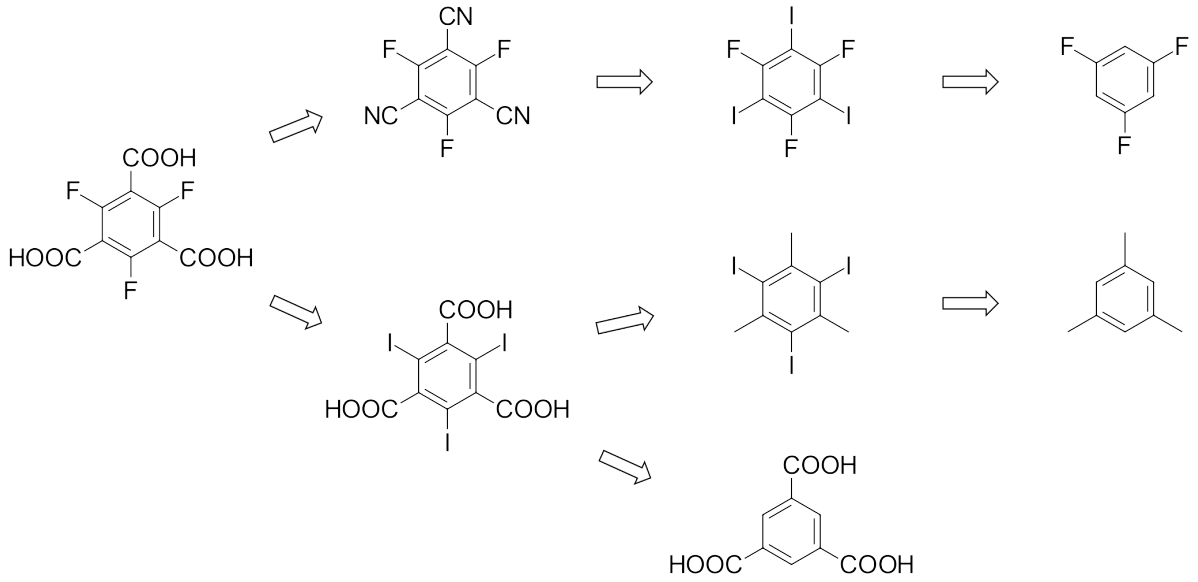

Figure 4.4: Retrosynthetic analysis.

In the first approach, K(H_2pF–BTC) was intended to be obtained in a three-step synthesis, the last step being the hydrolysis of 1,3,5-tricyano-2,4,6-trifluorobenzene.
For this purpose, 1,3,5-trifluoro-2,4,6-triiodobenzene was successfully synthesised according to a synthesis procedure known from the literature (see the following Figure 4.5).[85,86] The starting material is 1,3,5-trifluorobenzene, which is economically an ideal reactant. Starting from 1,3,5-trifluoro-2,4,6-triiodobenzene, 1,3,5-tricyano-2,4,6-trifluorobenzene was tried to be synthesised in three ways (see Figure 4.5 on p. 22). The first approach used $Pd(PPh_3)_4$ and CuI as catalysts and KCN as the CN^- source. GC-MS analysis of the product showed the degradation products of the starting materials. Therefore, the reaction does not lead to any conversion to the desired product.
In another approach, CuI was used as catalyst and $Na_2[Fe(CN)_5NO]$ as cyanation reagent and the reaction was carried out in polyethylene glycol (PEG-200). The product obtained was a black, viscous oil. Mass analysis by GC-MS identified it, as in the previous approach, as a mixture of degradation products of the starting materials.

In the third approach, 1,3,5-trifluoro-2,4,6-triiodobenzene, CuI and $K_4[Fe(CN)_6]$ were reacted together in PEG-6000, which was first melted. The reaction mixture was sonicated and heated to 70 °C. However, the product was not separable from the polymer and the mixture was not soluble, thus no analysis was possible.
In summary, 1,3,5-tricyano-2,4,6-trifluorobenzene and $pF\mathrm{BTC}^{3-}$ could not be synthesised by any of the approaches described above.

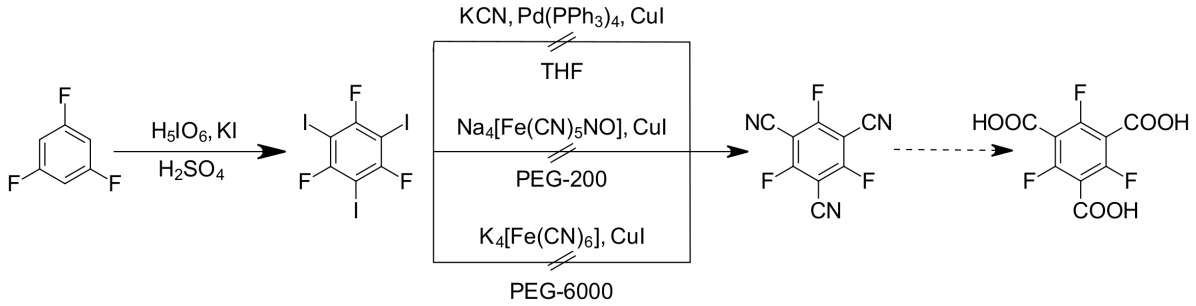

Figure 4.5: Three approaches to synthesise 1,3,5-tricyano-2,4,6-trifluorobenzene.

A different approach was therefore attempted, in which 2,4,6-triiodobenzene-1,3,5-tricarboxylic acid should undergo a Finkelstein reaction. In this reaction iodine in iodinated trimesic acid should be substituted by fluorine yielding in the perfluorinated trimesic acid (see Figure 4.6).

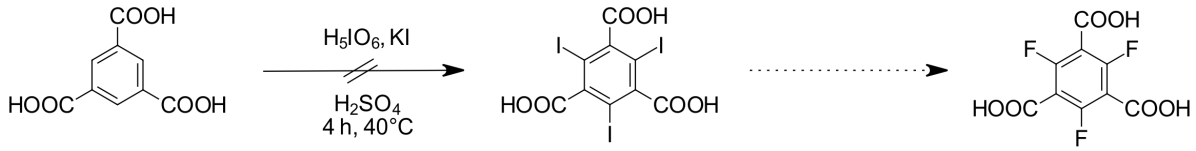

Figure 4.6: The attemped synthesis of 2,4,6-triiodobenzene-1,3,5-tricarboxylic acid as the first step to synthesise the perfluorinated trimesate linker.

For this, first, an attempt was made to prepare iodinated trimesic acid by the iodination of trimesic acid, which was carried out under the same reaction conditions as the iodination of mesitylene described above. Due to the insolubility of the product, it was not possible to characterise or analyse it by NMR spectroscopy or GC-MS. The product and this synthetic route were therefore discarded and the Finkelstein reaction was not carried out.

A further approach starting from mesitylene was partly published by *Xing et al.*[87] (see Figure 4.7). In the first step, mesitylene was reacted with H_5IO_6, I_2 and a catalytic amount of H_2SO_4 to give 1,3,5-triiodo-2,4,6-trimethylbenzene in a yield of 54 %. GC-MS analysis confirmed the presence of the desired product. The purity of the product was confirmed by NMR spectroscopy. In a second step, the iodinated compound was oxidised with an excess of $KMnO_4$. NMR spectroscopy revealed the formation of a salt between the solvent pyridine and the desired product. The product was then reacted in a Finkelstein reaction in a microwave, but the GCMS shows just the decomposition of the starting material.

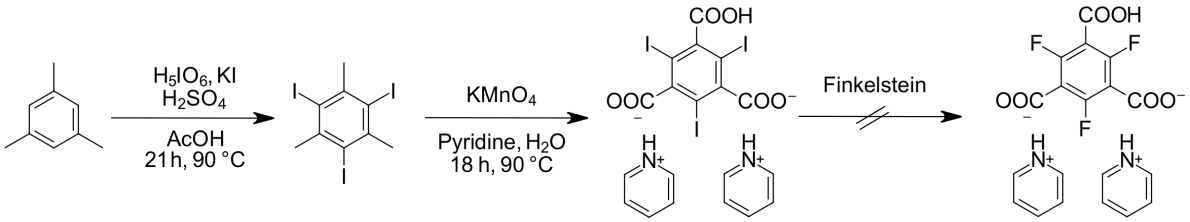

Figure 4.7: The second attemped synthesis route to prepare the perfluorinated trimesate linker.

4.1.3 Synthesis of H_3mA–BTC and attemped synthesis of H_3dA–BTC

2-aminobenzene-1,3,5-tricarboxylic acid (H_3mA-BTC) was synthesised according to *Rubin et al.* in a two-step synthesis (see Figure 4.8).[88] The initial step involved the protection of the amino group of 2,4,6-trimethylphenylamine. This was followed by the oxidation of the methyl groups with $KMnO_4$, and includes the deprotection of the amino group. This linker was obtained with a yield of 34 % over two steps and was characterised by NMR spectroscopy (see appendix on p. 131).

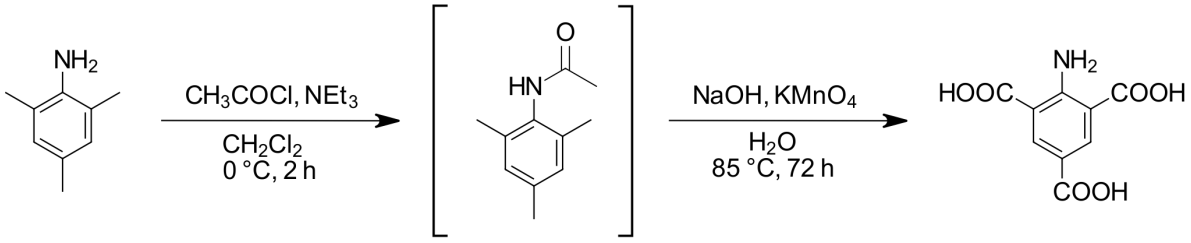

Figure 4.8: The synthesis of H_3mA-BTC.

The synthesis of 2,4-diaminobenzene-1,3,5-tricarboxylic acid (H_3dA-BTC) has not been previously described in the literature. It was tried to synthesise it for the first time via the same procedure as that used for the synthesis of H_3mA-BTC, as previously described (see Figure 4.9). However, the target linker could not be synthesised in the course of this work.

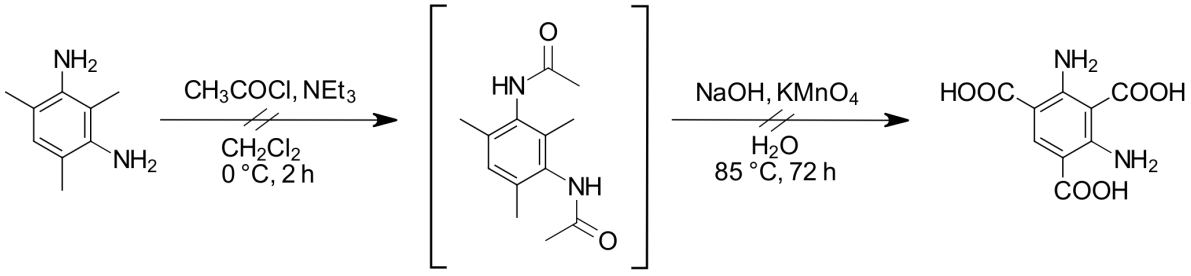

Figure 4.9: The attemped synthesis of H_3dA-BTC.

4.1.4 The Synthesis of H_3-3'-*mF*–BPTC

The synthesis of H_3-3'-*mF*–BPTC was first described by *Krautwurst*.[83] It is based on a synthesis route of unfluorinated BPTC known from the literature.[89] As shown in the Figure 4.10, the first step is a *Suzuki* coupling reaction, the product of which was then oxidised with $KMnO_4$. However, some modifications were made during the course of this work. The synthesis procedures are described in detail in the experimental section starting on p. 108.

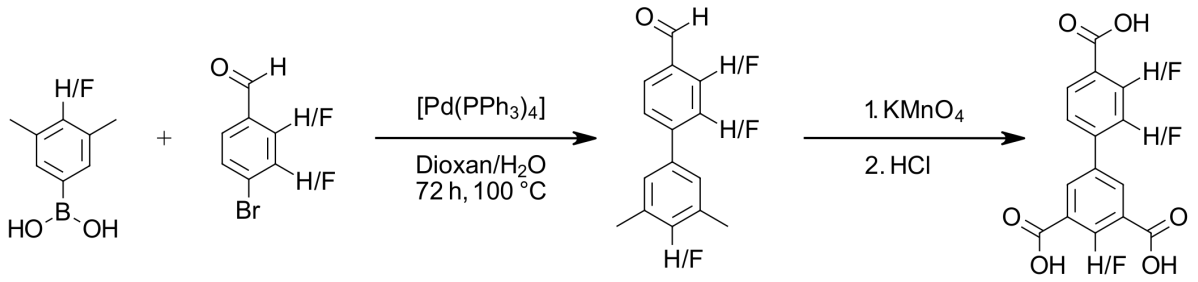

Figure 4.10: A general reaction scheme for the synthesis of fluorinated biphenyl-3,5,4'-tricarboxylic acids.

The intermediate and H_3-3'-*mF*–BPTC were characterised by NMR spectroscopy (see appendix, p. 136 and following). The analysis of the spectra showed that H_3-3'-*mF*–BPTC was successfully synthesised.

4.2 Anionic MOFs on the Basis of Fluorinated Trimesate Linkers

4.2.1 $^{3}_{\infty}[((CH_3)_2NH_2)K_2M_3(mF/dF{-}BTC)_3(H_2O)]$ (M = Zn, Co) (UoC-7)

Some results in this chapter are published in the following article,[1] with Susanna Wenzel as the first author, ©2024 Wiley-VCH GmbH:

S. Wenzel, A. E. L. Cammiade, R. K. Christoffels, S. S. Sebastian, T. Mattick, U. Ruschewitz, *Chem. Eur. J.* **2024**, *30*, e202400445. https://doi.org/10.1002/chem.202400445.

The structural analysis of Zn-UoC-7(2F) was initially described by Aimée E. L. Cammiade as part of her bachelor's thesis. The monofluorinated analogue, Zn-UoC-7(1F), was first synthesised and described in the preceding master's thesis by the first author, Susanna Wenzel. Building on this foundation, Susanna Wenzel contributed to the present research within this doctoral thesis by reproducing Zn-UoC-7(2F) to achieve a more reliable structural solution. She synthesised Co-UoC-7(2F) and also reproduced Zn-UoC-7(2F) in various solvents to explore potential template effects, completing the characterisation of these compounds through DSC/TGA and sorption measurements. The sorption measurement data were obtained by Aimée E. L. Cammiade and Ronja K. Christoffels. Adsorption enthalpies were calculated by Tim Mattick, and Hirshfeld surfaces were calculated by Sean S. Sebastian.

Structural Refinement and Analysis of Zn-UoC-7(1F) and Zn-UoC-7(2F)

The reaction of $Zn(NO_3)_2 \cdot 6\,H_2O$ with $K(H_2mF\text{–}BTC)$ and with $K(H_2dF\text{–}BTC)$ in DMF/EtOH or DMA/EtOH yielded pale yellow crystals of Zn-UoC-7(1F) and Zn-UoC-7(2F). Photographic images of the needle shaped crystals are shown in the Figure 4.11.
The crystal structure of Zn-UoC-7(1F) was characterised in a previous master's thesis[4] and that of Zn-UoC-7(2F) was first described in a previous bachelor's thesis.[3] However, in the course of this work, the previous refinements[3,4] have either been improved or augmented with additional results.

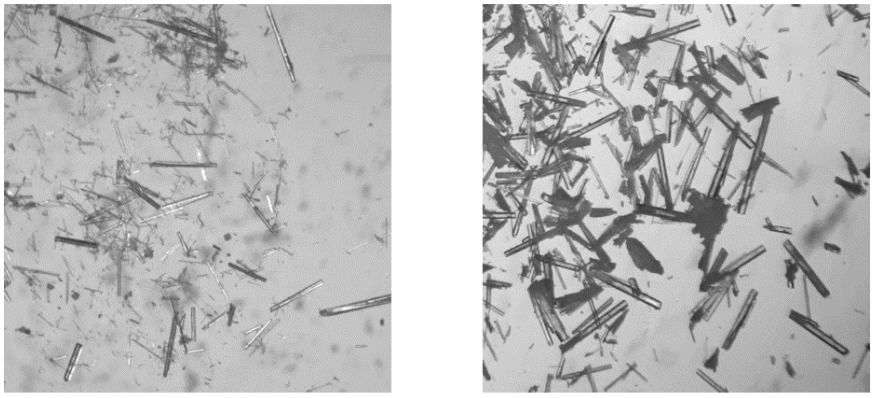

Figure 4.11: Photos of the crystals of Zn-UoC-7(1F) (left) and Zn-UoC-7(2F) (right). These photos were taken under a light microscope.

The crystal structures of Zn-UoC-7(1F) and Zn-UoC-7(2F) were solved and refined from single crystal synchrotron diffraction data recorded at beamline P24.1 of PETRA III, DESY. Selected crystallographic data for Zn-UoC-7(1F) and Zn-UoC-7(2F) are presented in the following Table 4.1 (see p. 28) and further details can be found in the attached CIF files.

Zn-UoC-7(1F) and Zn-UoC-7(2F) crystallise in the hexagonal space group $P6_3/m$ (no. 176) with two formula units per unit cell, resulting in isostructural MOFs. For Zn-UoC-7(1F), the cell parameters are $a = 17.4796(2)$ Å and $c = 10.1256(1)$ Å with a cell volume of $2679.3(6)$ Å^3. For Zn-UoC-7(2F), the cell parameters are $a = 17.4631(2)$ Å and $c = 10.1640(2)$ Å with a unit cell volume of $2684.34(8)$ Å^3.

Table 4.1: Selected crystallographic data and details of the single crystal structure analysis of Zn-UoC-7(1F)[4] and Zn-UoC-7(2F).

		Zn-UoC-7(1F)[4]	Zn-UoC-7(2F)
Formula		$C_{29}H_{16}F_3K_2NO_{19}Zn_3$	$C_{29}H_{13}F_6K_2NO_{19}Zn_3$
Crystal system		hexagonal	hexagonal
Space group (no.), Z		$P6_3/m$ (176), 2	$P6_3/m$ (176), 2
Lattice parameter	a / Å	17.4796(2)	17.4631(2)
	c / Å	10.1256(1)	10.1640(2)
	V / Å^3	2679.3(6)	2684.34(8)
R_{int}		0.1182	0.0350
R_1 (before *SQUEEZE*)		0.0575 (0.1947)	0.0376 (0.0659)
wR_2 (before *SQUEEZE*)		0.1752 (0.3712)	0.1261 (0.2241)
GooF (before *SQUEEZE*)		1.047 (1.177)	1.058 (1.125)

UoC-7 exhibits a 4,7,8T14 topology,[90] that can also be assigned to NKU-521 $[K_2Co_3(TZIA)_3(H_2O)_3]$[91] ($H_3TZIA$: 5-(1H-tetrazol-5-yl)isophthalic acid) whose composition points to large similarities to the crystal structure of UoC-7.
The following Figure 4.12 (see p. 29) illustrates a part of the crystal structure of Zn-UoC-7(1F) and Zn-UoC-7(2F), in which the thermal ellipsoids have been drawn at the 50 % probability level and all atoms of the asymmetric units have been labelled.

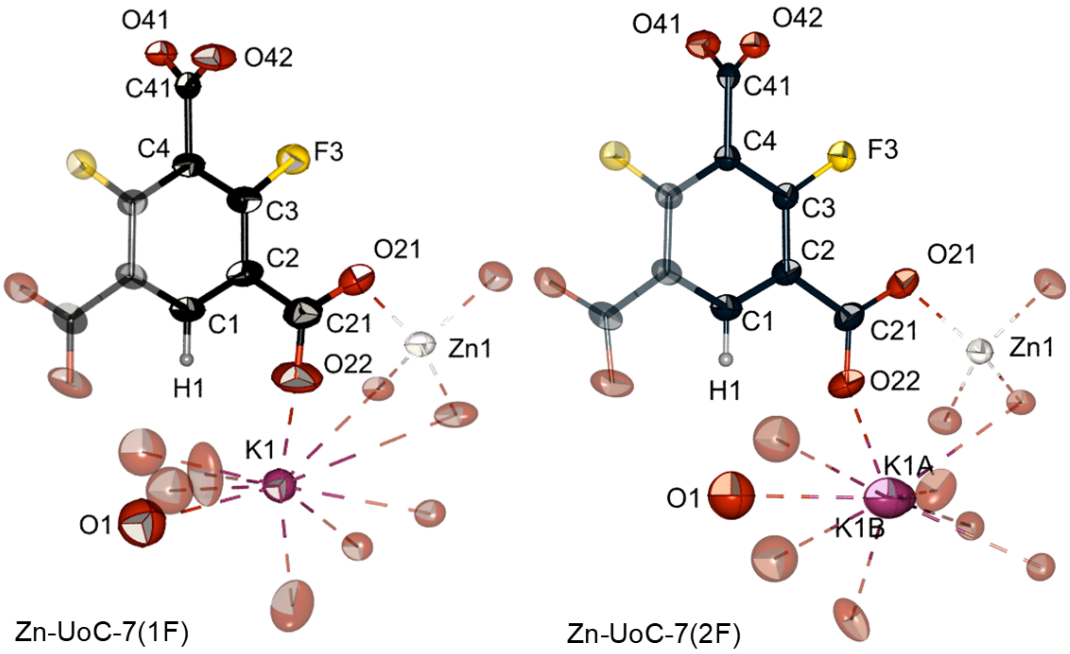

Figure 4.12: Asymmetric unit of Zn-UoC-7(1F) and Zn-UoC-7(2F). The thermal ellipsoids have been drawn at the 50 % probability level. The atoms of the asymmetric unit are labelled. Atoms that complete the linker and the coordination sphere of the metal cations are depicted in a transparent mode. Colour code: Zn (white), K (purple), O (dark red), C (black), F (yellow), and H (light grey).

For both MOFs, the asymmetric unit consist of one zinc cation (Zn1), one potassium cation (K1 or K1A/B), an incomplete linker (C1, C2, C3, C4, C41, O41, O42, C21, O21 and O22) and an oxygen atom (O1) assigned to a water molecule.
In Figure 4.12, the atoms that complete the linker are illustrated in a transparent mode, as well as the coordination sphere of the zinc and the potassium cation.
O1 of the water molecule, the zinc cation Zn1 and the linker atoms C1, C4, C41, O41, O42 and H1 occupy the *Wyckoff* position *6h*. C2, C3, C21, O21, O22 and F3, which also belong to the linker are occupying the *Wyckoff* position *12i*, while the potassium cation K1 (K1A/B) occupies the *Wyckoff* position *4f*.
In the structure of Zn-UoC-7(2F), the fluoro substituents are fully occupying the F3 position, whereas the H1 position is solely occupied by one hydrogen atom.

In contrast, the single fluoro substituent of Zn-UoC-7(1F) is disordered over the two F3 positions, with each occupied by 50 %. For both MOFs, the H1 atom was calculated by using the AFIX 43 command and positioned with the ideal distances and angles.
As described in literature,[55] the fluorine substituents of both MOFs lead to increased interplanar angles between the carboxylate groups and the phenyl rings, as can be seen in the following Figure 4.13.
In Zn-UoC-7(1F), the interplanar torsion angle for the carboxylate group between the two fluoro substituents in α position are 90°, while the other two symmetry equivalent interplanar torsion angles are 5.2°. In Zn-UoC-7(2F), similar interplanar torsion angles were observed: 90° and 4.7°.

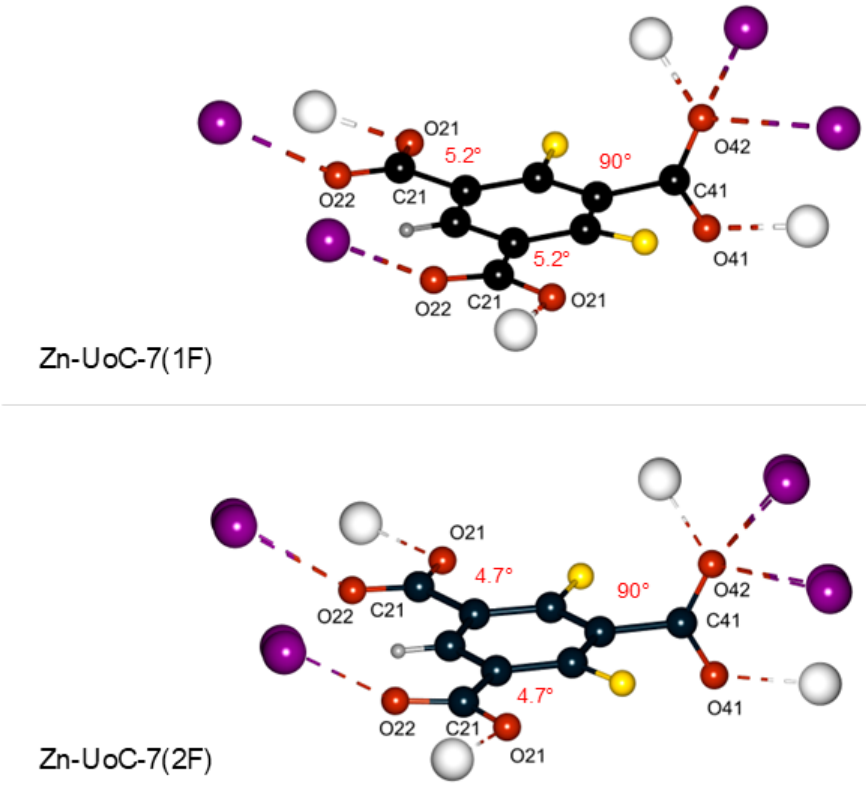

Figure 4.13: The interplanar torsion angles (red) of *mF*-BTC^{3-} in Zn-UoC-7(1F) (above) and of *dF*-BTC^{3-} in Zn-UoC-7(2F) (below). Colour code: Zn (white), K (purple), O (dark red), C (black), F (yellow) and H (light grey).

In both MOFs, the coordination sphere around the zinc cation Zn1 is a slightly distorted tetrahedron, as illustrated in the following Figure 4.14. The calculations with *SHAPE*[92] have yielded $CShM_{T-4} = 0.429$ for Zn-UoC-7(1F) and $CShM_{T-4} = 0.279$ for Zn-UoC-7(2F).

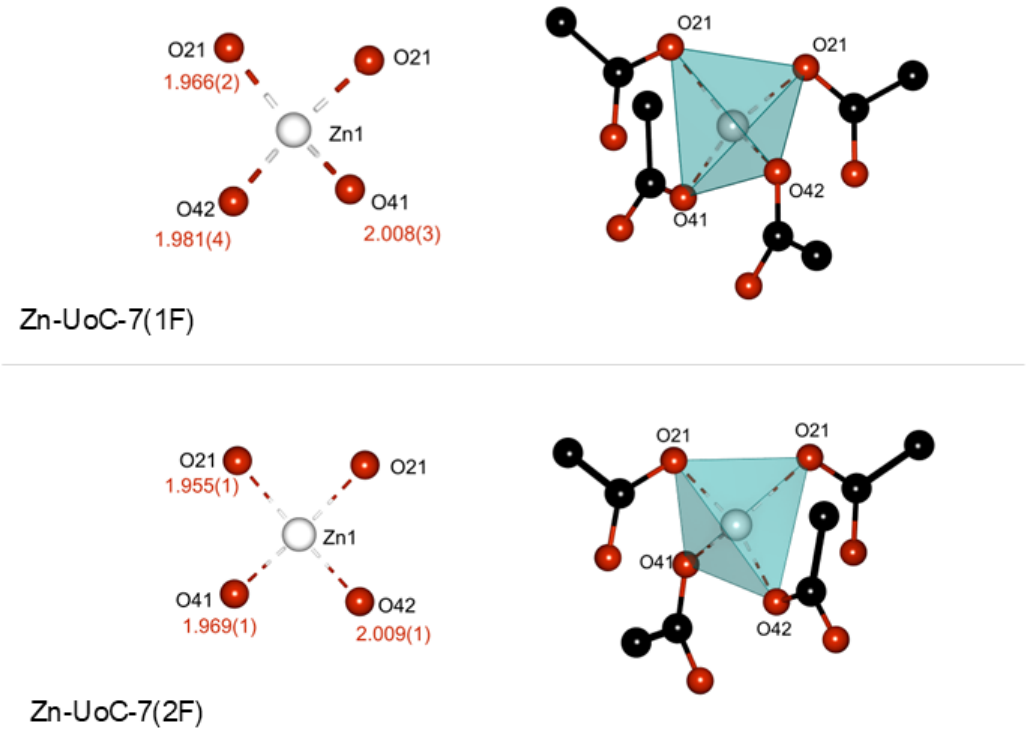

Figure 4.14: The coordination spheres around Zn1 with labelling of Zn–O distances (Å, red). Colour code: Zn (white), O (dark red), C (black) and tetrahedron (blue, semi-transparent).

The largest deviations from an ideal tetrahedral symmetry are observed for the oxygen atom (O42), which is also connected to the potassium cation (K1), whereas the other three oxygen atoms of the tetrahedrons are solely bound to the Zn1 cation.
In the course of this work, the potassium cation (K1) was refined with a disorder along the *c* axis, resulting in K1A and K1B. This improved the refinement of the crystal structure of Zn-UoC-7(2F) significantly, but not that of Zn-UoC-7(1F).

The coordination number of the potassium cation (K_1) is seven. This results in the formation of a KO_7 polyhedron, where six of the seven oxygen atoms are derived from six distinct carboxylate groups. The seventh ligand is a water molecule, whose oxygen atom (O_1) is disordered over three positions with an occupancy of 1/3.
The KO_7 polyhedra are connected via oxygen atoms (O1) forming strands along the *c* axis (see Figure 4.15). The K–O distances were found to range from 2.525(1) Å to 3.118(4) Å. However, due to the disorder of K1A/K1B and O1, a detailed and reasonable discussion of these distances is not possible.

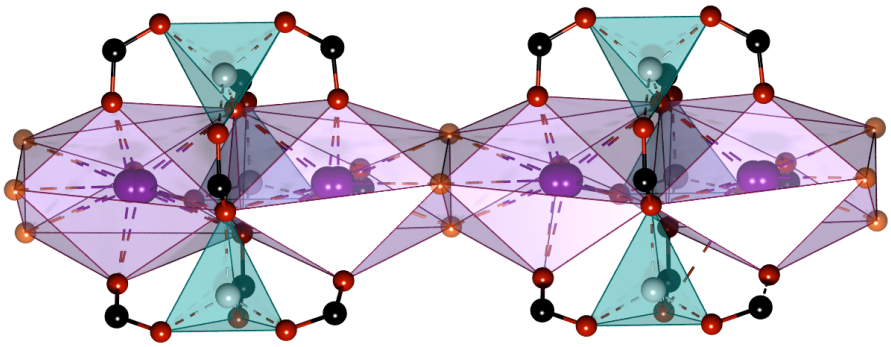

Figure 4.15: Part of the structure of Zn-UoC-7(2F) showing the connection of the Zn-SBU to the potassium oxygen strands. Disordered water molecules (O1) are depicted orange, otherwise the following colour code applies: Zn (white), K (purple), O (dark red), C (black) and F (yellow).

The potassium oxygen chain is vertically linked to other potassium oxygen chains and further ZnO_4 tetrahedra by the BTC^{3-} linkers. These interconnections result in an overall structure with large honeycomb channels along [001], as shown in the following Figure 4.16 (see p. 33). The approximate diameter of these channels is 11.7 Å, taking into account the van der Waals radii. The channels are filled with the disordered $(CH_3)_2NH_2^+$ cations and solvent molecules that remain from the synthesis.

The solvent-accessible volume was calculated using the SQUEZZE[66] option within *PLATON*.[93] The volume was calculated to be 1263 $Å^3$ for Zn-UoC-7(1F) and 1240 $Å^3$ for Zn-UoC-7(2F). These results are in accordance with the slightly larger volume of a fluoro substituent compared to a hydrogen substituent.
Furthermore, it was attempted to localise the cation from single crystal structure analysis, despite the fact that this was not successful for the majority of the anionic MOFs that were known from the literature. This attempt was based on to the high quality of the dataset obtained for Zn-UoC-7(2F) at a synchrotron source.
Indeed, a residual electron density was identified, which was successfully assigned to a cation with the chemical formula $(CH_3)_2NH_2^+$. The nitrogen atom N1 was found to reside on the *Wyckoff* position *6h*. Its occupancy was refined to 1/3, in accordance with the expected charge compensation of the anionic framework. This implies that only every third $(CH_3)_2NH_2^+$ cation position is occupied.
A similar cation position was found for Zn-UoC-7(1F), although the quality of this dataset is significantly lower.
In the following Figure 4.16, the cations are shown in the illustration of a single pore of Zn-UoC-7(1F) and Zn-UoC-7(2F).

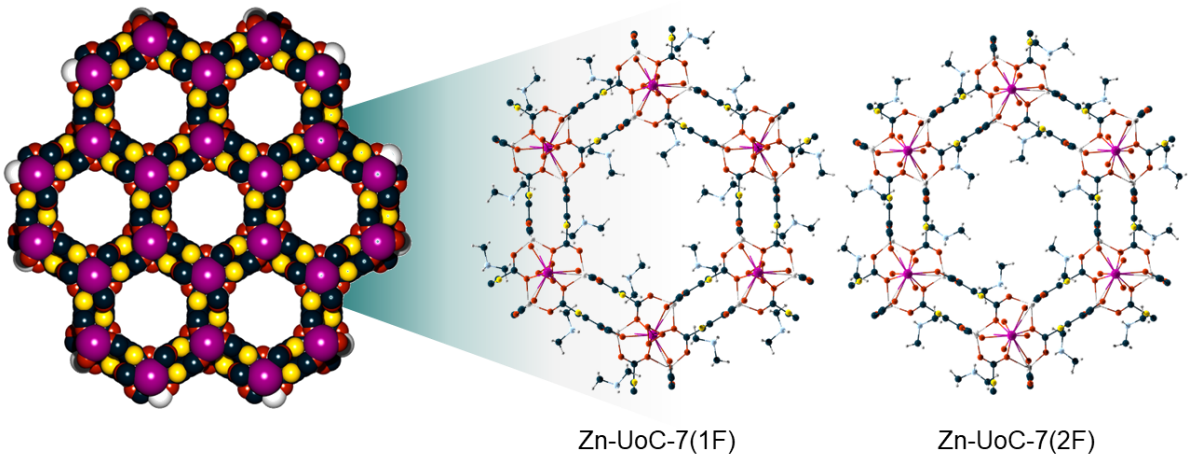

Figure 4.16: Section of the crystal structure of Zn-UoC-7 in a projection along [001] showing large channels in this direction. In the space filling model (left), atoms are drawn with their respective van der Waals radii, solvent molecules and $(CH_3)_2NH_2^+$ cations are omitted. The $(CH_3)_2NH_2^+$ cations are shown in the single pores (right). Colour code: Zn (white), K (purple), O (dark red), C (black), F (yellow), N (blue) and H (light grey).

Despite several restraints of the cations, no convergent refinement was obtained. Consequently, the refinement of the cations was not included into the final refinements of Zn-UoC-7(1F) and Zn-UoC-7(2F).
A Hirshfeld isosurface was nevertheless calculated for the $(CH_3)_2NH_2^+$ cation, which was found to be located within the pores of Zn-UoC-7(2F). This calculation demonstrates that all contacts between the cation and the anionic framework, or between two cations, are reasonable (see Figure 4.17). Moreover, the presence of red spots indicates that the partially positively charged protons of the cations are involved in the interactions with oxygen atoms of the carboxylate groups of the MOF framework. This confirms that the cation position is highly plausible.

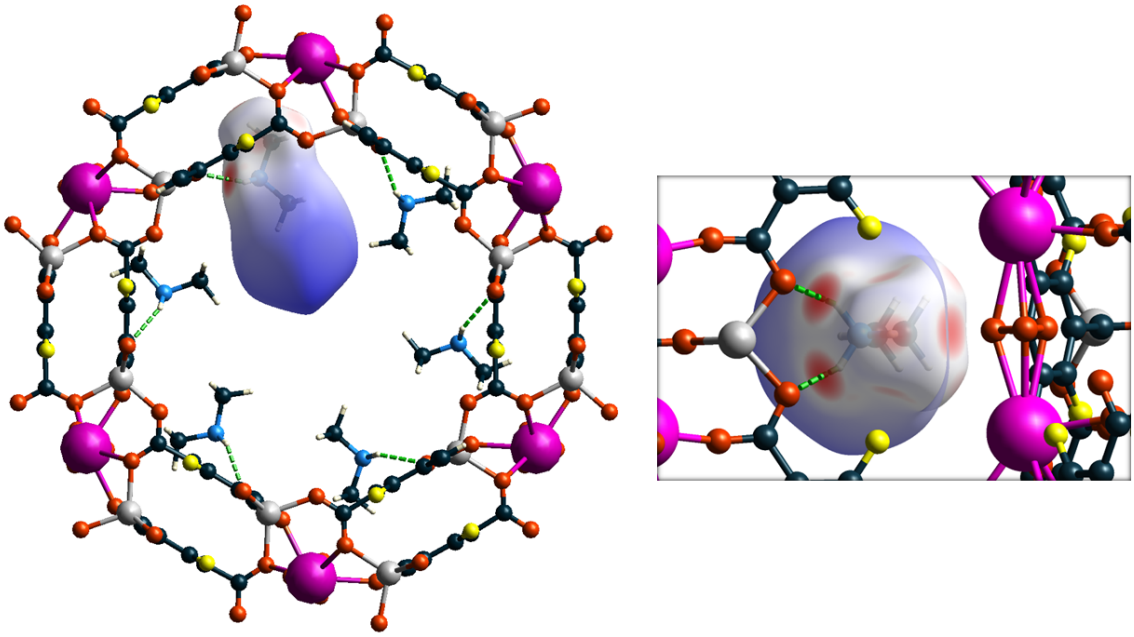

Figure 4.17: One channel of Zn-UoC-7(2F) (view along [001]) with disordered $(CH_3)_2NH_2^+$ cations. For one cation a calculated Hirshfeld surface is shown. Red spots indicate interactions between the cation and the anionic framework. Right: a close up of the illustrated Hirshfeld surface of one cation is shown. Colour code: Zn (white), K (purple), O (dark red), C (black), F (yellow), N (blue) and H (light grey).

Zn-UoC-7(1F) and Zn-UoC-7(2F) crystallise phase pure, which show the respective PXRD patterns (see Figure 4.18).

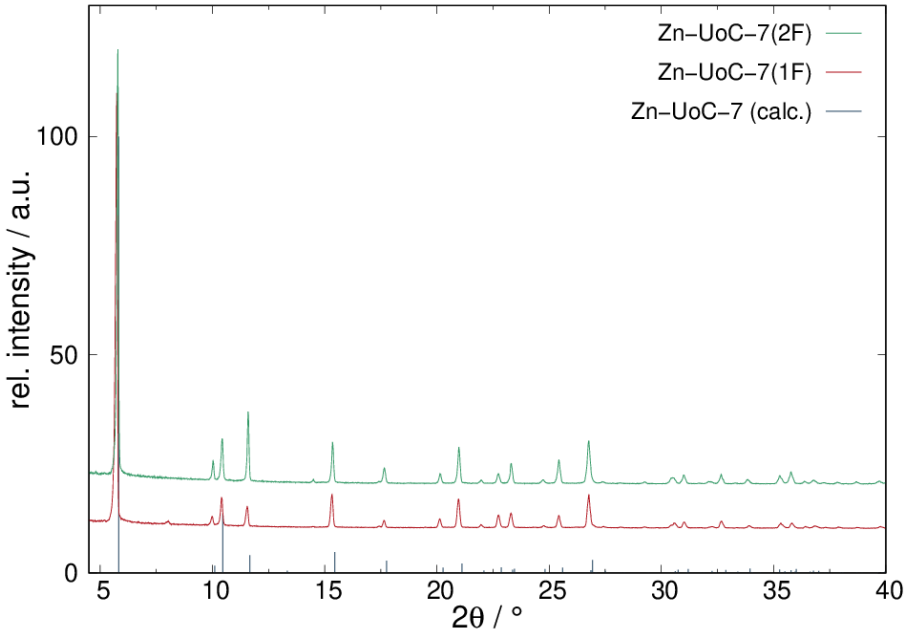

Figure 4.18: PXRD patterns of Zn-UoC-7(1F) (red) and Zn-UoC-7(2F) (green) synthesised in DMA/EtOH and DMF/EtOH, respectively. (*Rigaku MiniFlex600-C*, Cu Kα radiation (λ = 1.5418 Å)). For comparison, the calculated reflection positions and intensities from the single crystal data of Zn-UoC-7(2F) as a line diagram (black).

In order to corroborate the existence of the $(CH_3)_2NH_2^+$ cations, a control experiment was conducted, which was derived from the fact that the respective solvents (DMF, DEF, DMA) undergo an (acidic) hydrolysis to form the respective cations.[94]
It was investigated whether Zn-UoC-7(2F) would also form in a mixture of propylene carbonate (PC) and EtOH, which are unable to form such cations. This control experiment yielded in an amorphous solid.

In another approach, the counter cation was added in the form of $[(CH_3)_2NH_2]Cl$ to the synthesis in the solvent mixture PC/EtOH. The PXRD (see in the appendix, on p. 131) clearly shows that Zn-UoC-7(2F) has been formed under the specified synthesis conditions. This confirms that $(CH_3)_2NH_2^+$ is an integral component of the structure of Zn-UoC-7(2F).

It was also possible to synthesise Zn-UoC-7(2F) in DEF and DBF, where their hydrolysis produced larger cations: $(C_2H_5)_2NH_2^+$ and $(C_4H_9)_2NH_2^+$ (see Figure 4.19). Despite higher spatial demand, no templating effect was found. Instead, a slight increase of the lattice parameters was detected Especially in the (001) plane, there is an increase of the lattice parameter a by more than 0.8 %, whereas the increase of the c parameter is in the range of 0.4 - 0.6 % (see Table 4.2, p. 37).

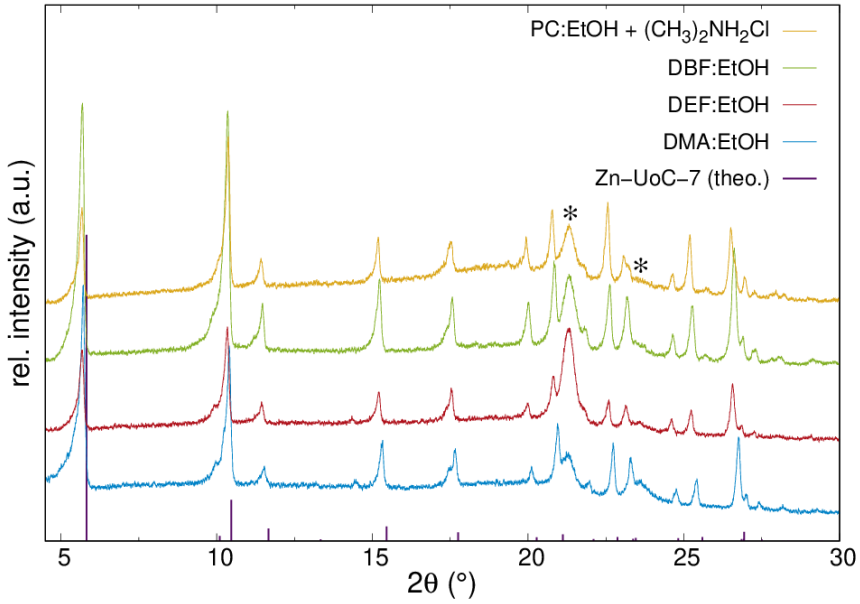

Figure 4.19: Comparison of the PXRD patterns of Zn-UoC-7(2F) synthesised with different counter cations (*Huber G670*, Cu Kα_1 radiation (λ = 1.5406 Å), *: additional reflections due to the foil of the sample holder). For comparison, the calculated reflection positions and intensities from the single crystal data of Zn-UoC-7(2F) as a line diagram.

Table 4.2: Lattice parameters of Zn-UoC-7(2F) compounds with different $R_2NH_2^+$ cations. The lattice parameters were obtained by *Le Bail fits* of the respective PXRD patterns.

Cation	a / Å	c / Å	V / Å^3
$(CH_3)_2NH_2^+$	17.5694(4)	10.1068(3)	2701.8(1)
$(C_2H_5)_2NH_2^+$	17.6888(5)	10.1657(5)	2754.6(2)
$(C_4H_9)_2NH_2^+$	17.7177(5)	10.1419(4)	2757.2(1)

Furthermore, the anionic framework of UoC-7 permits the post-synthetic exchange of the $(CH_3)_2NH_2^+$ cation with alkali metal cations such as Cs^+. Cs^+ is of particular interest due to the contamination of seawater with $^{137}Cs^+$ ions following the Fukushima nuclear disaster. A MOF capable of selectively adsorbing Cs^+ cations could potentially be utilised for seawater decontamination.
To evaluate UoC-7 for this application, its stability in water was assessed, as the Cs^+ cation exchange occurs in an aqueous medium. For this purpose, Zn-UoC-7(2F) was suspended in water and analysed via X-ray powder diffraction (see appendix, p. 141), which shows that this MOF is unstable in water. As a result, no further investigations were conducted.

Thermal Behaviour of Zn-UoC-7(1F) and Zn-UoC-7(2F)

The thermal behaviour of Zn-UoC-7(1F) was investigated for the first time in a previous master's thesis,[4] while the thermal behaviour of Zn-UoC-7(2F) was first investigated in a previous bachelor's thesis.[3] The results were reproduced and further analysed in the course of this work. The differential scanning calorimetry (DSC)/thermogravimetric analysis (TGA) curves of both MOFs are shown in the following Figure 4.20. To analyse the solvent release in more detail, a coupled DSC-TGA-MS measurement of Zn-UoC-7(2F) was conducted, which can be seen in the appendix (see p. 143).

In both curves, the mass loss starts below 100 °C, indicating the release of volatile solvents, most likely water or EtOH, which are part of the synthesis.
Below 100 °C, the coupled DSC-TGA-MS measurement of Zn-UoC-7(2F) shows a weak ion current for m/z = 18 and no significant ion current for m/z = 46. This indicates the presence of water in the pores of Zn-UoC-7(2F), while the presence of EtOH can be excluded. Therefore, the mass loss observed below 100 °C for Zn-UoC-7(2F) can be attributed to the release of water molecules.
For Zn-UoC-7(1F), the TGA curve shows an inflection point at approximately 300 °C, which corresponds with an exothermic signal observed in the DSC curve. Up to this temperature, a relative mass loss of about 23 % is observed, which is likely due to the release of DMF from the pores. Given that the release of one DMF molecule per formula unit would result in a mass loss of approximately 8 %, it can be inferred that the total mass loss up to around 300 °C corresponds to the release of two to three DMF molecules. The *SQUEEZE*[95] routine of *PLATON*[93] calculated 381 remaining electrons in solvent-accessible voids of the unit cell. This number corresponds to the presence of approximately eight DMF molecules in the unit cell, considering two $(CH_3)_2NH_2^+$ cations (with Z = 2, $2 \cdot 26$ electrons). However, the DSC/TGA measurements indicated just two to three DMF molecules. This discrepancy may be explained by the fact that the sample, which was filtered a few weeks prior to the DSC/TGA measurements, might have lost solvent molecules during storage.
However, the interpretation of this mass loss is complicated by the decomposition of $(CH_3)_2NH_2^+$ cations, which also begins within this temperature range and continues up to approximately 400 °C. Above 400 °C, the TGA curve of Zn-UoC-7(1F) shows a plateau, suggesting that further significant mass loss does not occur.
Therefore, it is likely that Zn-UoC-7(1F) begins to decompose from the inflection point at approximately 300 °C and continues up to 400 °C.

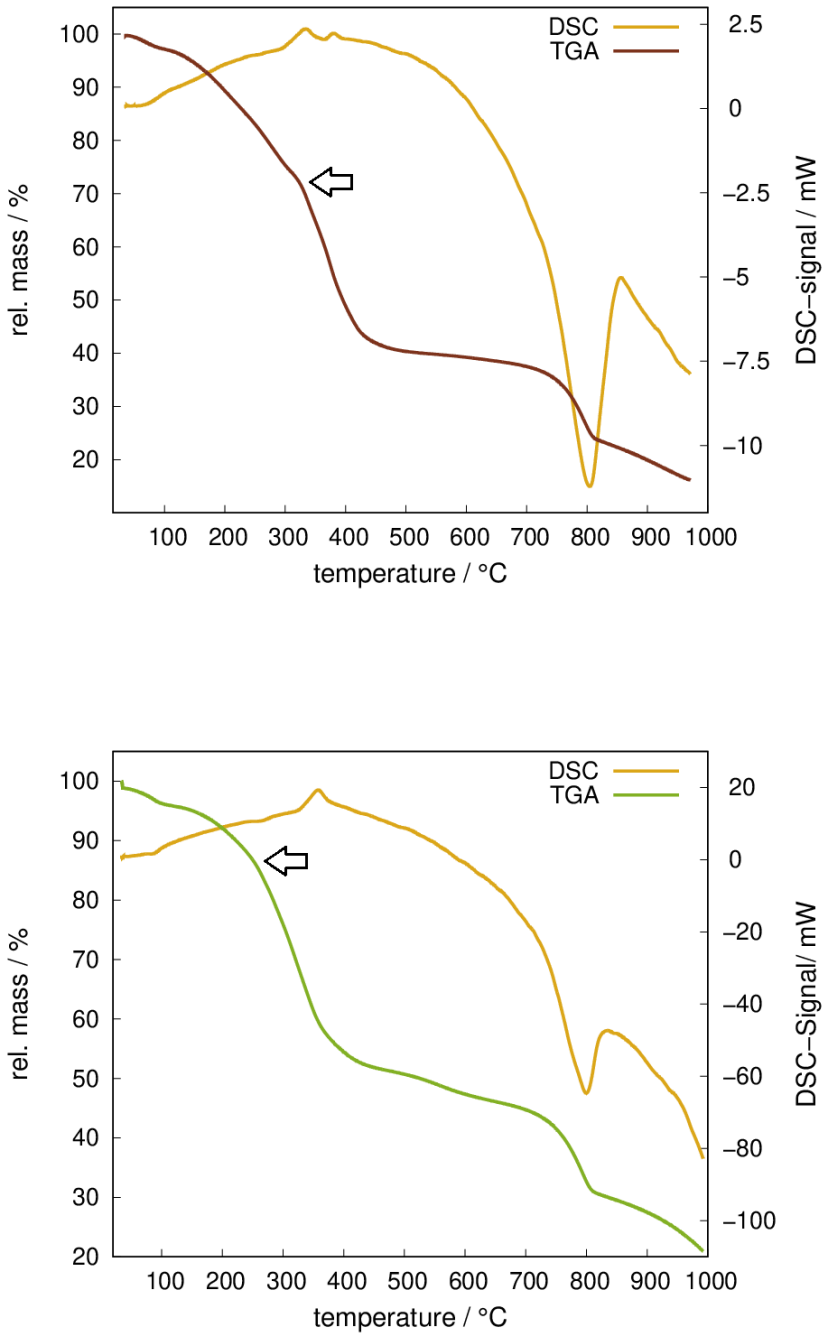

Figure 4.20: The DSC/TGA curves of Zn-UoC-7(1F) (top) and Zn-UoC-7(2F) (bottom) were recorded while heating at a rate of 10 °C/min under a steady flow of argon gas, up to a maximum temperature of 1000 °C. The arrows are intended to indicate where the decomposition of the MOFs is estimated to occur.

For Zn-UoC-7(2F), the TGA curve shows no inflection point until approximately 400 °C. At around 260 °C to 280 °C, the TGA curve exhibits a more pronounced decline, which is more clearly visible in the derivative thermogravimetry (DTG) curve of Zn-UoC-7(2F) (see appendix, p. 145). This suggests that Zn-UoC-7(2F) begins to decompose at this temperature. Up to this point, a relative mass loss of 16 % is observed, likely due to the release of DMA molecules from the pores. However, the interpretation of this part of the TGA curve is complicated by the probability that the release of the solvent will merge with the decomposition of the MOF via decarboxylation.
The results of the coupled DSC-TGA-MS measurement of Zn-UoC-7(2F) confirm these interpretations (appendix, p. 143). Until approximately 300 °C, the signature of DMA with the molecular ion (M^+) peak (m/z = 87) and the acetyl group (m/z = 43), which is its main decomposition product, can be observed.
Between 260 °C and 400 °C, three characteristic peaks follow, visible at m/z = 44 and m/z = 46 pointing to a three-step release of the $(CH_3)_2NH_2{}^+$ cation ($M((CH_3)_2NH_2{}^+) = 46.09\,g\,mol^{-1}$) and a starting decarboxylation of the MOF framework ($M(CO_2) = 44.01\,g\,mol^{-1}$).
The *SQUEEZE*[66] option within *PLATON*[93] estimates 186 electrons residing in the pores of Zn-UoC-7(2F). Assuming three DMA molecules and two $(CH_3)_2NH_2{}^+$ cations (2·26 electrons (with Z = 2)), a total of 196 electrons are calculated. This would be in good agreement with the TGA analysis, if the relative mass loss observed up to 300 °C is attributed solely to the release of DMF molecules.

Finally, an exothermic signal can be observed in the DSC curves of both MOFs at approximately 400 °C. At this temperature, the TGA curves show a plateau up to approximately 700 °C.
The relative mass loss observed above 700 °C is accompanied by strong endothermic signals in the DSC curves, which is more pronounced for Zn-UoC-7(2F) than for Zn-UoC-7(1F). A residue mass of about 32–33 % is calculated. K_2O melts at 740 °C, which corresponds to the strong endothermic signal observed above 700 °C, so the formation of K_2O/ZnO was assumed as the final residue. Unfortunately, after heating at 1000 °C, the residue was found to be almost amorphous (see Figure 4.21). The two weak reflections observed could not be assigned to K_2O or ZnO. Therefore, the residue was not further characterised. The residue after heating to 500 °C was a crystalline powder, but it could not be identified by its PXRD pattern (see Figure 4.21).

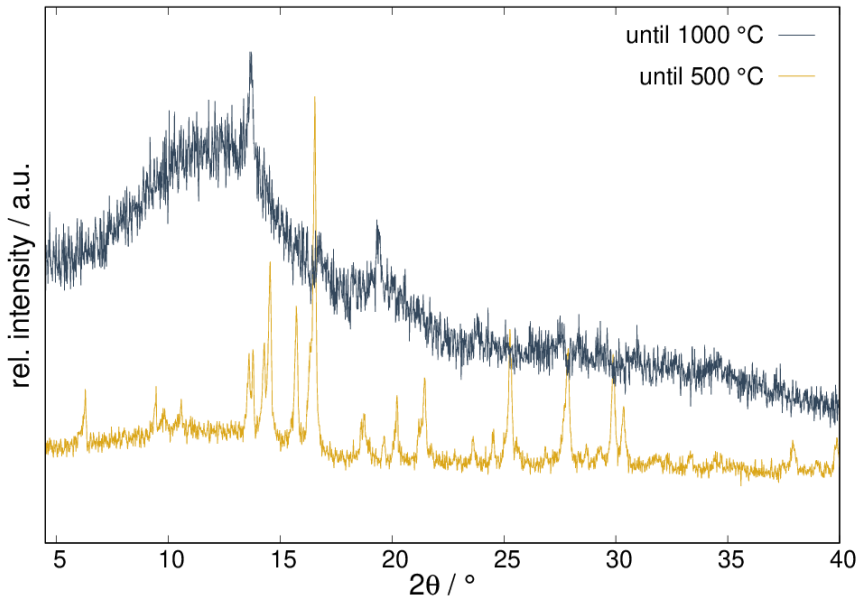

Figure 4.21: PXRD of the residues of Zn-UoC-7(2F) after DSC/TGA measurements up to 500 °C (yellow) and up to 1000 °C (blue).

Adsorption Behaviour of Zn-UoC-7(1F) and Zn-UoC-7(2F)

The porosity of Zn-UoC-7 was analysed using N_2 and CO_2 sorption measurements. The isotherms of N_2 adsorption and desorption that were measured after different activation temperatures (each for 24 h in high vacuum) are shown in the appendix (see p. 147 and following). For Zn-UoC-7(1F) and Zn-UoC-7(2F), the highest BET surface areas were obtained after an activation at 200 °C for 24 h under high vacuum (1 $\times 10^{-7}$ mbar). The two respective N_2 sorption isotherms are compared in the following Figure 4.22.

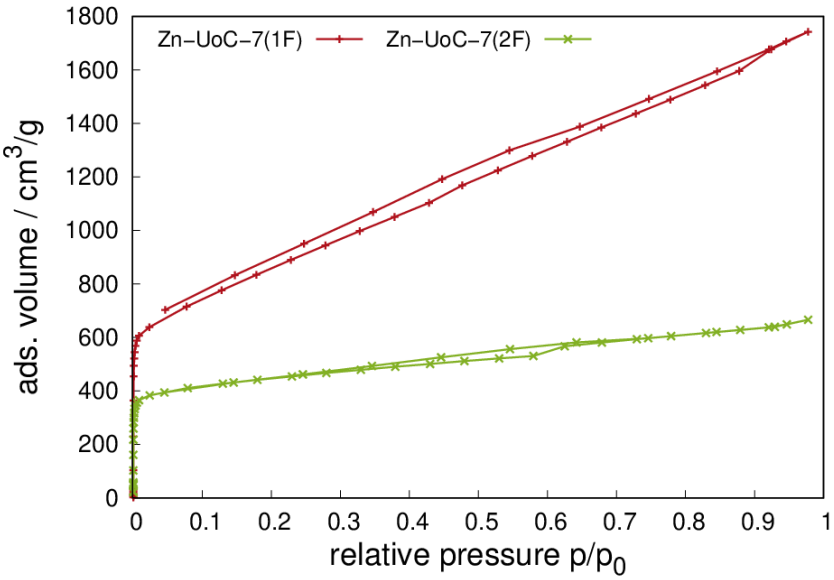

Figure 4.22: N_2 gas sorption isotherms of Zn-UoC-7(1F) (red) and Zn-UoC-7(2F) (green) measured at 77 K after activation at 200 °C for 24 h in high vacuum.

The isotherm observed for Zn-UoC-7(2F) is of type I(a), which is characteristic for microporous materials. In contrast, the isotherm of Zn-UoC-7(1F) initially assumes a type I(a) shape in the beginning, but does not reach saturation, which is unusual for microporous materials. It resembles that of type II isotherms, which is among others typical for macroporous materials, where multilayer sorption occurs. Zn-UoC-7(1F) is not a macroporous material, but it seems reasonable to suggest that the pore of Zn-UoC-7(1F) is sufficiently large to allow more gas molecules to be adsorbed after the first layer. However, at this time, there is no sufficient explanation for the unusual N_2 adsorption isotherm of Zn-UoC-7(1F), which was reproducible in multiple experiments. The specific BET surface area of Zn-UoC-7(1F) was determined to be $S_{BET} = 2740$ m²/g, while that of Zn-UoC-7(2F) was found to be lower at $S_{BET} = 1643$ m²/g. Both S_{BET} values indicate a highly porous MOF.
The following Figure 4.23 shows the PXRD of both MOFs after the N_2 sorption measurements.

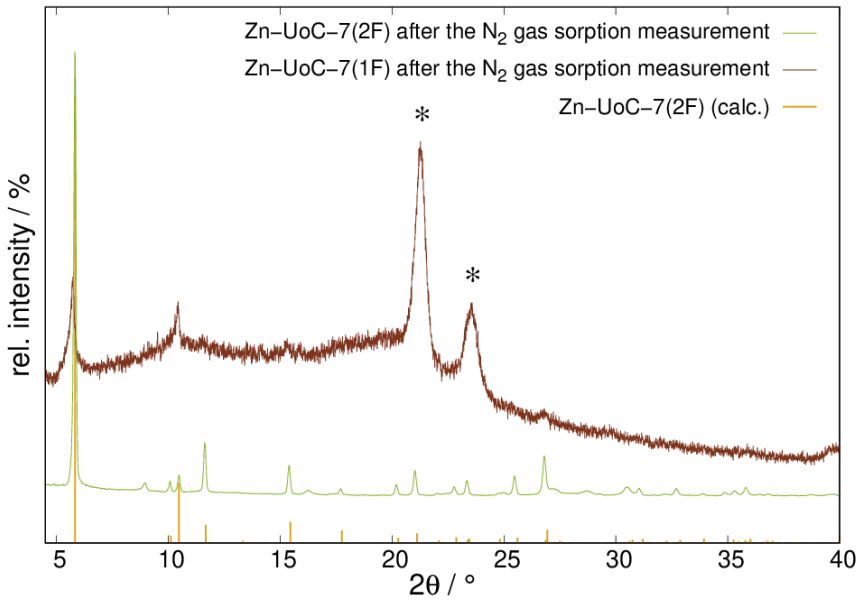

Figure 4.23: PXRD of Zn-UoC-7(1F) (red, *Huber G670*, Cu Kα_1 radiation ($\lambda = 1.5406$ Å), *: additional reflections due to the foil of the sample holder) and Zn-UoC-7(2F) (green, *Rigaku MiniFlex600-C*, Cu Kα radiation ($\lambda = 1.5418$ Å)) after the N_2 sorption measurements compared with the calculated reflection positions and intensities from the single crystal data of Zn-UoC-7(2F).

Only the three most intense reflections of Zn-UoC-7(1F) could be identified as broad signals. The presence of a very high background indicates a significantly decreased crystallinity. In contrast, the PXRD of Zn-UoC-7(2F) shows the expected sharp reflections indicating the persistence of crystallinity after the gas sorption measurement.
In the appendix (see p. 131), the pore size distribution obtained from N_2 gas sorption measurements is given. The results are similar for Zn-UoC-7(1F) and Zn-UoC-7(2F). Both show a maximum at a pore diameter of approximately 7.5 Å, which is significantly smaller than the diameter obtained from the single crystal structure analysis of the framework. The latter does not consider the positions of the cations, which obviously reduce the accessible pore size.
Moreover, CO_2 sorption measurements were conducted on Zn-UoC-7(1F) and Zn-UoC-7(2F).
NKU-521,[91] which has the same topology as UoC-7, was found to be a good adsorbent

for CO_2, so the same was assumed for UoC-7.
The isotherms, which were measured at 273 K and 293 K respectively, are shown in the following Figure 4.24. Prior to the measurement, both MOFs were activated at 200 °C for 24 h.

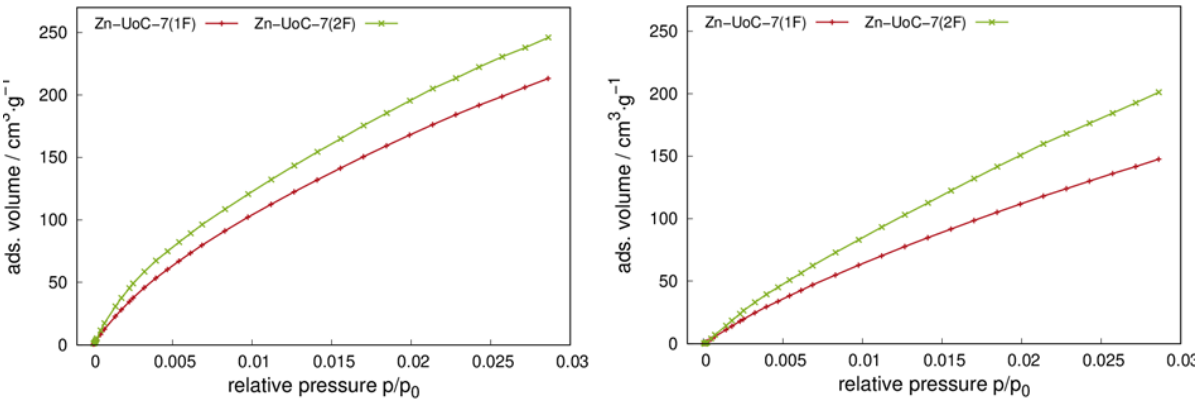

Figure 4.24: The comparison of the CO_2 gas sorption isotherms of Zn-UoC-7(1F) (red) and Zn-UoC-7(2F) (green) measured at 273 K (left) and 293 (right) after activation at 200 °C for 24 h in high vacuum.

At 273 K and a relative pressure of 0.028 bar, the CO_2 uptake of Zn-UoC-7(1F) reaches a value of 213 cm^3/g, while the CO_2 uptake of Zn-UoC-7(2F) reaches a value of 247 cm^3/g. Very remarkably, Zn-UoC-7(2F) shows one of the highest CO_2 uptakes reported to this day, even surpassing the CO_2 benchmark material Mg_2(DOBDC) (H_4DOBDC: 2,5-dihydroxyterephthalic acid) with its very high uptake of 225 cm^3/g.[2]
One potential explanation for this phenomenon is the narrow pore size and the stronger interactions between the fluoro substituents of the linker and the CO_2 guests. It has been demonstrated that optimising the pore size can lead to a significant enhancement in the uptake of small molecules such as CO_2.[96] It was thus concluded that MOFs with narrow pore diameters (less than 7 Å) should be ideal sorbents for small molecule sorbates. Considering the positions of the cations, the pore sizes of Zn-UoC-7(1F) and Zn-UoC-7(2F) are in close proximity to this "ideal" pore size.
At 293 K and a pressure of 0.028 bar, the CO_2 uptake of Zn-UoC-7(1F) reaches a value of 148 cm^3/g, while the CO_2 uptake of Zn-UoC-7(2F) reaches a value of 201 cm^3/g. These values are lower than those obtained at 273 K, which shows that the uptake depends on

the measuring temperature.
Moreover, the data indicate that an increase in fluorination of the linker results in a significant enhancement of CO_2 uptake, which is consistent with previous observations for other MOFs and CPs.[52,56] Apparently, the van der Waals (dispersion) interactions between the CO_2 guest and the MOF framework increase with a higher number of fluoro substituents of the linker.[52] As expected, this effect is more pronounced for CO_2 than for N_2 or H_2.[52]
Since Zn-UoC-7(2F) shows a remarkably high CO_2 uptake, five cycles of CO_2 ad- and desorption were measured. The corresponding isotherms, which were recorded at 273 K, are illustrated in Figure 4.25 (see on p. 45).
After five cycles of CO_2 adsorption and desorption, no significant reduction in CO_2 uptake was observed, demonstrating the stability of Zn-UoC-7(2F). Subsequently, the residue from these measurements was analysed using PXRD (see Figure 4.25). Immediately after the measurement, with empty pores, Zn-UoC-7(2F) exhibited reduced crystallinity. However, after suspending the residue in DMA, the PXRD revealed the characteristic pattern of Zn-UoC-7(2F). These results confirmed that the crystalline structure of Zn-UoC-7(2F) remained intact following the five cycles of CO_2 adsorption and desorption.

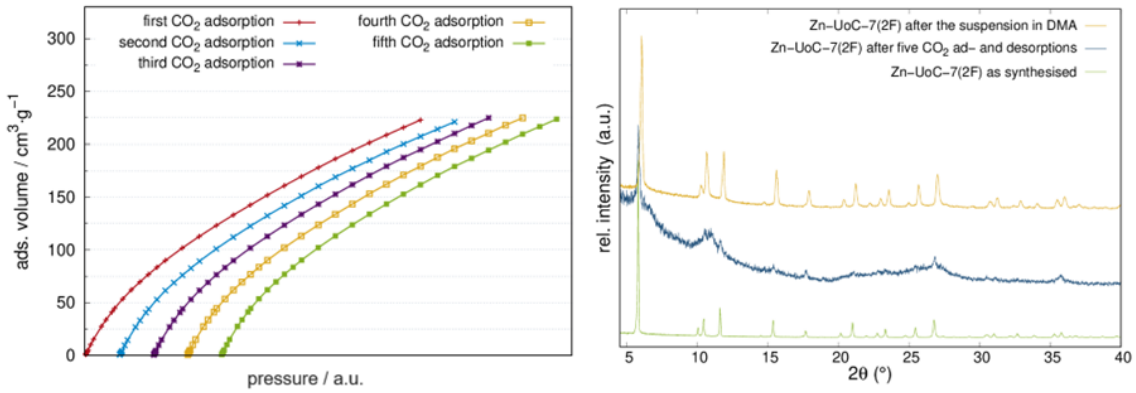

Figure 4.25: Left: cycles of CO_2 gas sorption measurements on Zn-UoC-7(2F) with a off-set along the x axis. Right: PXRD of Zn-UoC-7(2F) after five cycles of CO_2 gas sorption measurements (blue) and after suspending in DMA (pink) (*Rigaku MiniFlex600-C*, Cu Kα radiation (λ = 1.5418 Å)).

In conclusion, the isosteric enthalpies of CO_2 adsorption for Zn-UoC-7(1F) and Zn-UoC-7(2F) were determined. The respective virial fits[97] are presented in the appendix (see p. 131). The isosteric enthalpy of adsorption ΔH^0_{ads} of Zn-UoC-7(1F) has a value of $-35(2)\,\mathrm{kJ/mol}$, while ΔH^0_{ads} of Zn-UoC-7(2F) has a value of $-49(4)\,\mathrm{kJ/mol}$. ΔH^0_{ads} increases with the number of fluorine substituents of the linker, thus corroborating the higher CO_2 uptake of Zn-UoC-7(2F) compared to Zn-UoC-7(1F). Furthermore, the ΔH^0_{ads} of Zn-UoC-7(2F) has a remarkably high value, higher than that of Mg_2(dobdc) ($\Delta H^0_{ads} = -42\,\mathrm{kJ/mol}$).[2] However, it is essential to consider the high standard deviations of such determinations, which have only been barely given in the literature.

Exchange of the transition metal cation

It was possible to synthesise a difluorinated analogue with Co^{2+} cations, referred to as Co-UoC-7(2F). For this, $Co(NO_3)_2 \cdot 6\,H_2O$ was reacted with K(H_2dF-BTC), yielding a crystalline, purple powder (see Figure 4.26). Attempts to isolate single crystals from this powder failed, however, the PXRD of Co-UoC-7(2F) unambiguously confirmed that it crystallises isostructurally with Zn-UoC-7(1F) and Zn-UoC-7(2F).

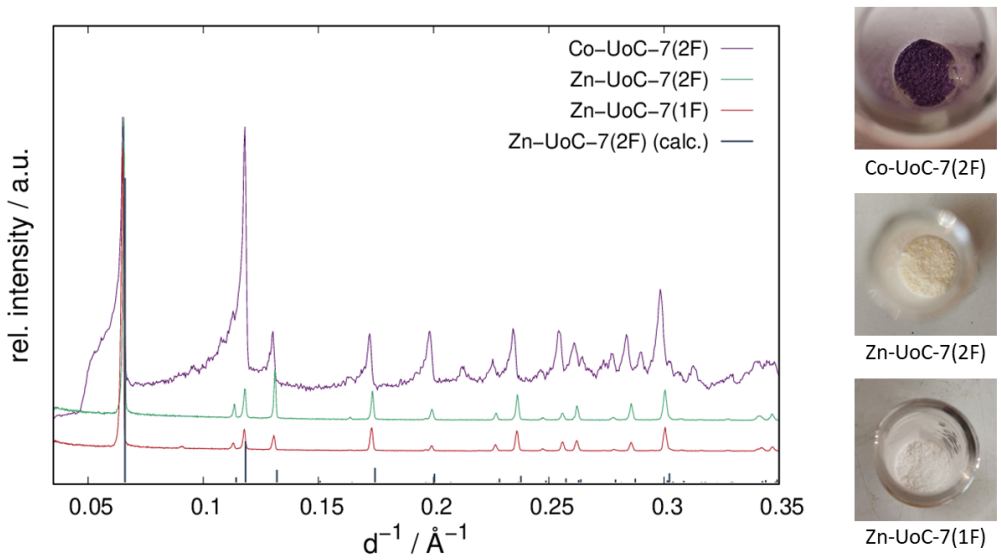

Figure 4.26: The comparison of the measured PXRD patterns of Zn-UoC-7(1F)(red), Zn-UoC-7(2F) (green curve) (*Rigaku Miniflex600-C*, Cu Kα radiation (λ = 1.5418 Å)) and Co-UoC-7(1F) (purple) (Stoe Stadi P, Mo Kα_1-radiation (λ = 0.71069 Å)). For comparison, the calculated reflection positions and intensities from the single crystal data are given as a line diagram (blue), simulated from the crystal structure of Zn-UoC-7(2F).

Approaches to synthesise further derivatives from divalent metal cations, such as Cu^{2+} and Mg^{2+}, have not been successful to date. However, for all three UoC-7 derivatives different synthesis conditions were required, which are summarised in Table 4.3. Therefore, it is plausible that further optimisation of the parameters could lead to the formation of derivatives with other metal cations in the future.

Table 4.3: A comparison of the selected synthesis parameters for the syntheses of Zn-UoC-7(1F), Zn-UoC-7(2F) and Co-UoC-7(2F).

	Zn-UoC-7(1F)	Zn-UoC-7(2F)	Co-UoC-7(2F)
solvent mixture	DMA:EtOH 1:2	DMF:EtOH 1:2	DMA:EtOH 1:2
reaction temperature	95 °C	100 °C	95°C
dwell time	48 h	48 h	48 h
cooling time	48 h	72 h	72 h

4.2.2 $^{3}_{\infty}[((CH_3)_2NH_2)_3In_3(mF\text{–}BTC)_4]$ (UoC-13(1F))

The reaction of $In(NO_3)_3 \cdot x\,H_2O$ with $K(H_2mF\text{-BTC})$ in DMF at 100 °C for 48 h yielded colourless crystals of UoC-13(1F). A picture of them taken under a light microscope is shown in the following Figure 4.27.

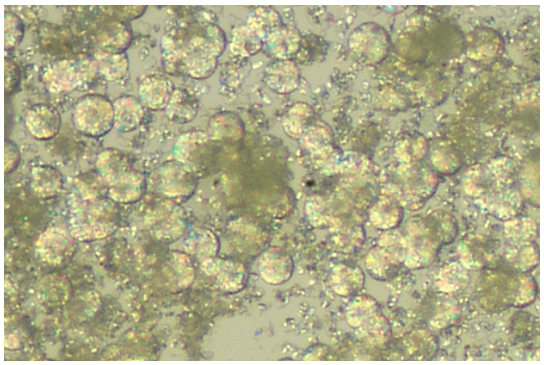

Figure 4.27: Light microscope image of UoC-13(1F) crystals.

A single crystal of UoC-13(1F) was analysed via X-ray diffraction. Selected crystallographic data are summarised in the following Table 4.4. Additional crystal data are provided in the attached CIF file.
Based on a single crystal X-ray diffraction (SCXRD) analysis, UoC-13(1F) crystallises in the tetragonal space group $I\bar{4}$ (no. 82) with four formula units per unit cell. The cell parameters are $a = 22.6077(5)$ Å and $c = 17.2858(6)$ Å with a cell volume of $8834.9(5)$ Å^3.

The asymmetric unit of UoC-13(1F) as shown in Figure 4.28 consists of three crystallographically independent In^{3+} cations and two $mF\text{–}BTC^{3-}$ anions. The indium cation In1 occupies in the special *Wyckoff* position *2c* and In3 the *Wyckoff* position *2b*. All other atoms of the asymmetric unit are on the general *Wyckoff* position *8g*.

Table 4.4: Selected crystallographic data and details of X-ray single crystal structure analysis of UoC-13(1F).

			UoC-13(1F)
Formula			$C_{36}H_8F_4In_3O_{24}$
Crystal system			tetragonal
Space group (no.), Z			$I\bar{4}$ (82), 4
Lattice parameter	a / Å		22.6077(5)
	c / Å		17.2858(6)
Cell volume	V / Å^3		8834.9(5)
R Indices	R_{int}		0.066
	R_1	(before *SQUEEZE*)	0.0479 (0.1063)
	wR_2	(before *SQUEEZE*)	0.0595 (0.2763)
	GooF	(before *SQUEEZE*)	0.930 (1.078)

The fluorine substituents in both *mF*-BTC^{3-} anions are disordered over positions: F1A/F1B and F2A/F2B. The occupancy refinement suggests a preference for the F1B position, with an approximate ratio of 41:59. There is no significant preference observed between the F2A and F2B positions. The H9 and H14 positions each contain one hydrogen atom. Notably, these hydrogen atoms were positioned using the AFIX 43 command, which ensured ideal distances and angles.

In literature, it is described that the presence of fluorine substituents on aromatic carboxylate linkers can significantly enhance the interplanar torsion angles between the carboxylate groups and the phenyl ring.[55]
For UoC-13(1F), one interplanar torsion angle is increased to 39.7°. This angle is between the phenyl ring and the carboxylate group (O3-C2-O4), which is located between the two disordered fluorine substituents F1A and F1B at the phenyl ring (C1-C9). The other interplanar torsion angles are 3.6° for O1-C1-O2, 13.2° for O5-C3-O6, 1.7° for O7-C10-O8, 13.4° for O9-C11-O10, and 10.3° for O11-C12-O12.

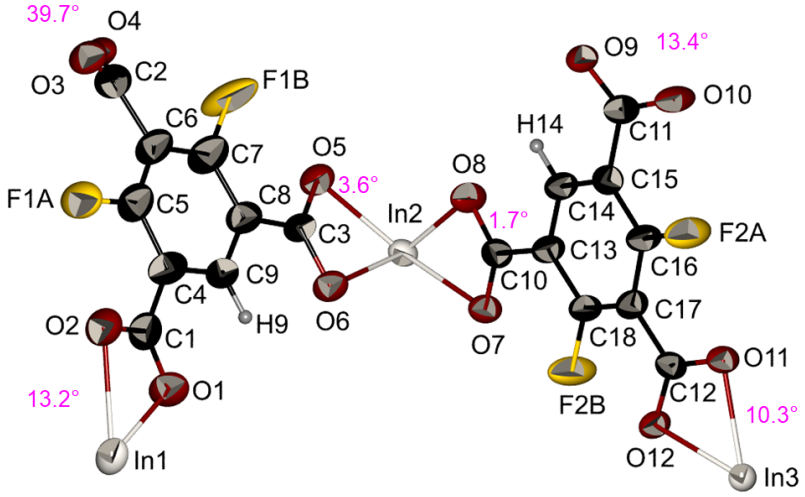

Figure 4.28: Ellipsoidal representation of the asymmetric unit. Thermal ellipsoids are drawn at the 50 % probability level. The angles between the carboxylic group and the phenyl ring are shown in pink. Colour code: In (white), O (dark red), C (black), F (yellow), and H (light grey).

The coordination environment of the indium cations (In1, In2, and In3) is illustrated in Figure 4.29. Each indium cation coordinates to eight oxygen atoms, forming a distorted triangular dodecahedron. Calculations using *SHAPE*[92] yielded $CShM_{TDD-8}$ values of 2.997 for In1, 2.846 for In2, and 2.519 for In3. The shortest In–O distance is between In1–O1 with 2.150(3) Å and the longest between In1–O2 with 2.480(3) Å.

The coordination of indium by four negatively charged carboxylate groups results in negatively charged SBUs, with $(CH_3)_2NH_2^+$ being the probable counter cations. As already discussed for UoC-7, they are formed by the hydrolysis of the solvent DMF[94] (see Chapter 4.2.1, p. 27 and following). Considering these three $(CH_3)_2NH_2^+$ cations, UoC-13(1F) is best described as ${}^3_\infty[((CH_3)_2NH_2)_3In_3(mF\text{–}BTC)_4]$.
In the refinement of UoC-13(1F), the cations could not be located. Since they are strongly disordered, this is not unusual. In the literature, the charge balancing cation has not been shown in the final refinement of many anionic MOFs.[22,72]
As a result, the residual electron density within the solvent-accessible voids of the compound was removed using the *SQUEEZE* routine[66] in *PLATON*.[93]

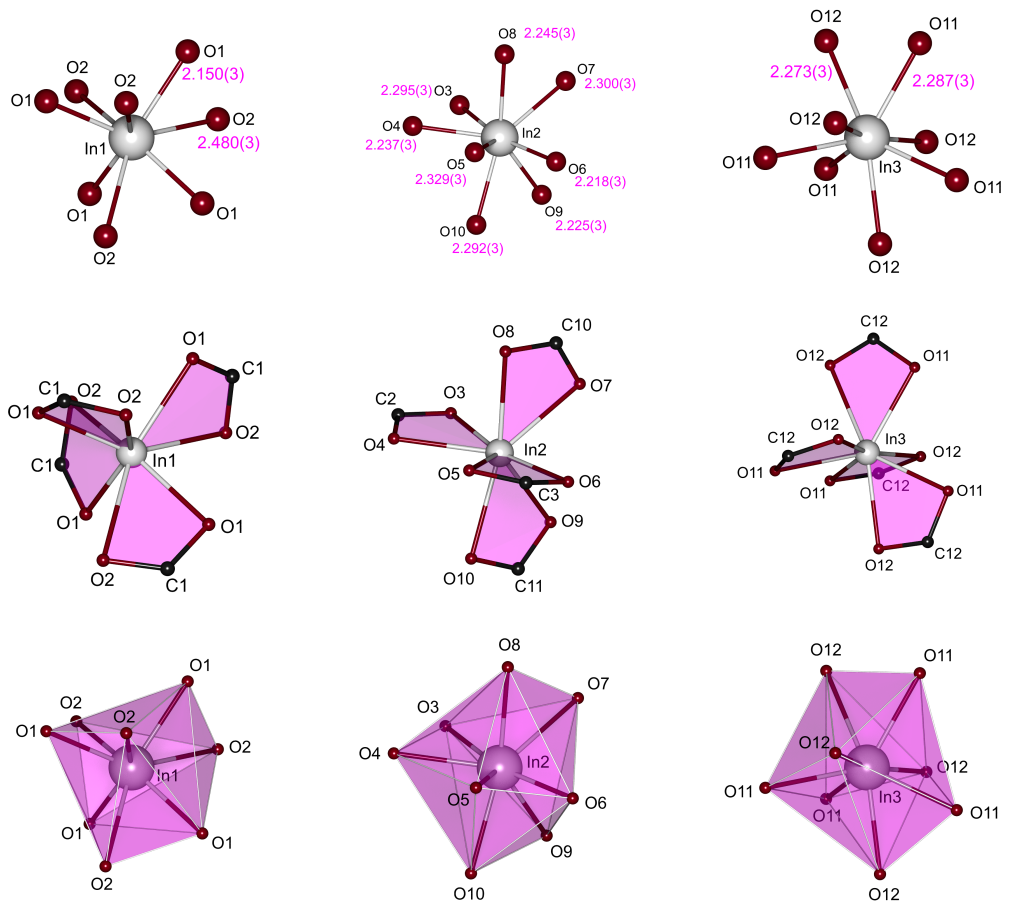

Figure 4.29: Coordination spheres around In1, In2 and In3 with labeling of the atoms (black) and In–O distances (Å, pink). The plane spanned by the coordination of the carboxylate groups to the indium cation is illustrated in pink.

To enable further analysis of UoC-13(1F), it was essential to synthesise a phase pure powder of UoC-13(1F). In contrast to the synthesis of the UoC-13(F) crystals, $In(NO_3)_2 \cdot xH_2O$ was replaced by $InCl_3$, the temperature was increased to 110 °C and the heating time was reduced from 48 h to 24 h. Furthermore, the cooling time was reduced from 72 h to 12 h. The aforementioned conditions yielded a colourless crystalline powder of UoC-13(1F). The PXRD pattern of this powder, as can be seen in Figure 4.30 on p. 52, shows some background noise, but indicates its phase purity.

Furthermore, the synthesis of UoC-13(1F) in DEF was successful, which is accompanied by the hydrolysis of DEF into larger $(C_2H_5)_2NH_2^+$ cations. The respective PXRD is shown in the appendix (see p. 141).

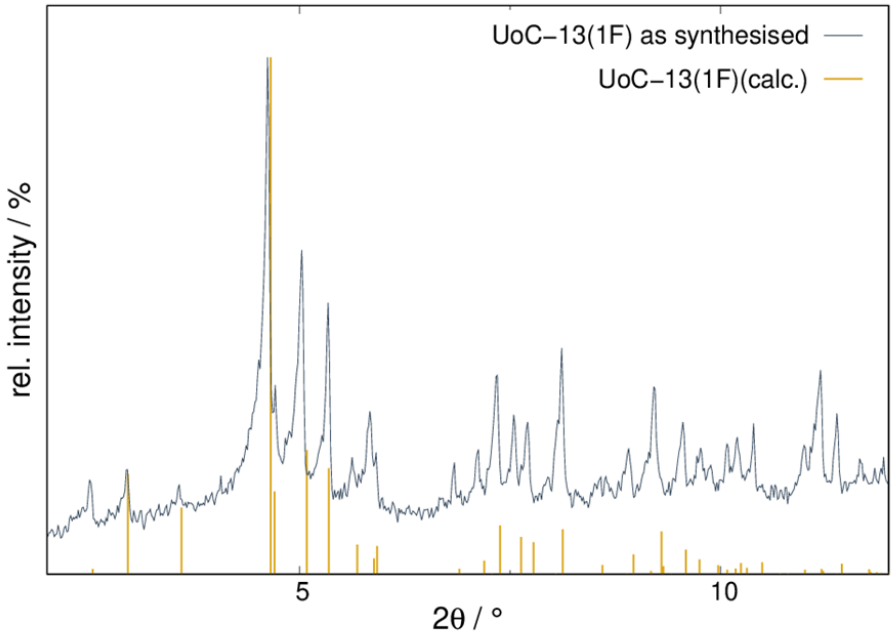

Figure 4.30: Left: PXRD pattern of UoC-13(1F) (blue). For comparison, the calculated reflection positions and intensities calculated from the crystal structure of UoC-13(1F) is given as a line diagram (orange). Right: powder of UoC-13(1F), as synthesised.

As previously mentioned, the contamination of seawater with $^{137}Cs^+$ cations following the Fukushima nuclear disaster has made MOFs capable of selectively adsorbing Cs^+ cations particularly valuable for potential use in seawater decontamination.
Owing to its anionic framework, UoC-13(1F) is a potential cation exchange material, however, similar to UoC-7, it was also found to be unstable in water as can be seen in the corresponding PXRD pattern in the appendix (see p. 142). Consequently, further investigations of UoC-13(1F) as Cs^+ exchange material were not pursued.

Furthermore, the thermal behaviour of UoC-13(1F) was investigated. The following Figure 4.31 shows the DSC/TGA curve of UoC-13(1F) synthesised in DMF.
A relative mass loss of 38 % up to approximately 450 °C can be observed in the TGA curve, accompanied by a weak endothermic signal in the DSC curve. This is likely attributed to the release of DMF molecules from the pores, which remain from the synthesis of UoC-13(1F). However, in this temperature range, the decomposition of the cations and the framework itself can be expected. It is possible, as already described for UoC-7, that the release of uncoordinated solvent molecules and the decomposition of both the cations and the framework happen simultaneously. Assuming that the mass loss up to approximately 450 °C is only due to the release of DMF molecules, a mass loss of 37 % is calculated for ten DMF molecules.

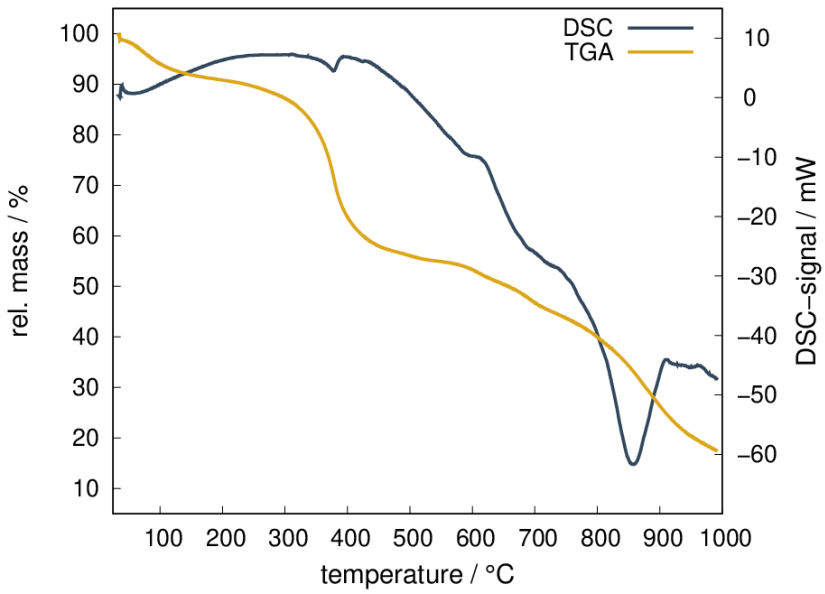

Figure 4.31: DSC/TGA measurement of UoC-13(1F), which was recorded while heating at a rate of 10 °C/min under a steady flow of argon gas, up to a maximum temperature of 1000 °C. The arrows are intended to indicate where the decomposition of the MOFs is estimated to occur.

Above 600 °C, a further mass loss of 37 % is observed, which is most probably due to the thermal decomposition of the remaining structure. This mass loss is accompanied

by a strong endothermic signal in the DSC curve. Starting at 650 °C, the formation of indium(III) oxide (In_2O_3) can be expected, Unfortunately, the quantity of the residue remaining after the analysis was insufficient for PXRD analysis.

The *SQUEEZE*[66] option in the *PLATON* software[93] calculated 1775 remaining electrons for the unit cell, which corresponds to 444 electrons per formula unit (Z = 4).
After accounting for the three $(CH_3)_2NH_2^+$ cations ($3 \cdot 26$ *electrons*) per formula unit, 366 electrons remain per formula unit. This number is approximately equivalent to nine DMF molecules, which is consistent with the results obtained from the TGA analysis.

Furthermore, *SQUEEZE*[66] of the *PLATON* software[93] yielded for UoC-13(1F) solvent-accessible voids of 5774 Å^3 per unit cell, which accounts for 65 % of the total unit cell volume. The potential voids can be seen in Figure 4.32. Their approximate diameter is 8 Å.

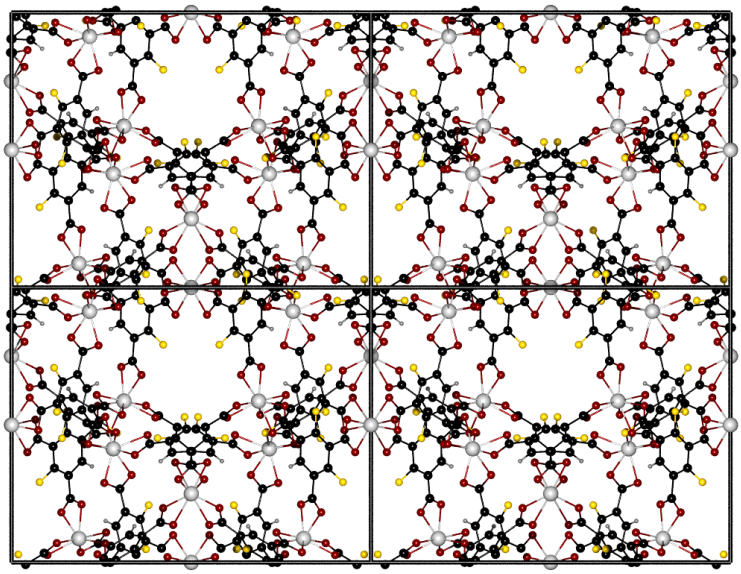

Figure 4.32: Part of the crystal structure of UoC-13(1F) in the direction [010]. Colour code: In (white), O (dark red), C (black), F (yellow), H (light gray).

The sorption behaviour of UoC-13(1F) was subsequently investigated by N_2 gas sorption measurements. For this, UoC-13(1F) was activated at 120 °C under high vacuum for 24 h. However, no type I isotherm has been observed to date. The resulting isotherm is presented in the appendix (see p. 148).

It is possible that 120 °C is insufficient to fully activate this MOF. To ascertain this, the sample should be activated at elevated temperatures before conducting further measurements.
Nevertheless, repeating the adsorption measurements is recommended, because it is reasonable that UoC-13(1F) is porous based on the aforementioned results.

4.2.3 $^{3}_{\infty}[((CH_3)_2NH_2)_3Ga_3(mF\text{-}BTC)_4]$ (GaMOF-1(1F))

Some of the results in the following chapter are described in the bachelor's thesis of Pascal L. Jurzick.[98] He prepared and characterised GaMOF-1(NH_2)[98] as part of his bachelor's thesis under the supervision of Susanna Wenzel in the research group of Prof. Dr. Uwe Ruschewitz. Susanna Wenzel contributed the synthesis and characterisation of the monofluorinated congener GaMOF-1(1F).

GaMOF-1,[22] published by *Banerjee et al.*, was already mentioned in Chapter 3.4 (see p. 11 and following). It was synthesised by reacting gallium nitrate hydrate with H_3BTC in a mixture of DMF and ethanol, in the presence of ammonium fluoride. The reaction mixture was heated to 180 °C for a period of five days.
Nevertheless, an analogous synthesis, in which gallium nitrate hydrate was reacted with K(H_2mF-BTC) or H_3mA-BTC, did not yield any product. As a result, the synthesis procedure was modified.
To synthesise the isostructural GaMOF-1(NH_2),[98] gallium nitrate hydrate and H_3mA-BTC were dissolved in DMA and heated at a lower temperature of 130 °C for just 72 h.
For the synthesis of GaMOF-1(1F), gallium chloride or gallium nitrate hydrate and K(H_2mF-BTC were dissolved in DMF and heated at 100 °C for 48 h, yielding colourless crystals of GaMOF-1(1F) (see Figure 4.33).

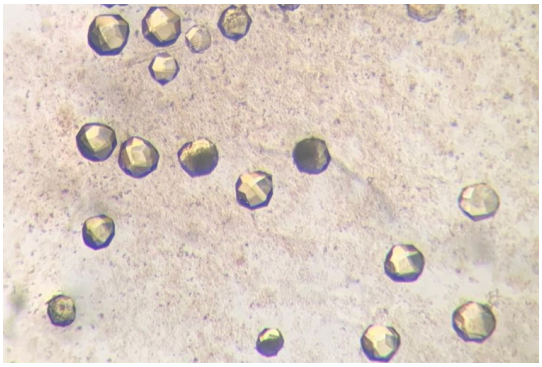

Figure 4.33: Photo of the crystals of GaMOF-1(1F) that was taken under a light microscope.

A crystal of GaMOF-1(1F) was analysed via single crystal X-ray diffraction. It crystallises isostructurally to GaMOF-1[22] and GaMOF-1(NH_2)[98] in the cubic space group $I\bar{4}3d$ (no. 220), with four formula units per unit cell. The cell parameter is a = 19.9908(5) Å with a unit cell volume of 7989.0(6) Å^3. The following table 4.5 presents selected crystallographic data from the single crystal analysis of Ga-MOF-1(1F), GaMOF-1[22] and GaMOF-1(NH_2).[98] The comparison of the parameters shows that the lattice parameters and the overall volumes of the unit cells are similar for all three MOFs.

Table 4.5: Selected parameters of the crystal structure analysis of the unfluorinated GaMOF-1,[22] GaMOF-1(1F) and GaMOF-1(NH_2).[98]

	GaMOF-1[22]	GaMOF-1(1F)	GaMOF-1(NH_2)[98]
Formula	$C_{36}H_{12}Ga_3O_{24}$	$C_{36}H_8F_4Ga_3O_{24}$	$C_{36}H_{16}N_4Ga_3O_{24}$
Crystal system	cubic	cubic	cubic
Space group (no.), Z	$I\bar{4}3d$ (220), 4	$I\bar{4}3d$ (220), 4	$I\bar{4}3d$ (220), 4
Lattice parameter a / Å	19.9611(9)	19.9908(5)	20.007(3)
V / Å^3	7953.4(6)	7989.0(6)	8008.9(4)
R_{int}	0.0473	0.0543	0.104
R_1 (before *SQUEEZE*)	0.0305 (0.0903)	0.0364 (0.0903)	0.1019 (0.0653)
wR_2 (before *SQUEEZE*)	0.0909 (0.2500)	0.1022 (0.2500)	0.2788 (0.1841)
GooF (before *SQUEEZE*)	1.07	1.092 (1.135)	1.123 (1.158)

In all three crystal structures, the asymmetric unit consists of one crystallographically independent gallium metal cation (Ga1) and one-third of the linker. The asymmetric unit of GaMOF-1(1F) is shown in Figure 4.34.
The atoms C1, C2, C3, O1, O2 and O3 occupy the general *Wyckoff* position *48e*, while the gallium cation Ga1 occupies the special *Wyckoff* position *12a*.
GaMOF-1(1F) has just one fluorine substituent (F1), therefore, its occupancy was set to 1/3, as it was for N1, H1A und H1B in GaMOF-1(NH_2).[98]

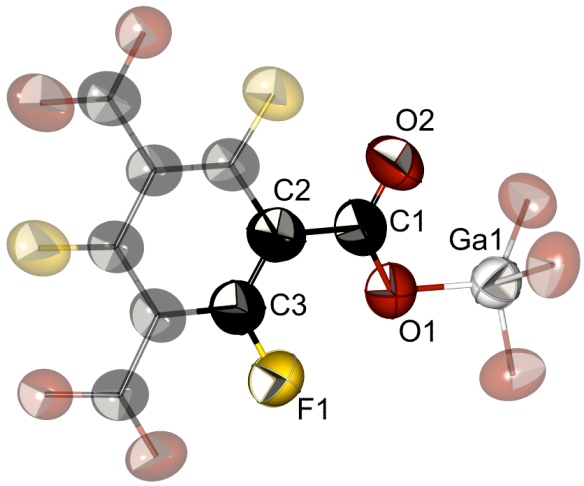

Figure 4.34: Thermal ellipsoids are drawn at the 50 % probability level. The atoms of the asymmetric unit are labelled. Atoms that complete the linker and the coordination sphere of Ga1 are depicted in a transparent mode. Colour code: Ga (white), O (dark red), C (black), F (yellow).

In literature, it is described that the presence of fluorine substituents on aromatic carboxylate linkers can significantly enhance the interplanar torsion angles between the carboxylate groups and the phenyl ring.[55]
In GaMOF-1(1F), the interplanar torsion angle between the phenyl ring (C1-C9) and the carboxylate group (O1-C1-O2) is 8.7°. In contrast, this angle is 4.4° in GaMOF-1 and 7.3° in GaMOF-1(NH_2). Therefore, the fluorine- and amino-substituted GaMOF-1 show only slight increased interplanar torsion angles compared to the unsubstituted MOF. Therefore, the BTC^{3-} linkers remain nearly planar in all three structures.

However, an increasing number of fluorine substituents leads to stronger repulsive interactions, resulting in higher interplanar torsion angles.[55] Since the structure of the linker has a significant influence on the crystal structure of the resulting MOF, it is possible that the increased interplanar torsion angle of the *dF*-BTC^{3-} and *pF*-BTC^{3-} linker makes the formation of a di- or perfluorinated GaMOF-1 unlikely. Accordingly, all attempts to synthesise them failed.

Each gallium cation is coordinated by four oxygen atoms in a tetrahedral geometry (see Figure 4.35). Calculations using *SHAPE*[92] yielded $CShM_{T-4}$ values of 0.937 for Ga1.

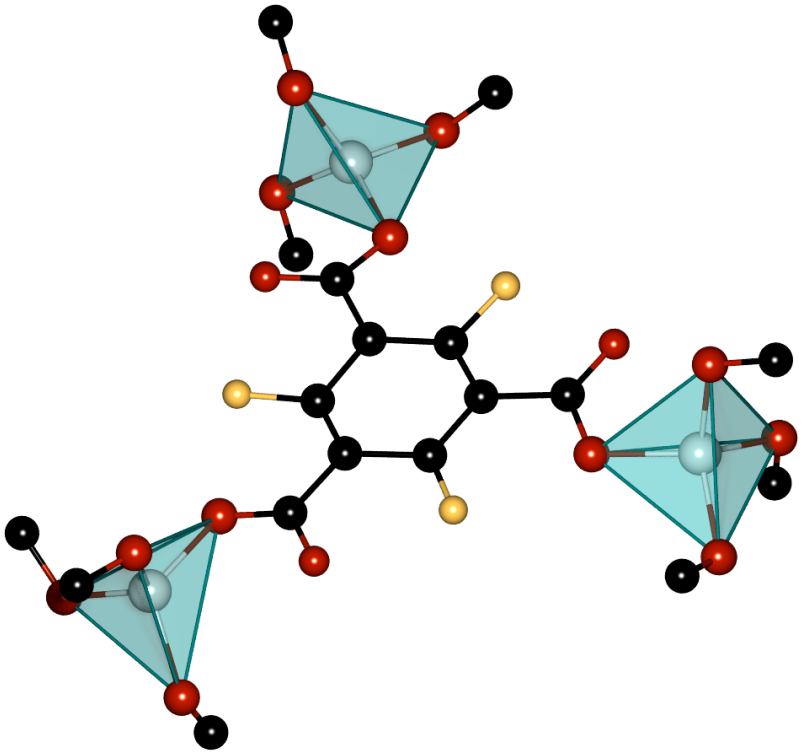

Figure 4.35: A section of the crystal structure of GaMOF-1(1F) showing the coordination sphere of the gallium cations and the *mF*-BTC^{3-} linker. Colour code: Ga (white), O (dark red), C (black), F (yellow).

The bond lengths of Ga1-O1 in all three MOFs are summarised in Table 4.6, showing a significant difference. GaMOF-1(1F) has the largest bond length at 184.5(3) pm (Ga1-O1), while GaMOF-1(NH_2) has the shortes at 181.4(6) pm (Ga1-O1). The bond length of 183.17(2) pm in GaMOF-1 is 183.17(2) pm (Ga1-O1), falling in between.
Each linker coordinates to three gallium cations via its carboxylate groups, with each carboxylate group binding to the gallium cations monodentately via O1.
For GaMOF-1(1F), the distances between the carbon (C1) of the carboxylate group and the two respective oxygen atoms, O1 and O2, are 126.8(7) pm and 122.0(8) pm, confirming that O2 remains uncoordinated. These bond lengths also differ significantly from them found in GaMOF-1 and GaMOF-1(NH_2) (see Table 4.6). In GaMOF-1, the bond lengths are 131.0(2) pm (C1-O1) and 120.1(3) pm (C1-O2), and in GaMOF-1(NH_2), they are 130.4(9) pm (C1-O1) and 122.0(1) pm (C1-O2).

Table 4.6: Comparison of selected bond lengths d and interplanar torsion angle $\measuredangle_{Tors.}$ between the carboxylate groups and the phenyl ring (Ph = C2, C3) within the unfluorinated GaMOF-1,[22] GaMOF-1(1F) and GaMOF-1(NH_2).[98]

	GaMOF-1[22]	GaMOF-1(1F)	GaMOF-1(NH_2)[98]
d(Ga1–O1) / pm	183.17(2)	184.5(3)	181.4(6)
d(C1–C2) / pm	149.6(2)	147.2(6)	148.4(9)
d(C1–O1) / pm	131.0(2)	126.8(7)	130.4(9)
d(C1–O2) / pm	120.1(3)	122.0 (8)	122.0(1)

	GaMOF-1[22]	GaMOF-1(1F)	GaMOF-1(NH_2)[98]
$\measuredangle_{Tors.}$(Ph:O1–C1–O2) / °	4.4	8.7	7.3

Similar to UoC-13(1F), the coordination of each gallium cation to four negatively charged carboxylate groups results in the formation of negatively charged SBUs (see Chapter 4.2.2, p. 48). In the synthesis of GaMOF-1(1F), DMF is used as a solvent. Therefore, the most probable counter cation is $(CH_3)_2NH_2^+$, which is formed by the hydrolysis of DMF.[94] Considering the $(CH_3)_2NH_2^+$ cations, GaMOF-1(1F) can be described as $^3_\infty[((CH_3)_2NH_2)_3Ga_3(mF\text{–}BTC)_4]$.

Similar to UoC-13(1F), GaMOF-1,[22] and GaMOF-1(NH_2),[98] the $(CH_3)_2NH_2^+$ counter cations in GaMOF-1(1F) are strongly disordered and could not be located in its refinement. Consequently, the residual electron density within the solvent-accessible voids of the compound was removed using the *SQUEEZE*[66] routine in *PLATON*.[93]
For GaMOF-1(1F), *SQUEEZE*[66] calculated a solvent-accessible volume of 4827 Å^3 per unit cell, which is approximately 60 % of the total unit cell volume.
Moreover, *SQUEEZE*[66] determined that there are 1383 remaining electrons in the unit cell. With Z = 4, this corresponds to 346 electrons per formula unit. After accounting for the three $(CH_3)_2NH_2^+$ cations per formula unit (3 × 26 electrons), 268 electrons remain, which corresponds to approximately six to seven non-coordinating DMF molecules per formula unit.
Additional information on the amount of non-coordinating solvent molecules could be provided by DSC/TGA measurements, as described for GaMOF-1.[22] However, despite the sample being phase-pure (as shown in the Figure 4.36, p. 61), the yield has been limited to a few single crystals, which precludes further characterization.
The N_2 adsorption isotherm of GaMOF-1 measured at 77 K is a type I isotherm with a resulting BET surface area of 205 m^2/g (Langmuir surface area: 236 m^2/g).[22] This is relatively low compared to many highly porous MOFs.[41]
In contrast, no type I isotherm was obtained for GaMOF-1(NH_2) (see Figure 7.30 in the appendix, p. 148). For GaMOF-1(1F), a comparable result was expected. However, activation was not attempted due to the limited yield of this MOF.

The size of the cation is a significant factor in the synthesis of GaMOF-1.[22] Using tetrapropylammonium iodide instead of dimethylammonium chloride results in the formation of CAUMOF-11,[73] which crystallises in the trigonal space group $R3c$ (no. 161).[22] This structural change, driven by the varying sizes of cations or solvent molecules, is known as the template effect.[74]
In contrast, the use of tetrapropylammonium iodide in the synthesis of GaMOF-1(1F) resulted in the absence of any precipitation, whereas in the synthesis of GaMOF-1(NH_2), an isostructural product was formed.[98]

Moreover, attempts were made to synthesise GaMOF-1(1F) in DEF and DBF, which hydrolyse to form $(C_2H_5)_2NH_2^+$ and $(C_4H_9)_2NH_2^+$ cations. The resulting powders were analysed by PXRD (see Figure 4.36). The PXRD analysis did not show any correlation between their patterns and the calculated pattern of the GaMOF-1(1F) crystal structure. In the course of this work, it was not possible to identify and characterise them further.

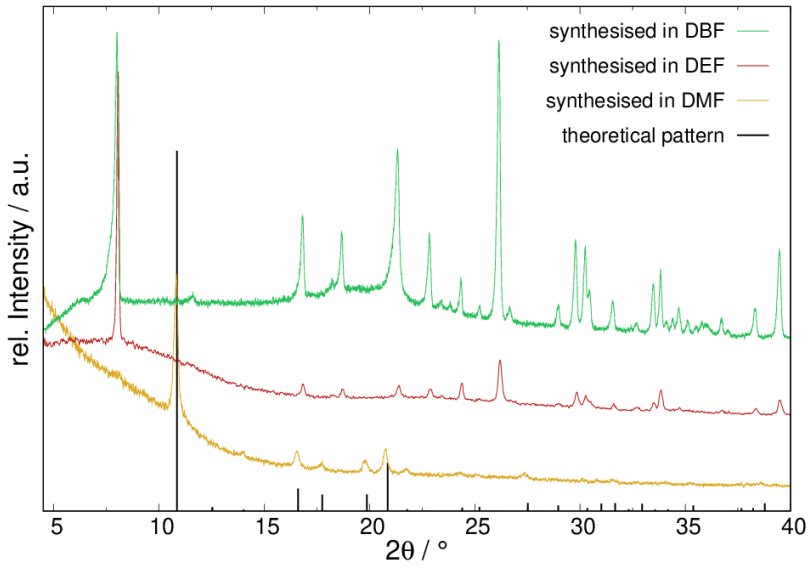

Figure 4.36: The PXRD pattern of GaMOF-1(1F) (*Rigaku Miniflex600-C*, Cu Kα radiation (λ = 1.5418 Å)) is compared to the PXRD patterns of the products synthesised in DEF and DBF. For comparison, the reflection positions and intensities calculated from the crystal structure solution of GaMOF-1(1F) as a line diagram.

4.3 $[[Zn_4O]_4[M_2(H_2O)_2]_3(mF/dF{-}BTC)_{12}]$ (M = Zn, Cu, Co) (UoC-5)

Some of the results presented in the following chapter were previously reported in the master's thesis of Susanna Wenzel[4] and the bachelor's thesis of Aimée E. L. Cammiade.[3] Aimée E. L. Cammiade synthesised and characterised Zn-UoC-5(1F) as part of her bachelor's thesis under the supervision of Prof. Dr. Uwe Ruschewitz.[3] Cu,Zn-UoC-5(1F) and Cu,Zn-UoC-5(2F) were first synthesised as crystalline powders in the preceding master's thesis by Susanna Wenzel.[4]
Building on these results, Susanna Wenzel synthesised single crystals of Cu,Zn-UoC-5(1F) and Co,Zn-UoC-5(1F) within this thesis, and characterised their structure and thermal behaviour. Additionally, Susanna Wenzel reproduced Cu,Zn-UoC-5(1F) and Cu,Zn-UoC-5(2F) as well as synthesised Co,Zn-UoC-5(1F) and Co,Zn-UoC-5(2F) as crystalline powders, and characterised their thermal and sorption behaviour for the first time.

The reaction of $Zn(NO_3)_2 \cdot 6\,H_2O$ with $K(H_2mF{-}BTC)$ in DMA yielded colourless crystals of Zn-UoC-5(1F), as depicted in Figure 4.37[4] (left). A structural model of this MOF was first introduced in a previous bachelor's thesis.[3]
During this doctoral thesis, crystals of the isostructural bimetallic compounds Cu,Zn-UoC-5(1F) and Co,Zn-UoC-5(1F) were successfully synthesised. For this, $Zn(NO_3)_2 \cdot 6\,H_2O$ and $K(H_2mF{-}BTC)$ was reacted with $Cu(NO_3)_2 \cdot 3\,H_2O$ and $Co(NO_3)_2 \cdot 6\,H_2O$, respectively. These crystals are also shown in Figure 4.37.

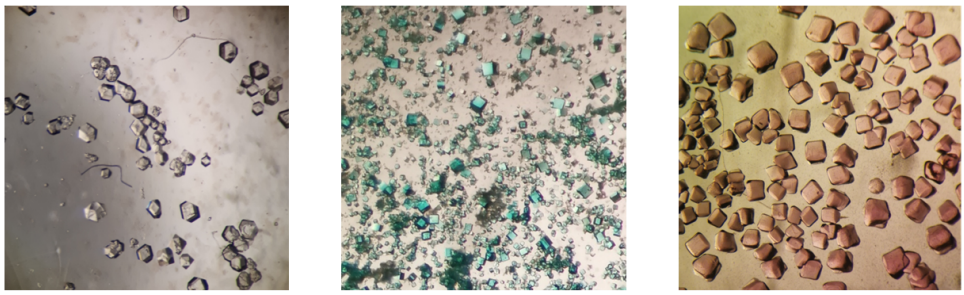

Figure 4.37: Light microscopy pictures of the crystals of Zn-UoC-5(1F),[4] Cu,Zn-UoC-5(1F) and Co,Zn-UoC-5(1F) (from left to right).

Structural Refinement and Analysis of Zn-UoC-5(1F), Cu,Zn-UoC-5(1F) and Co,Zn-UoC-5(1F)

All three compounds were analysed by single crystal X-ray diffraction as part of this work.
However, the structural solution of Zn-UoC-5(1F)[3] was not improved by either better crystal quality or enhanced data quality (as indicated by similar R_{int} values).
Nevertheless, the structures of Cu,Zn-UoC-5(1F) and Co,Zn-UoC-5(1F) were characterised for the first time in this work and will be described and compared to the existing structural model of Zn-UoC-5(1F)[3] in this section.
For comparison, selected parameters of the single crystal X-ray diffraction analysis are presented in Table 4.7. Additional details on the structure solutions and refinements can be found in the corresponding CIF files, which are attached to this thesis.

Table 4.7: Selected crystallographic data and details of single crystal structure analysis of Zn-UoC-5(1F),[3] Cu,Zn-UoC-5(1F) and Co,Zn-UoC-5(1F).

	Zn-UoC-5(1F)[3]	Cu,Zn-UoC-5(1F)	Co,Zn-UoC-5(1F)
Formula	$C_{54}H_{18}F_6O_{41}Zn_{11}$	$C_{54}H_{18}F_6O_{41}Cu_3Zn_8$	$C_{54}H_{18}F_6O_{41}Co_3Zn_8$
Crystal system	cubic	cubic	cubic
Space group (no.), Z	$I23$ (197), 4	$I23$ (197), 4	$I23$ (197), 4
a / Å	23.1070(7)	23.1094(10)	23.1084(10)
V / Å^3	12337.6(11)	12357.4(7)	12339.8(17)
R_{int}	0.1516	0.1587	0.0477
R_1 (before *SQUEEZE*)	0.1783	0.1342 (0.1988)	0.1609 (0.2837)
wR_2 (before *SQUEEZE*)	0.3697	0.3201 (0.4591)	0.4008 (0.6439)
GooF (before *SQUEEZE*)	1.042	1.273 (1.897)	1.852 (3.339)
Flack(x)	0.55(14)	0.49(11)	0.505(5)

Zn-UoC-5(1F),[3] Cu,Zn-UoC-5(1F) and Co,Zn-UoC-5(1F) crystallise in the cubic space group $I23$ (no. 197) with four formula units per unit cell.
The cell volume of Zn-UoC-5(1F) is 12 337.6(11) Å with the cell parameter a = 23.1070(7) Å.[3] In comparison, the cell parameter for Co,Zn-UoC-5(1F) shows a slight increase to a = 23.1084(10) Å with a corresponding cell volume of V = 12334.8(17) Å^3. Similarly, for Cu,Zn-UoC-5(1F), the cell parameter increases to a = 23.1084(10) Å with a cell volume of V = 12334.8(17) Å^3. However, the partial substitution of zinc cations with cobalt or copper cations neither affects the formation of the structure nor significantly alters the unit cell size.

Like Zn-UoC-5(1F),[3] the crystal structure of Cu,Zn-UoC-5(1F) was solved as an inversion twin. The asymmetric unit of Cu,Zn-UoC-5(1F) is shown in Figure 4.38, where the ellipsoids are depicted with a 50 % probability level. Additionally, atoms are shown in a semi-transparent mode to visualise the coordination sphere of the metal cations.

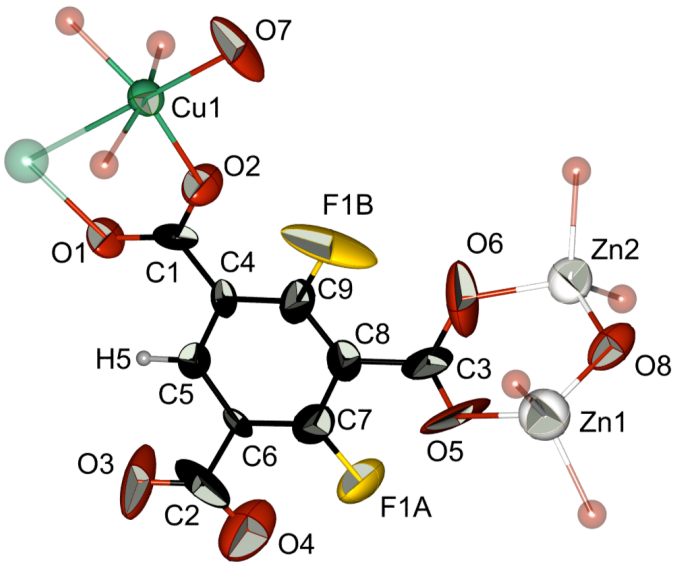

Figure 4.38: Asymmetric unit of Cu,Zn-UoC-5(1F): the thermal ellipsoids are drawn at the 50 % probability level, with all atoms labelled. Atoms that complete the coordination sphere of the metal cations are depicted in a transparent mode. Colour code: Zn (white), Cu (green), O (dark red), C (black), F (yellow), and H (light grey).

The asymmetric unit consists of two crystallographically independent zinc cations (Zn1 and Zn2), one copper cation (Cu1), one *mF*-BTC^{3-} anion, and two further oxygen atoms (O7 and O8). It is probable that O7 belongs to a DMA or to a H_2O molecule, which is coordinated to the copper cation Cu1. However, the solvent molecule could not be refined.
The fluorine substituent of the linker is disordered over the two F1A and F1B positions. The occupancies of these positions were refined freely, revealing a preference for position F1A with a ratio of approximately 66:34.
The refinement of F1A, F1B, C3, O3, O4, O5, and O7 via split positions, as recommended by *SHELXL*,[99] did not result in a chemically meaningful structural model and was discarded.
Zn1 and O8 occupy the special *Wyckoff* position *8c*, while Cu1 and O7 occupy the special *Wyckoff* position *12e*. All other atoms occupy the general *Wyckoff* position *24f*.
This results in $C_{54}H_{18}F_6O_{41}Cu_3Zn_8$ as the sum formula for Cu,Zn-UoC-5(1F).

Refining Co,Zn-UoC-5(1F) proved to be more challenging than refining Zn-UoC-5(1F)[3] and Cu,Zn-UoC-5(1F). The Co,Zn-UoC-5(1F) measurement shows the lowest R_{int} value among the three datasets. However, the data did not provide a chemically meaningful starting model, and stable refinement was only achieved by constraining bond lengths and angles to chemically reasonable values. After using the *SQUEEZE*[66] routine of PLATON[93] to remove residual electron density, the structure could be refined anisotropically.
The asymmetric unit of Co,Zn-UoC-5(1F) is shown in Figure 4.39 (see p. 66), with ellipsoids represented at a 50 % probability level. Additionally, the atoms are rendered in a semi-transparent mode to clearly visualise the coordination sphere of the zinc and cobalt cations.
Similar to Zn-UoC-5(1F)[3] and Cu,Zn-UoC-5(1F), it consists of three crystallographically independent metal cations (Zn1, Zn2, Co1), one *mF*–BTC^{3-} anion (C1-C9, O1-O6, F1, H1) and two coordinating oxygen atoms (O7, O8).
In Cu,Zn-UoC-5(1F), the copper atom (Cu1) is located in the special Wyckoff position 12e. However, in Co,Zn-UoC-5(1F), it is cobalt (Co1) that occupies this position. All other atoms are positioned as outlined for Zn-UoC-5(1F)[3] and Cu,Zn-UoC-5(1F).
This results in $C_{54}H_{18}F_6O_{41}Co_3Zn_8$ as the sum formula for Co,Zn-UoC-5(1F).

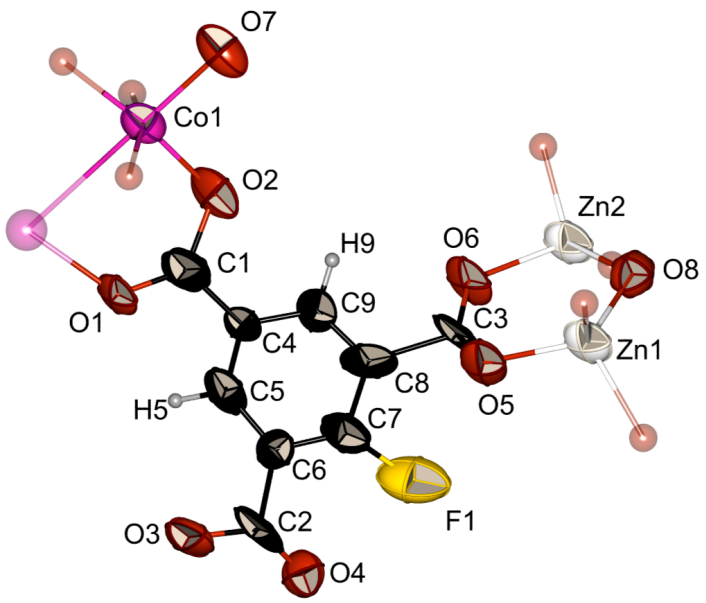

Figure 4.39: Asymmetric unit of Co,Zn-UoC-5(1F): the thermal ellipsoids are drawn at the 50 % probability level, with all atoms labelled. Atoms that complete the coordination sphere of the metal cations are depicted in a transparent mode. Colour code: Zn (white), Co (pink), O (dark red), C (black), F (yellow), and H (light grey).

For all three MOFs, the R indices indicate that the refinements are of insufficient quality (see Table 4.7, p. 63). Ideally, the R_1 value should be less than 5 %, and at the very least below 10 %.[100]

However, R_1 values of 17.83 % for Zn-UoC-5(1F) and 14.79 % for Co,Zn-UoC-5(1F) are significantly higher. Only the R_1 value for Cu,Zn-UoC-5(1F), at 11.41 %, is close to 10 %.

Additionally, the wR_2 value is often approximately two to three times greater than the R_1 value, which is the case for all three structures.

Nevertheless, it should be as small as possible, ideally less than 15 %,[100] which none of the refinements offer.

Given the very large unit cell volume, the structural model is still considered acceptable. Moreover, the thermal ellipsoids of Zn-UoC-5(1F) and Cu,Zn-UoC-5(1F) are enlarged.

While the thermal ellipsoids of Co,Zn-UoC-5(1F) appear reasonably well-defined, the refinement process used was somewhat unconventional. Only F1 shows an enlarged ellipsoid, which indicates a disorder for F1, possibly as for Zn-UoC-5(1F) and Cu,Zn-UoC-5(1F), over two positions. Nevertheless, such a splitting did not lead to a stable refinement of Co,Zn-UoC-5(1F).
Generally, a possible reason for the enlarged ellipsoids could be data of insufficient quality. Nonetheless, upon examining the bond lengths, angles, and coordination spheres, all structural models remain chemically plausible.

In literature, it is described that the presence of fluorine substituents on aromatic carboxylate linkers can significantly enhance the interplanar torsion angles between the carboxylate groups and the phenyl ring.[55] For all three MOFs, these angles are summarised in the following Table 4.8.
In Zn-UoC-5(1F) and Cu,Zn-UoC-5(1F), particularly the interplanar torsion angle between the phenyl ring and the carboxylate group, which is located between the two disordered fluorine substituents, is increased to 39.7°. Similarly, in Co,Zn-UoC-5(1F), this angle was the largest, even though fluorine is not disordered in this structure.

Table 4.8: Comparison of the interplanar torsion angle $\measuredangle_{Tors.}$ between the carboxylate groups and the phenyl ring (C4-C9) within Zn-UoC-5(1F),[3] Cu,Zn-UoC-5(1F) and Co,Zn-UoC-5(1F).

	Zn-UoC-5(1F)[3]	Cu,Zn-UoC-5(1F)	Co,Zn-UoC-5(1F)
$\measuredangle_{Tors.}$(C4-C9:O1–C1–O2) / °	13.2	4.7	3.4
$\measuredangle_{Tors.}$(C4-C9:O3–C2–O4) / °	16.3	13.7	23.5
$\measuredangle_{Tors.}$(C4-C9:O5–C1–O6) / °	44.0	51.2	58.1

One particularly noteworthy aspect of the UoC-5 structure is the presence of two different SBUs, as illustrated in Figure 4.40 (see p.68). One SBU is a M_2 paddlewheel unit, which is spanned by two equivalent metal cations (M = Zn, Cu, Co) and the second SBU an octahedral $Zn_4O(COO)_6$ cluster.
The M_2 paddlewheel is a well-known structural feature from the HKUST-1[13] framework. Each metal cation is coordinated to another metal cation, four oxygen atoms from four

different linkers, and one oxygen atom from a solvent molecule, such as water or DMA. Although the oxygen atom (O7) of these solvent molecules was refined, it was not possible to refine the entire solvent molecules for any of the three MOFs.
The second SBU is an octahedral $Zn_4O(COO)_6$ cluster consisting of four zinc cations coordinated to a central oxygen atom (O8) in a tetrahedral arrangement, with each zinc cation further connected to three carboxylate groups from six different organic linkers. This SBU is well known from MOF-5[12].

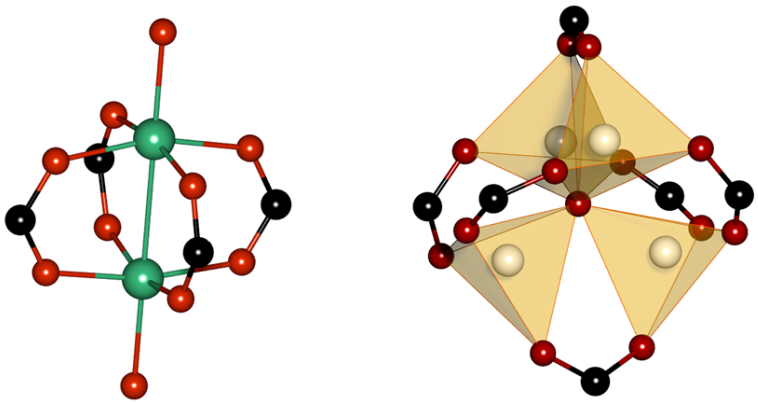

Figure 4.40: SBUs present in the UoC-5 structure: M_2 paddlewheel unit (left) and $Zn_4O(COO)_6$ unit (right).Colour code: Zn (white), Cu (green), O (dark red), C (black), F (yellow), and H (light grey).

In all three MOFs, the two metal cations in the paddlewheel unit are each surrounded by five oxygen atoms and one additional metal cation, forming a slightly distorted octahedron. Each zinc cation (Zn1 and Zn2) coordinates to four oxygen atoms, forming a nearly ideal tetrahedron. All Continuous Shape Measures (CShM) values calculated using *SHAPE*[92] are summarised in Table 4.9.

Table 4.9: CShM values calculated by *SHAPE*[92] for Zn-UoC-5(1F),[3] Cu,Zn-UoC-5(1F) and Co,Zn-UoC-5(1F).

	Zn-UoC-5(1F)[3]	Cu,Zn-UoC-5(1F)	Co,Zn-UoC-5(1F)
$CShM_{T-4}$ (Zn1)	0.518	0.107	0.062
$CShM_{T-4}$ (Zn2)	1.934	0.282	1.173
$CShM_{OC-6}$ (Zn3/Cu1/Co1)	1.770	1.473	2.252

In Cu,Zn-UoC-5(1F), the distance between metal cations in the paddlewheel unit is measured as 276.0(3) pm. This distance is consistent with those observed in other MOFs featuring Cu_2 paddlewheel units.[52] This consistency suggests that the paddlewheel unit in Cu,Zn-UoC-5(1F) is likely occupied by copper cations.
In contrast, for Co,Zn-UoC-5(1F), the Co1–Co1 distance within the paddlewheel unit is 295.7(6) pm, which corresponds well with distances observed in other MOFs featuring Co_2 paddlewheel units.[101] However, the distance is notably similar to the Zn3–Zn3 distance observed in Zn-UoC-5(1F) making it less clear which metal cation occupies the paddlewheel position in Co,Zn-UoC-5(1F).
Determining which metal cation occupies which position can be challenging, as Cu^{2+} and Co^{2+} have nearly the same number of electrons, making them difficult to distinguish during refinement.

To gain further insights into the chemical composition of Cu,Zn-UoC-5(1F), particularly the ratio of the two metals, X-ray photoelectron spectroscopy (XPS) was employed. The survey spectra for this MOF reveal the expected peaks for carbon, oxygen, fluorine, copper, and zinc, as illustrated in Figure 4.41.
The XPS analysis yielded a zinc-to-copper ratio of approximately 3:1. This result deviates from the 8:3 ratio determined by SCXRD analysis. This discrepancy may result from the uneven distribution of metals within the sample. Additionally, XPS is a surface-sensitive method, which can affect the accuracy of the measured ratios.
Furthermore, the high-resolution XPS spectra of the Cu 2p signals confirm that copper is, as anticipated, in the +II valence state, evidenced by a binding energy of 954 eV (2p1/2) and 933.7 eV (2p3/2).

Similarly, the Zn 3s binding energy measured at 139.8 eV supports the conclusion that zinc is also in the +II valence state.

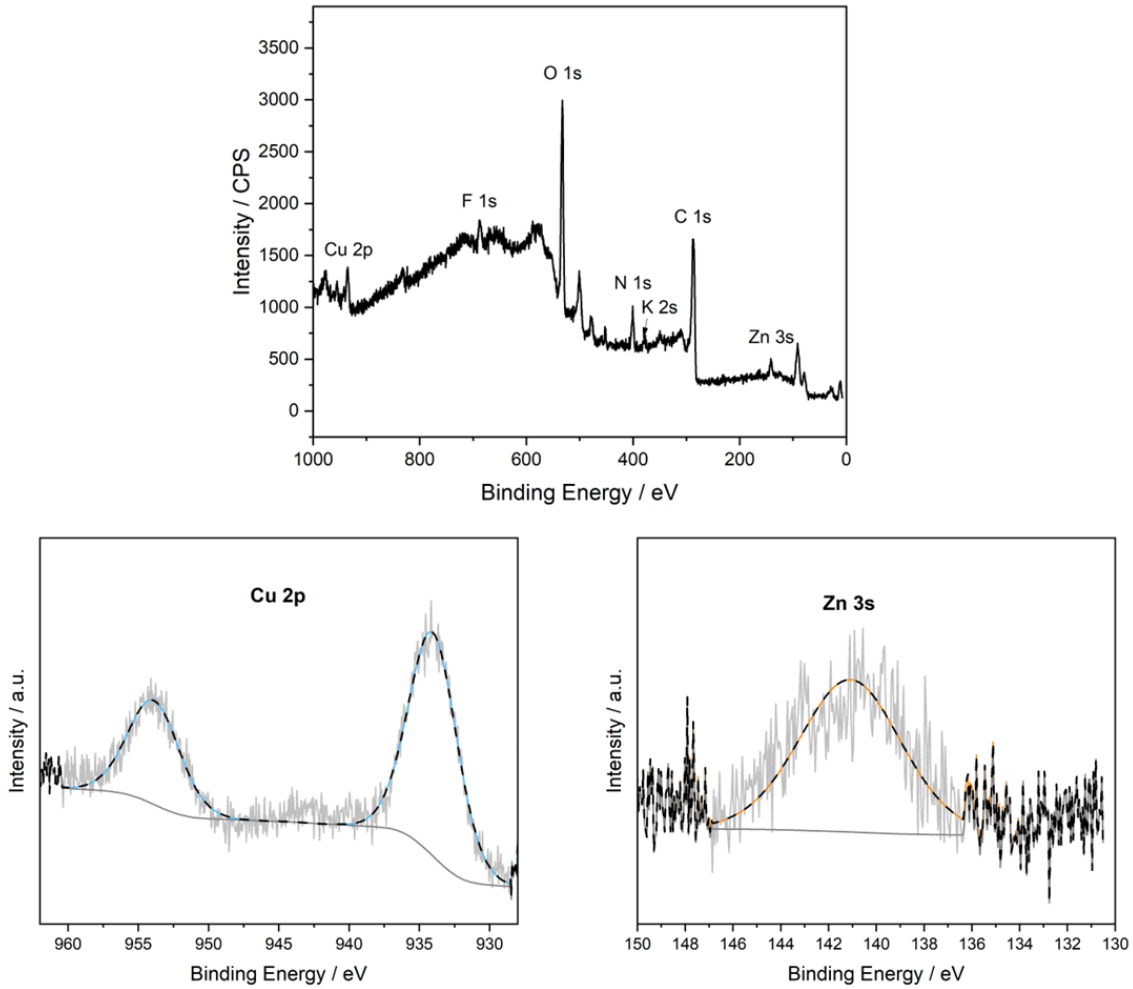

Figure 4.41: XPS analysis of Cu,Zn-UoC-5(1F).

The expansion of the structure, originating from the two SBUs, results in a three-dimensional network. Within the structure, highly convoluted channels are formed, into which the fluorine atoms protrude.
Triangular channels are observable along the [111] direction as depicted in the following Figure 4.42.

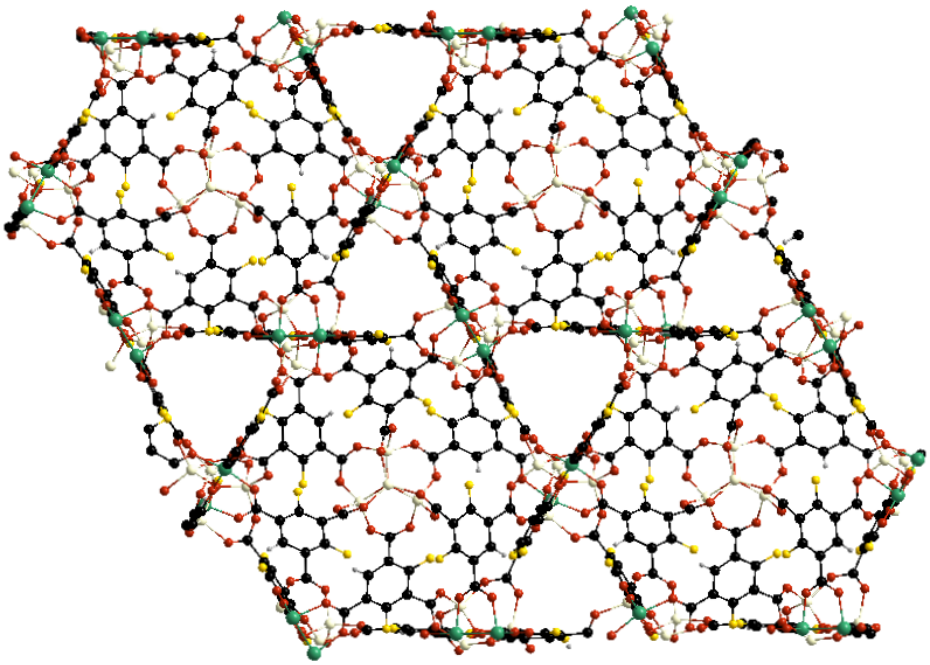

Figure 4.42: Part of the crystal structure of Cu,Zn-UoC-5(1F) in the direction of [111]. Colour code: Zn (white), Cu (green), O (dark red), C (black), F (yellow), and H (light grey).

4.3.1 Synthesis and Phase Purity of Zn-UoC-5(1F), Cu,Zn-UoC-5(1F), CuZn-UoC-5(2F), Co,Zn-UoC-5(1F) and Co,Zn-UoC-5(2F)

The reaction of K(H_2dF–BTC) with a mixture of $Zn(NO_3)_2 \cdot 6\,H_2O$ and $Cu(NO_3)_2 \cdot 6\,H_2O$ in DMA yielded green powders of a difluorinated UoC-5 (Cu,Zn-UoC-5(2F)), as already described in the previous master's thesis.[4]

In the course of this work, $Cu(NO_3)_2 \cdot 6\,H_2O$ was substituted with $Co(NO_3)_2 \cdot 6\,H_2O$ and reacted with K(H_2dF–BTC) in DMF. This resulted in Co,Zn-UoC-5(1F) and Co,Zn-UoC-5(2F) as reddish powders, which are shown in the following Figure 4.43.

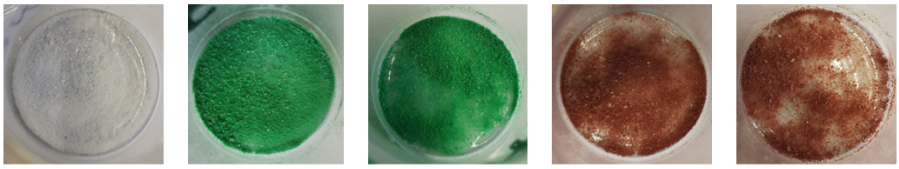

Figure 4.43: Powders of Zn-UoC-5(1F), Cu,Zn-UoC-5(1F), Cu,Zn-UoC-5(2F), Co,Zn-UoC-5(1F) and Co,Zn-UoC-5(2F) (from left to right).

The synthesis parameters for all five compounds are presented in Table 4.10. Additionally, for Cu,Zn-UoC-5(1F) and Co,Zn-UoC-5(1F) the synthesis parameters leading to the formation of their single crystals are given.

Table 4.10: A comparison of the selected synthesis parameters for the syntheses of Zn-UoC-5(1F), Cu,Zn-UoC-5(1F), Cu,Zn-UoC-5(2F), Co,Zn-UoC-5(1F) and Co,Zn-UoC-5(2F).

Compound	Solvent	Reaction Temp.	Dwell Time	Cooling Time
Zn-UoC-5(1F) (crystals)	DMA	100 °C	24 h	12 h
Cu,Zn-UoC-5(1F) (powder)	DMA	120 °C	48 h	12 h
Cu,Zn-UoC-5(1F) (crystals)	DMA	120 °C	48 h	48 h
Cu,Zn-UoC-5(2F) (powder)	DMA	120 °C	48 h	24 h
Co,Zn-UoC-5(1F) (powder)	DMF	120 °C	48 h	12 h
Co,Zn-UoC-5(1F) (crystals)	DMF	120 °C	48 h	24 h
Co,Zn-UoC-5(2F) (powder)	DMF	120 °C	48 h	24 h

Single crystals of Cu,Zn-UoC-5(2F) and Co,Zn-UoC-5(2F) suitable for scXRD were not obtained, despite modifications to the synthesis conditions. However, the similarity of the PXRD patterns across all UoC-5 derivatives clearly indicates that they are isostructural (see Figure 4.44). Moreover, the PXRD of Cu,Zn-UoC-5(1F) and Co,Zn-UoC-5(1F) confirms their phase purity. It is noteworthy that despite adjusting the synthesis parameters, it was not possible to obtain Zn-UoC-5 in a phase pure form. The PXRD pattern of the least impure product is shown in Figure 4.44 and extraneous reflections with low intensities can still be recognised. In general, it has been a challenge to reproduce Zn-UoC-5(1F) and Co,Zn-UoC-5(1F). In many cases, it was observed

that different frameworks formed under otherwise identical synthetic conditions. The compounds that form in competition to Zn-UoC-5(1F) and Co,Zn-UoC-5(1F) are briefly reviewed in Chapter 4.3.4 (see p. 81 and following).

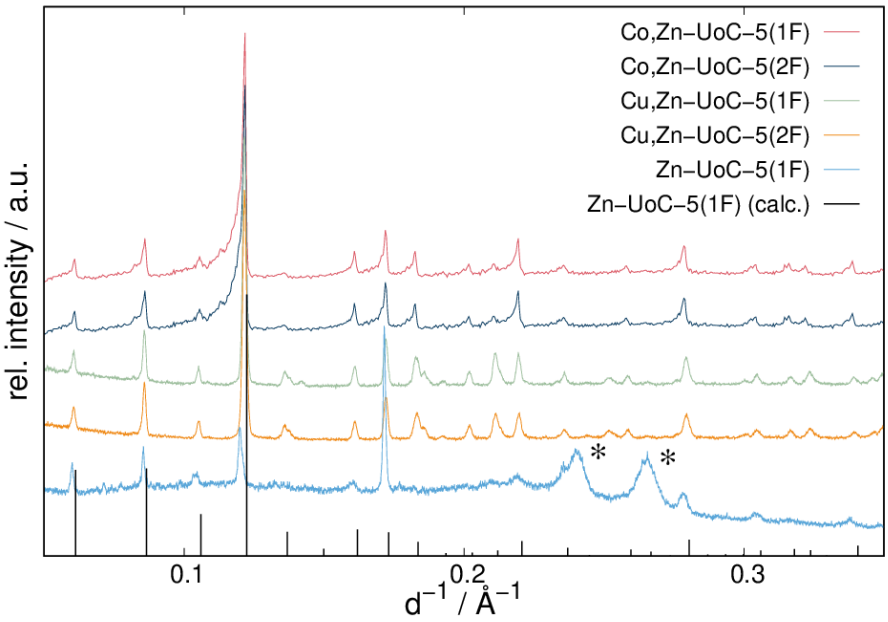

Figure 4.44: PXRD pattern of Zn-UoC-5(1F)[4] (*Huber G670*, Cu Kα_1 radiation (λ = 1.5406 Å), *: additional reflections due to the foil of the sample holder), as well as PXRD pattern of Cu,Zn-UoC-5(1F), Cu,Zn-UoC-5(2F), Co,Zn-UoC-5(1F), and Co,Zn-UoC-5(2F) (*Rigaku MiniFlex600-C*, Cu Kα radiation (λ = 1.5418 Å)).

4.3.2 Thermal Behaviour of Cu,Zn-UoC-5(1F), Cu,Zn-UoC-5(2F) and Co,Zn-UoC-5(1F)

The first detailed investigations of the thermal and sorption behaviours of Cu,Zn-UoC-5(1F), Cu,Zn-UoC-5(2F) and Co,Zn-UoC-5(1F), are presented below. The resulting DSC/TGA curves of Cu,Zn-UoC-5(1F) and Cu,Zn-UoC-5(2F) are shown in the following Figure 4.45 (see p. 75).
For both MOFs, the TGA curves show a similar slight mass loss up to 150 °C, indicating the release of water. At this temperature, the slopes of the TGA curves change.
At approximately 320 °C to 340 °C, an inflection point can be determined (see also the DTG curves of both MOFs on p. 146 and following).
Up to this temperature range, the TGA curves indicate a mass loss of 30 %. Since Cu,Zn-UoC-5(1F) and Cu,Zn-UoC-5(2F) were synthesized in DMA, these mass losses may be attributed to the release of ten to eleven DMA molecules from the pores. For ten and eleven DMA molecules, mass losses of 29 % and 31 % are calculated, respectively.

Since no solvent molecules could be refined for Cu,Zn-UoC-5(1F) in the single-crystal structure analysis, the residual electron density within the solvent-accessible voids of the compound was removed using the *SQUEEZE*[66] routine within *PLATON*.[93] *SQUEEZE*[66] calculated 1275 residual electrons per unit cell. With Z = 4, this corresponds to approximately 318 residual electrons per formula unit. If the release of water molecules is neglected, assuming that only DMA molecules are present in the pores, six to seven DMA molecules would be consistent with the calculated residual electron density. A mass loss of approximately 22 % is calculated for the release of seven DMA molecules per formula unit, which is lower than the value indicated by the TGA curve (30 %). This discrepancy may be explained by the simultaneous release of solvent and the decomposition of the MOF via decarboxylation.

The final step in the TGA curves of Cu,Zn-UoC-5(1F) and Cu,Zn-UoC-5(2F) after the inflection point at approximately 320 °C corresponds to the decomposition of the MOF.

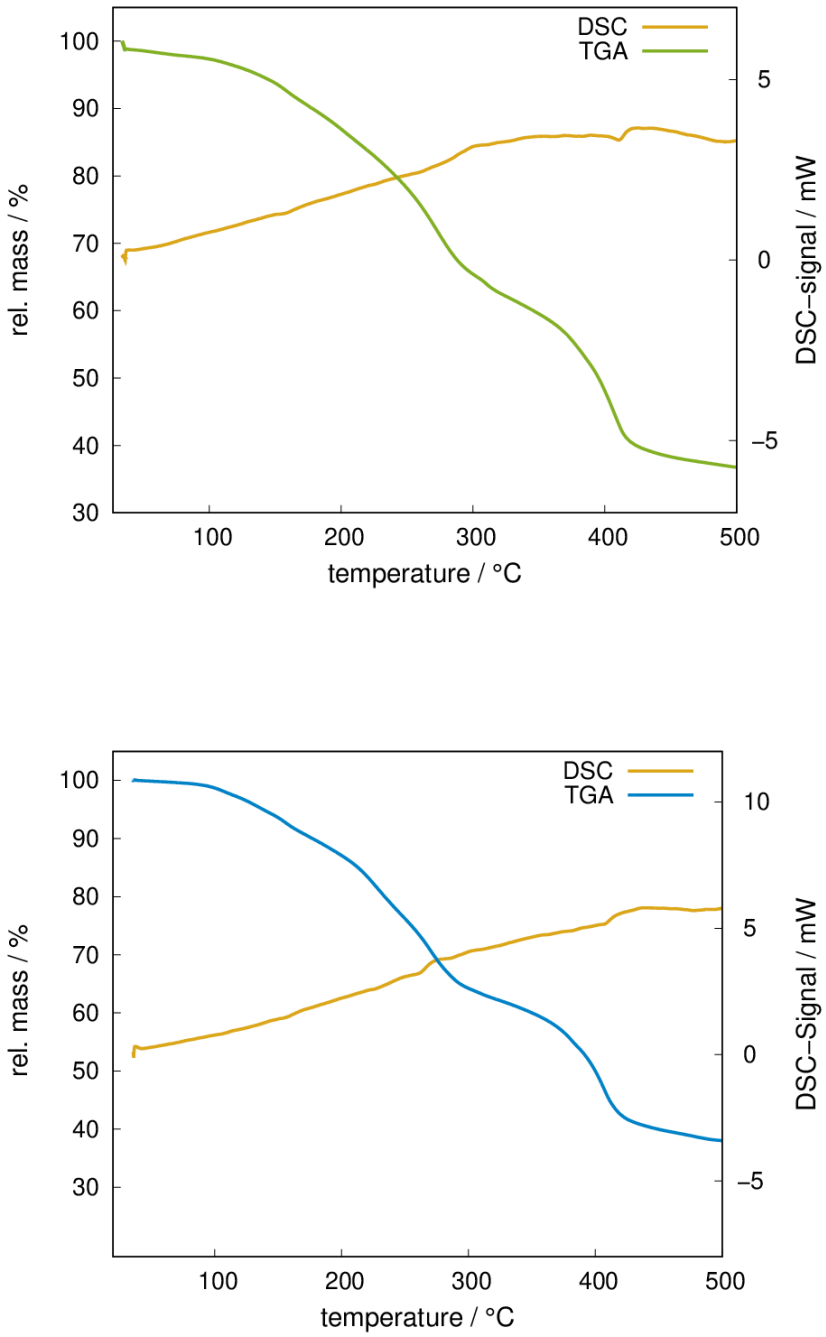

Figure 4.45: DSC/TGA curves of Cu,Zn-UoC-5(1F) (top). DSC/TGA curves of Cu,Zn-UoC-5(2F) (bottom), heated at 10 °C/min under steady argon gas flow to a maximum temperature of 500 °C.

The DSC/TGA curves of Co,Zn-UoC-5(1F) are shown in Figure 4.46.
The TGA curve shows an initial mass loss of 13 % up to 250 °C. This mass loss aligns with an endothermic signal observed in the DSC curve. This mass loss is most likely due to the release of water and DMF molecules. The TGA curve then shows a plateau until approximately 300 °C. In this temperature range, the MOF seems to be thermally stable.

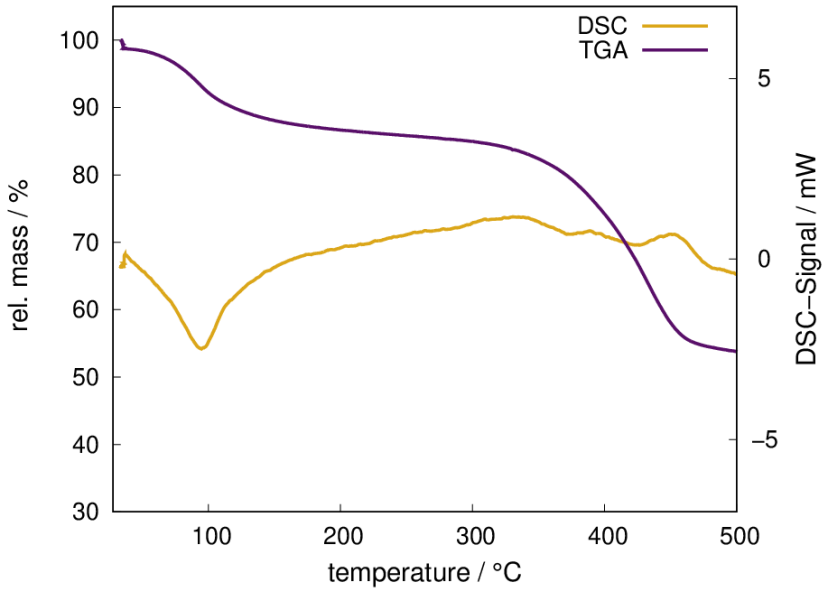

Figure 4.46: DSC/TGA curves of Co,Zn-UoC-5(1F), heated at 10 °C/min under steady argon gas flow to a maximum temperature of 500 °C.

The subsequent mass loss of approximately 34 % up to 480 °C corresponds with two exothermic signals observed in the DSC curve. This mass loss is probably due to the release of uncoordinated DMF molecules and the decomposition of the MOF. These two processes cannot be distinguished in this analysis. Similar to Cu,Zn-UoC-5(1F),

the residual electron density within the solvent-accessible voids of the compound was removed using *SQUEEZE*[66] within *PLATON*.[93] *SQUEEZE*[66] calculated 2638 residual electrons per unit cell. Based on this calculation and the assumption that only DMF molecules are present in the pores, it is estimated that 16 to 17 DMF molecules could be accommodated. A mass loss of approximately 44 % is calculated for the release of 16

DMF molecules per formula unit. This value would be similar to the mass loss observed up to 480 °C in the TGA analysis (47 %). This observation suggests that the compound remained stable and did not decompose until it reached 500 °C. To confirm this, further analysis is required, such as PXRD analysis on the residue after the TGA measurement up to this temperature. This can provide insights into whether the crystal structure is still intact or if it has decomposed into other products.

4.3.3 Adsorption Behaviour of Cu,Zn-UoC-5(1F) and Cu,Zn-UoC-5(2F)

In the course of this work, the sorption behaviour of Cu,Zn-UoC-5(1F) and Cu,Zn-UoC-5(2F) was investigated via N_2 sorption measurements for the first time. This resulted in the determination of the pore sizes and specific surface areas of these MOFs. A detailed discussion of these results will be provided below.
In order to achieve optimal activation, isotherms were obtained for both MOFs at different activation temperatures (see appendix on p. 149 and following).
For both MOFs, the highest BET surface areas were calculated from the isotherms obtained after an activation at 160 °C for 24 h under high vacuum (1×10^{-7} mbar).
In the following Figure 4.47, the N_2 sorption isotherms of Cu,Zn-UoC-5(1F) and Cu,Zn-UoC-5(2F) with optimized activation conditions are compared.

The comparison clearly indicates that the specific surface area decreases with an increasing degree of fluorination.
The monofluorinated compound has a specific surface area of $S_{BET} = 1760$ m²/g. The difluorinated compound has a specific surface area of $S_{BET} = 1400$ m²/g, which is in good agreement with the slightly larger fluorine atom in comparison with hydrogen atoms.
The isotherm of Cu,Zn-UoC-5(2F) does not reach saturation but instead shows a steadily increasing N_2 adsorption, which requires further investigation. Currently, there is no explanation for this behaviour, which was reproducible in several experiments.

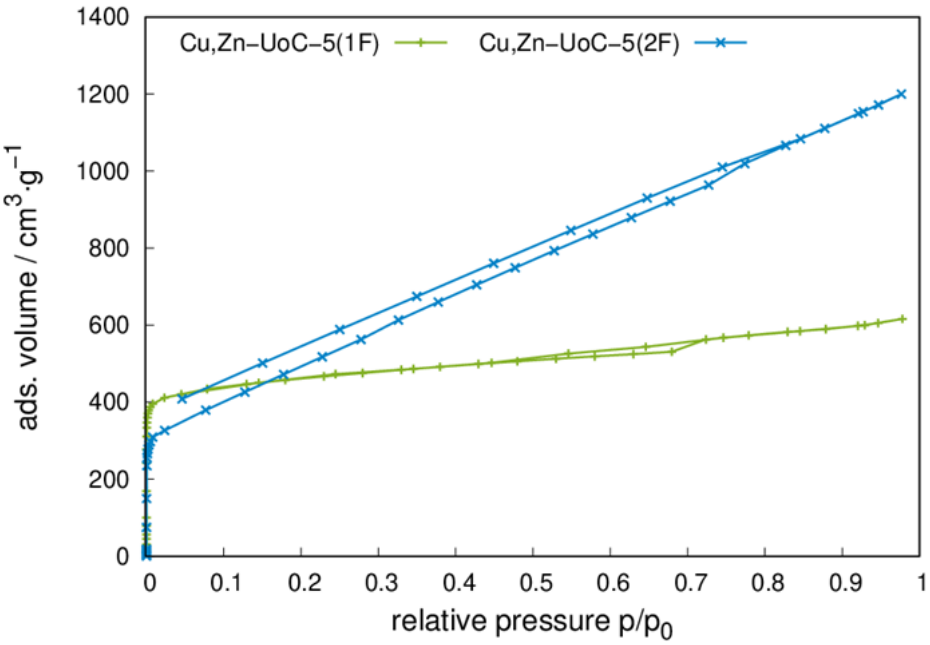

Figure 4.47: N_2 gas sorption isotherms of Cu,Zn-UoC-5(1F) and Cu,Zn-UoC-5(2F) at 77 K after activating at 160 °C for 24 h in high vacuum.

Furthermore, the pore size distribution obtained from N_2 gas sorption measurements as seen in the appendix (p. 131) gave similar results for Cu,Zn-UoC-5(1F) and Cu,Zn-UoC-5(2F).

Both data sets exhibit a maximum at a pore radius of approximately 3 Å, which is in close agreement with the diameter obtained from the structural model derived from the SCXRD.

Finally, a PXRD pattern of Cu,Zn-UoC-5(1F) was measured after the N_2 sorption measurement. It is given as Figure **??** (see p. 80.

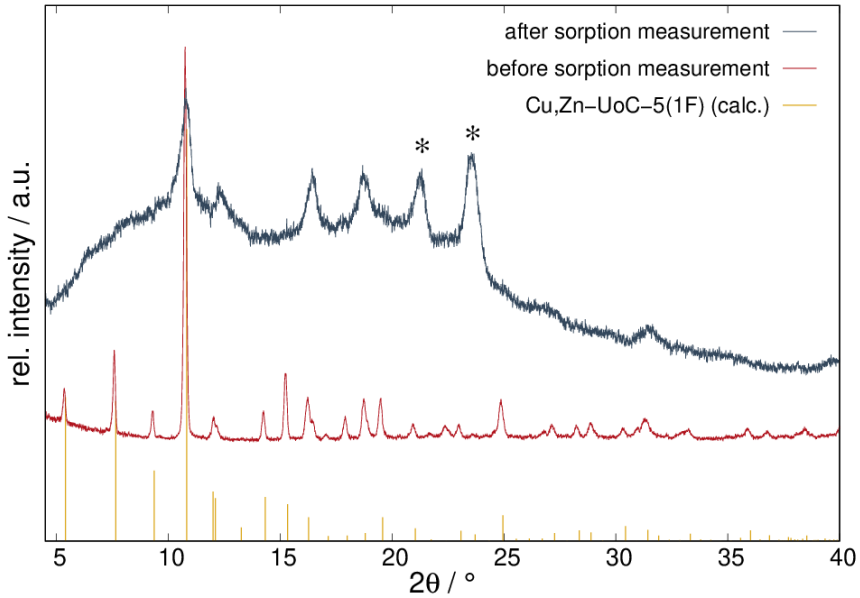

Figure 4.48: PXRD patterns of Cu,Zn-UoC-5(1F) before (*Rigaku MiniFlex600-C*, Cu Kα radiation ($\lambda = 1.5418$ Å)) and after N_2 sorption measurement (*Huber G670*, Cu Kα_1 radiation ($\lambda = 1.5406$ Å), *: additional reflections due to the foil of the sample holder) compared with the calculated reflection positions and intensities from the single crystal data of Cu,Zn-UoC-5(1F).

Only the three strongest reflections of Cu,Zn-UoC-5(1F) were detectable as broad signals in the PXRD pattern, with a high background noise, indicating a significant loss of crystallinity.

To determine whether Cu,Zn-UoC-5(1F) partially decomposes during measurement or if the framework remains intact, an additional experiment was conducted.

In this experiment, Cu,Zn-UoC-5(1F) was heated at 160°C for three days under vacuum. During heating, the powder's color shifted from green to dark green, and finally to black (see Figure 4.49 on p. 80). A PXRD pattern of the resulting black powder was recorded, which showed no reflections, indicating the loss of crystallinity.

Subsequently, the black powder was suspended in DMA for 24 hours. During this time, the powder's color changed back to a green. The PXRD pattern of this greenish powder show the characteristic reflections of UoC-5.

This experiment suggests that the crystallinity can be restored by reintroducing solvent molecules. Therefore, the reduction in crystallinity is only due to the absence of solvent molecules, while the overall framework of the MOF remains intact.
The observations summarised in Figure 4.49 were consistently reproducible throughout the course of this work.

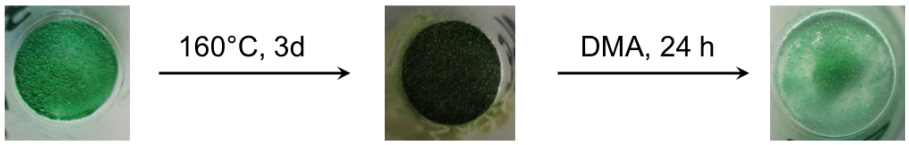

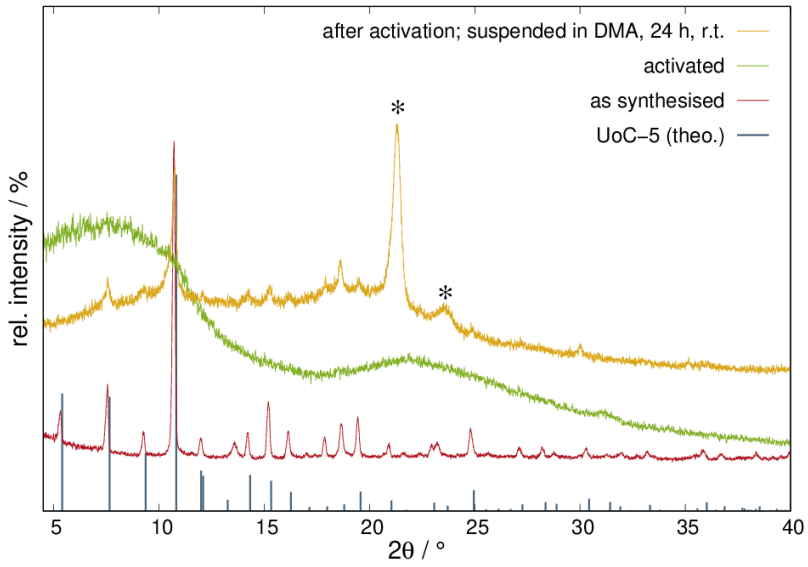

Figure 4.49: PXRD of Cu,Zn-UoC-5(1F) as synthesised (red, *Rigaku MiniFlex600-C*, Cu Kα radiation (λ = 1.5418 Å)) compared to the PXRD of Cu,Zn-UoC-5(1F) after heating at 160 °C for 3 days (green, *Rigaku MiniFlex600-C*, Cu Kα radiation (λ = 1.5418 Å)) and to the PXRD of the heated sample after suspension in DMA (orange, *Huber G670*, Cu Kα_1 radiation (λ = 1.5406 Å), *: additional reflections due to the foil of the sample holder) compared with the calculated reflection positions and intensities from the single crystal data of Cu,Zn-UoC-5 (blue).

4.3.4 Coordination Polymers and MOFs forming alongside the synthesis of Zn-UoC-5(1F) and Co,Zn-UoC-5(1F)

The preparation of Zn-UoC-5(1F) and Co,Zn-UoC-5(1F) has proven to be a challenge. Zn-UoC-5(1F) was not obtained phase pure in the course of this work. The PXRD pattern of the product with the fewest impurities is shown in Figure 4.44 (see p. 73).[4] It was synthesised by heating a mixture of K(H_2*mF*BTC) (1.0 equiv), $Zn(NO_3)_2 \cdot 6\,H_2O$ (3.1 equiv) and DMA to 100 °C within 2 h, maintaining this temperature for 48 h, and cooling it down to room temperature within 12 h.[4] However, under the same conditions, four additional compounds also formed. Their crystals are shown in Figure 4.50. Furthermore, one compound forms under the identical synthesis conditions as Co,Zn-UoC-5(1F) (see Figure 4.52).

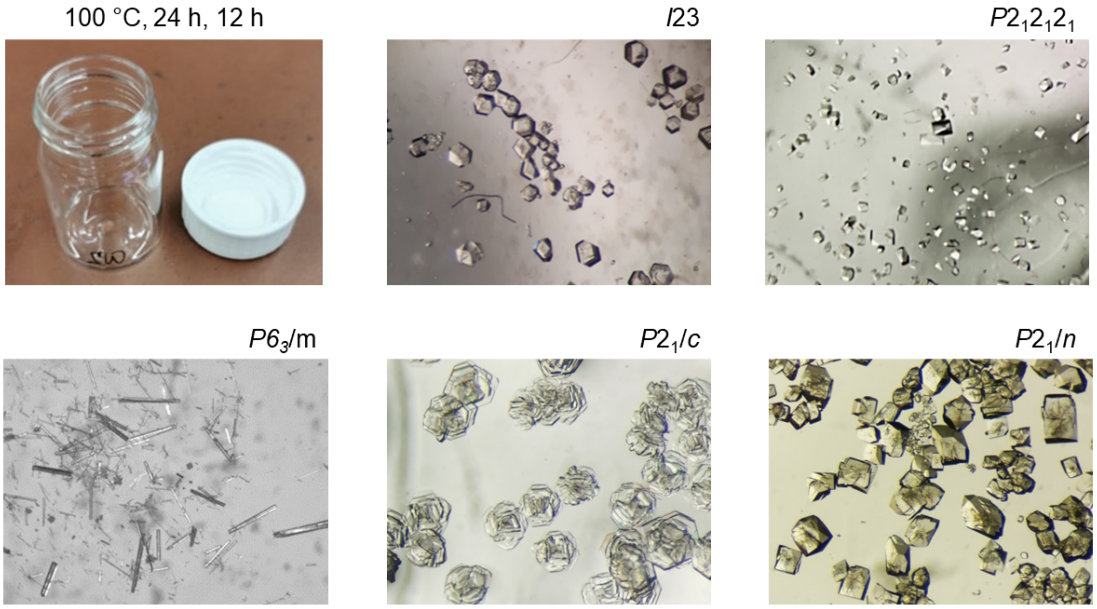

Figure 4.50: Light microscope images of all crystals obtained from the reaction of $Zn(NO_3)_2 \cdot 6\,H_2O$ with K(H_2*mF*-BTC) in DMA at 100 °C for 24 h. Top left: the reaction vessel.

One of four compounds forming alongside Zn-UoC-5(1F) is Zn-UoC-7(1F), whose structure and physical properties are described in detail in Chapter 4.2.1 (see p. 26 and following). Figure 4.51 shows the PXRD of one approach, in which both structures have formed side by side.

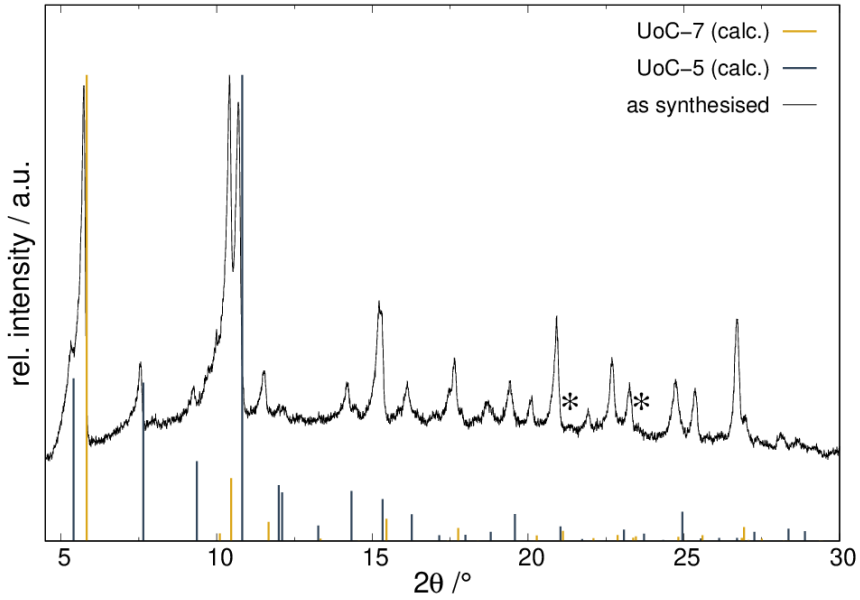

Figure 4.51: PXRD pattern of an approach in which Zn-UoC-5(1F) and Zn-UoC-7(1F) formed side by side (*Huber G670*, Cu Kα_1 radiation (λ = 1.5406 Å) (λ = 1.5406 Å), *: additional reflections due to the foil of the sample holder). For comparison, the reflection positions and intensities calculated from the crystal structure solution of Zn-UoC-5(1F) and Zn-UoC-7(1F) are given.

Since Zn-UoC-7(1F) is a bimetallic MOF incorporating Zn^{2+} and K^+ cations, K(H_2mF–BTC) was replaced by (Bu_4N)(H_2mF–BTC) during synthesis to avoid the formation of Zn-UoC-7(1F). However, Zn-UoC-5(1F) was not accessible by this modified approach.

Another compound that forms in competition with Zn-UoC-5(1F) is $^{2}_{\infty}[Zn_2(HmF{-}BTC)_2(DMA)_2]\cdot 2\,DMA$ (Zn-UHM-31(1F)), which crystallises isostructurally to $^{2}_{\infty}[Cu_2(HmF{-}BTC)_2(DMA)_2]\cdot 2\,DMA$ (UHM-31)[52] in the monoclinic space group $P2_1/c$ (no. 14), with four formula units per unit cell. The structure of Zn-UHM-31(1F) is described in detail in a previous bachelor's thesis[3] in the research group of *Prof. Dr. Uwe Ruschewitz*. Therefore, a structural description is not provided in this thesis.

$^{3}_{\infty}[Zn_2(mF{-}BTC)(NO_3)(DMA)_3]$ also forms under the same synthesis conditions as Zn-UoC-5(1F). This compound crystallises in the orthorhombic space group $P2_1P2_1P2_1$ (no. 19) with four formula units per unit cell.
Moreover, $^{3}_{\infty}[Co_2(mF{-}BTC)(NO_3)(DMA)_3]$ could also be synthesised as part of this work, which is isostructural to $^{3}_{\infty}[Zn_2(mF{-}BTC)(NO_3)(DMA)_3]$.
Both structures could not be refined in the course of this work, however, an isostructural non-fluorinated $^{3}_{\infty}[Zn_2(BTC)(NO_3)(DMF)_3]$[102] is already described by *Oh et al.*[102]

$^{3}_{\infty}[Zn_3(mF{-}BTC)_2(DMA)_3]$[103] is the fourth compound forming under the same synthesis conditions as Zn-UoC-5(1F). It crystallises in the monoclinic space group $P2_1/n$ (no. 14) with four formula units per unit cell. Its structural solution is described in detail in a previous bachelor's thesis[103] in the research group of *Prof. Dr. Uwe Ruschewitz*. Therefore, a structural description is not provided in this thesis.

Similar to Zn-UoC-5(1F), the synthesis of Co,Zn-UoC-5(1F) also presented challenges in achieving a phase-pure product. The same synthesis approach often yielded in a mixture of two types of crystals as depicted in Figure 4.52. One can be assigned to Co,Zn-UoC-5(1F) and the other to $^{3}_{\infty}[CoZn_2(mF{-}BTC)_2(DMA)_3]$ crystallises isostructurally to $^{3}_{\infty}[Zn_3(mF{-}BTC)_2(DMA)_3]$[103].

Selected crystallographic data of $^{3}_{\infty}[CoZn_2(mF{-}BTC)_2(DMA)_3]$ are summarised in Table 7.1 (see p. 152). Additional crystal data are provided in the attached CIF file. Moreover, its asymmetric unit can also be found in the appendix (see Figure 7.35, p. 153).

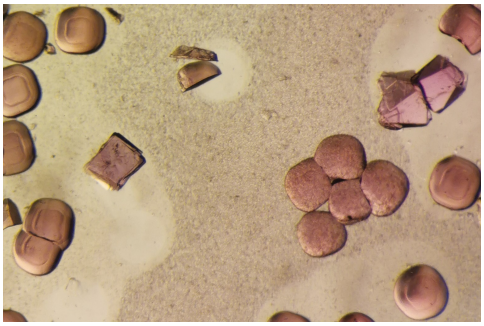

Figure 4.52: Image of a mixture of single crystalline $^{3}_{\infty}[CoZn_2(mF{-}BTC)_2(DMA)_3]$ and Co,Zn-UoC-5(1F), taken under a light microscope.

4.4 Influence of the Fluorination on the Thermal and Sorption Properties of the resulting MOFs

The thermal stability of MOFs based on aromatic carboxylate linkers is expected to be reduced by increasing the number of fluorine substituents at the phenyl ring of the linker. This can be explained by the electron-withdrawing effect of fluorine increasing the propensity for decarboxylation.[55,56]
Since the two presented MOF systems, Zn-UoC-7(1F)/Zn-UoC-7(2F) and Cu,Zn-UoC-5(1F)/Cu,Zn-UoC-5(2F), are isostructural and differ only in their degree of fluorination, it was possible to investigate how varying degrees of fluorination influence the thermal behaviour of the respective MOFs.[56,82–84]

Figure 4.53 compares the TGA curves of Zn-UoC-7(1F) and Zn-UoC-7(2F). A more detailed description of the thermal behaviour of both MOFs is provided in Chapter 4.2.1 (see p. 37).

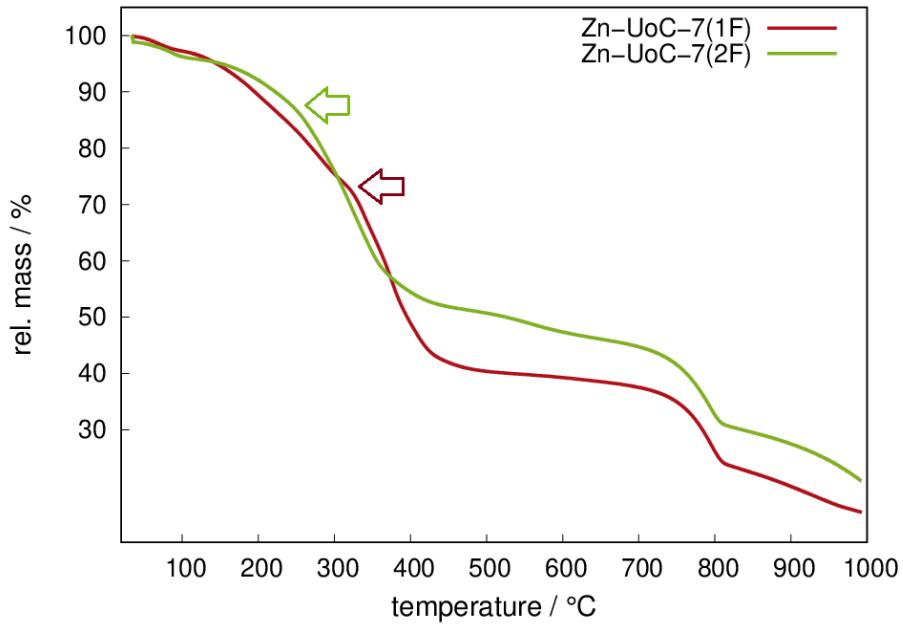

Figure 4.53: TGA curve of Zn-UoC-7(1F) (red) compared to the TGA curve of Zn-UoC-7(2F) (green). The arrows are intended to indicate where the decomposition of the MOFs is estimated to occur.

Determining the decomposition temperature of both MOFs is difficult due to the simultaneous release of uncoordinated solvent molecules, accompanied by the concurrent decomposition of the cations and frameworks.
Zn-UoC-7(1F) appears to commence decomposition at approximately 300°C, as indicated by the inflection point observed in its TGA curve. In contrast, the TGA curve of Zn-UoC-7(2F) does not exhibit a distinct inflection point until around 400°C. Nonetheless, a notable decline is observed between 260°C and 280°C, a feature more distinctly evident in the DTG curve of Zn-UoC-7(2F) (see appendix, p. 145). This suggests that Zn-UoC-7(2F) may begin to decompose at this lower temperature.
Therefore, as described in literature[56,82–84], the more highly fluorinated Zn-UoC-7(2F) decomposes at a lower temperature compared to the less fluorinated Zn-UoC-7(1F).

Similar to Zn-UoC-7(1F) and Zn-UoC-7(2F), determining the decomposition temperatures of Cu,Zn-UoC-5(1F) and Cu,Zn-UoC-5(2F) is complicated by the potential overlap of

uncoordinated solvent molecule release with the decomposition of the frameworks. The TGA curves of these MOF are compared in Figure 4.54.

The TGA curves of both MOFs exhibit an inflection point within the temperature range of approximately 320 °C to 340 °C, which is more distinctly visible in the DTG curves (see appendix, p. **??** and following). This indicates that both MOFs begin to decompose within this temperature range. Consequently, it appears that higher fluorination does not influence the thermal stability of Cu,Zn-UoC-5.

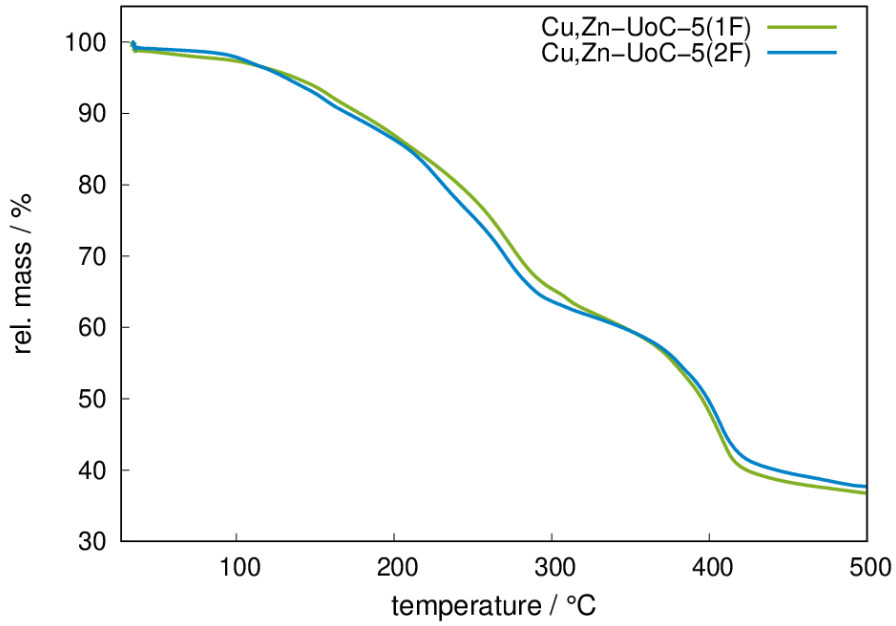

Figure 4.54: TGA curve of Cu,Zn-UoC-5(1F) (green) compared to the TGA curve of Cu,Zn-UoC-(2F) (blue).

Furthermore, with a higher degree of fluorination, the CO_2 uptake of Zn-UoC-7 is enhanced demonstrated through the CO_2 sorption measurements that were conducted on Zn-UoC-7 (see Chapter 4.3.3, p. 77). This indicates that Zn-UoC-7(2F) interacts stronger with the CO_2 guest molecules This is in agreement with previous observations for other MOFs.[17,52] *Peikert et al.* attributed this stronger interactions to the relatively

high quadrupole moment of fluorine.[17]

In addition to the CO_2 gas sorption measurements on Zn-UoC-7(1F)/Zn-UoC-7(2F), N_2 gas sorption measurements were conducted on Zn-UoC-7(1F)/Zn-UoC-7(2F) and Cu,Zn-UoC-5(1F)/Cu,Zn-UoC-5(2F).
The specific surface area of Zn-UoC-7(1F) is $S_{BET} = 2740\,\mathrm{cm^2/g}$, while the corresponding value for Zn-UoC-7(2F) is significantly lower at $S_{BET} = 1643\,\mathrm{cm^2/g}$ (see Figure 4.22 on p. 42). Similarly, Cu,Zn-UoC-5(1F) exhibited a specific surface area of $S_{BET} = 1760\,\mathrm{cm^2/g}$, which is higher than the $S_{BET} = 1400\,\mathrm{m^2/g}$ observed for the higher fluorinated Cu,Zn-UoC-5(2F). This reduction in specific surface area with increased fluorination aligns with the larger *van der Waals* radius of fluorine compared to hydrogen.

In conclusion, the observed trends regarding the influence of the number of fluorine substituents on the two MOF Zn-UoC-7(1F) and Zn-UoC-7(2F) align with the expectations. These findings are consistent with those reported for other MOF systems in the literature.[17,52,55,56]

4.5 Additional Syntheses

In the present thesis, MOF structures are described which are based on the fluorinated BTC^{3-} linker. The synthesis parameters of these MOFs were adopted, whereby the K(H_2mF/dF–BTC) were replaced by H_3mF/dF–BTB. Similarly to BTC^{3-}, BTB^{3-} is a tritopic organic linkers, but with an enlarged backbone. As described in the scientific opjective (see Chapter 2, p. 2), it was aimed to synthesise isoreticular MOFs, maintaining the same general frameworks while varying the size of the linkers. Ultimately, these approaches have not yet been successful. In most cases, no product precipitated, or the precipitation was amorphous.

Furthermore, H_3mF–BPTC was synthesised and reacted with various transition metals. The reaction of $Zn(NO_3)_2 \cdot 6\,H_2O$ with H_3mF–BPTC yielded colourless crystals, while the reaction of $Co(NO_3)_2 \cdot 6\,H_2O$ with H3mF-BPTC yielded pink crystals. The crystals resulting from both approaches are shown in Figure 4.55. However, they were found

to be unsuitable for SCXRD, which is the reason why these two products could not be identified and further characterised.

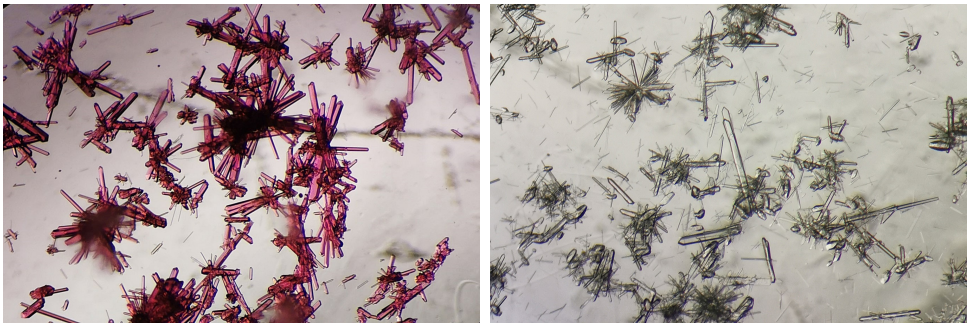

Figure 4.55: The reaction of $Co(NO_3)_2 \cdot 6\,H_2O$ with H_3mF–BPTC yielded pink crystals (left), while the reaction of $Zn(NO_3)_2 \cdot 6\,H_2O$ with H_3mF–BPTC yielded colourless crystals (right).

5 Conclusion

The principal objective of this doctoral thesis was the preparation and structural analysis of MOFs containing divalent zinc, copper, and cobalt cations as well as trimesate linkers with varying degrees of fluorination. To accomplish this, K(H_2*mF*–BTC) and K(H_2*dF*–BTC) were successfully synthesised and reacted with the corresponding metal salts.

The reaction of these linkers with $Zn(NO_3)_2 \cdot 6\,H_2O$ in DMA/DMF:EtOH resulted in the formation of $^{3}_{\infty}[((CH_3)_2NH_2)K_2Zn_3(mF/dF\text{–BTC})_3(H_2O)]$ (Zn-UoC-7(1F) and Zn-UoC-7(2F)). Both MOFs crystallise in the hexagonal space group $P6_3/m$ (no. 176). The crystal structures of Zn-UoC-7(1F) and Zn-UoC-7(2F) were previously described in a bachelor's thesis[3] and a master's thesis,[4] respectively. In the course of this work, phase-pure samples of both compounds were successfully synthesised, the structure solutions were significantly improved, and their material properties were characterised in detail.

Zn-UoC-7(1F) and Zn-UoC-7(2F) exhibit large channels running along [001] with a diameter of approximately 11.7 Å. N_2 gas sorption measurements reveal large surface areas of $S_{BET} = 2740\,m^2/g$ for Zn-UoC-7(1F) and $S_{BET} = 1643\,m^2/g$ for Zn-UoC-7(2F). Moreover, both MOFs exhibit high CO_2 uptake, with Zn-UoC-7(1F) showing a lower uptake compared to Zn-UoC-7(2F). Remarkably, Zn-UoC-7(2F) achieves an exceptionally high CO_2 uptake of $247\,cm^3/g$ at 273 K, which is among the highest values reported for MOFs to date.[2] This can be attributed to the narrow pore size[96] and the strong interactions between the fluoro substituents of the linker and the CO_2 guests.

Zn-UoC-7 is the first anionic MOF based on fluorinated trimesate linkers. The anionic framework is charge-balanced by $(CH_3)_2NH_2^+$ cations, which are generated by the hydrolysis of the solvents DMF and DMA. In this thesis, the $(CH_3)_2NH_2^+$ cations were successfully localised within the MOF pores using SCXRD.

The use of larger cations did not result in a templating effect. Instead, a slight, but significant increase of the lattice parameters was observed.

The aforementioned results have already been published as a hot paper article in *Chemistry – A European Journal.*[1]

$K(H_2BTC) \cdot H_2O$[81] was successfully synthesised, however, the attempts to synthesise an unfluorinated MOF isostructural to Zn-UoC-7 has been unsuccessful so far.
Moreover, the synthesis of an isostructural MOF with the pF–BTC^{3-} linker was impeded by the limited availability of the reactants required for the synthesis of the linker. None of the attempts to develop new synthetic pathways yielded sufficient quantities of the products for further investigations.
Furthermore, an isostructural cobalt compound, Co-UoC-7(2F), was synthesised in the form of a crystalline powder. Although attempts to isolate single crystals from this powder were unsuccessful, PXRD analysis unambiguously confirmed that it crystallises isostructurally to Zn-UoC-7(1F) and Zn-UoC-7(2F).
Subsequent approaches to synthesize further derivatives from divalent metal cations, such as Cu^{2+} and Mg^{2+}, have not been successful to date. Since the synthesis of isostructural MOFs with varying linkers or metals consistently requires different syntheses conditions, it is plausible that further optimisation of the parameters could lead to the formation of derivatives with other metal cations in the future.

Another anionic MOF synthesised in this work was UoC-13(1F), which crystallises in the tetragonal space group $I\bar{4}$ (no. 82) with four formula units per unit cell and is described as $^{3}_{\infty}[((CH_3)_2NH_2)_3In_3(mF\text{–}BTC)_4]$.
Similar to UoC-7, the anionic framework of UoC-13(1F) is compensated by $(CH_3)_2NH_2{}^+$ cations formed via hydrolysis of the solvent DMF. The use of DEF, which hydrolyses to larger cations, did not result in a templating effect.
The residual electron density within the solvent-accessible voids of UoC-13(1F) was removed using the *SQUEEZE*[66] routine of *PLATON*.[93] This procedure identified solvent-accessible voids of 5723 Å^3 per unit cell, which corresponds to 56 % of the total unit cell volume. Based on the single-crystal analysis, the potential voids have an approximate diameter of 8 Å. In the course of this work, no type I isotherm has been obtained for UoC-13(1F). However, single-crystal analysis indicates the porosity of this compound, so repeating the adsorption measurements is recommended.

GaMOF-1(1F) is the third anionic MOF structure investigated in the course of this work. Based on single crystal X-ray diffraction, its composition may be described as $^{3}_{\infty}[((CH_3)_2NH_2)_3Ga_3(mF\text{–}BTC)_4]$. As the molecular formula shows, the anionic framework of GaMOF-1 is also compensated by $(CH_3)_2NH_2{}^+$ cations formed by the hydrolysis

of DMF. It crystallises isostructurally to the unfluorinated GaMOF-1[22] and amino-substituted GaMOF-1(NH_2)[98] in the cubic space group $I\bar{4}3d$ (no. 220). GaMOF-1(NH_2)[98] exhibited no measurable internal surface area, while a BET surface area of $S_{BET} = 205\,m^2/g$ was reported for GaMOF-1,[22] which is relatively low in comparison to many other highly porous MOFs. Consequently, it was not attempted to activate GaMOF-1(1F).

In addition to the anionic MOFs, a series of MOFs featuring neutral frameworks was investigated. The crystal structure of these MOFs was first described in a previous bachelor's thesis with the reported Zn-UoC-5(1F).[3] Based on this single crystal analysis, UoC-5 crystallises in the cubic space group $I23$ (no. 197) with four formula units per unit cell, and is best described as $[[Zn_4O]_4[M_2(H_2O)_2]_3(mF/dF\text{–}BTC)_{12}]$ (M = Zn, Cu, Co). A notable aspect of the UoC-5 structure is the presence of two SBUs: a paddlewheel unit $M(COO)_4$ (M = Zn, Cu, Co) and an octahedral $Zn_4O(COO)_6$ unit.
In the course of this work, Cu,Zn-UoC-5(1F) and Co,Zn-UoC-5(1F) were obtained as single crystals for the first time, which enabled their structural characterisation via single crystal X-Ray diffraction.
The partial substitution of Zn^{2+} with Cu^{2+} or Co^{2+} does not significantly impact the unit cell parameters, which can be attributed to the similar ionic radii of these cations.[104]
Despite many efforts, single crystals suitable for SCXRD analysis of Cu,Zn-UoC-5(2F)[4] and Co,Zn-UoC-5(2F) were not obtained. However, the PXRD patterns indicated that all UoC-5 derivatives are isostructural, and phase purity was confirmed for Cu,Zn-UoC-5(1F) and Co,Zn-UoC-5(1F).
XPS was employed to analyse the chemical composition of Cu,Zn-UoC-5(1F), yielding a zinc-to-copper ratio of approximately 3:1, both in the +II valence state. This ratio deviates from the 8:3 ratio determined by SCXRD analysis. This discrepancy may result from the uneven distribution of metals within the bulk sample.
For Cu,Zn-UoC-5(1F), a specific surface area of $S_{BET} = 1760\,m^2/g$ was measured, whereas Cu,Zn-UoC-5(2F) exhibited a smaller specific surface area of $S_{BET} = 1400\,m^2/g$. Presumably due to the larger size of fluorine compared to hydrogen.

The synthesis of Zn-UoC-5(1F) and Co,Zn-Uoc-5(1F) was particularly challenging, often resulting in the formation of another undesired (side-) product: Zn-UoC-7(1F), Zn-UHM-33(1F)[3] crystallising in the monoclinic space group $P2_1/c$ (no. 14), $^{2}_{\infty}[Zn_2(BTC)(NO_3)(DMF)_3]$ crystallising in the space group $P2_1P2_1P2_1$ (no. 19) and $^{3}_{\infty}[Zn_3(mF{-}BTC)_2(DMA)_3]$ crystallising in the monoclinic space group $P2_1/n$ (no. 14).

Furthermore, the isostructural MOFs with varying degrees of fluorination were investigated with respect to the influence of fluorination on their thermal behaviour and sorption properties. As expected, the higher fluorinated Zn-UoC-7(2F) decomposes at a lower temperature than the less fluorinated Zn-UoC-7(1F). This can be explained by the electron-withdrawing effect of fluorine increasing the propensity for decarboxylation.[55,56] However, it must be noted that the simultaneous release of uncoordinated solvent molecules, along with the decomposition of both the cations and the frameworks, complicates the determination of an exact decomposition temperature.
Similarly, for Cu,Zn-UoC-5(1F) and Cu,Zn-UoC-5(2F), the determination of decomposition temperatures is complicated by the release of uncoordinated solvent molecule merging with the decomposition of the frameworks.
The TGA curves of both MOFs indicates that both MOFs begin to decompose within the temperature range of approximately 320 °C to 340 °C. Consequently, it appears that higher fluorination does not influence the thermal stability of Cu,Zn-UoC-5.
Additionally, it was demonstrated that Zn-UoC-7(2F) interacts stronger with CO_2 guest molecules than Zn-UoC-7(1F). Remarkably, Zn-UoC-7(2F) achieves an exceptionally high CO_2 uptake of 247 cm^3/g at 273 K, which is one of the highest CO_2 uptake reported to date.[2]
In conclusion, additional isostructural MOFs with varying degrees of fluorination could provide deeper insights into the trends observed in this doctoral thesis. It would also be valuable to synthesize the previously presented MOF systems with substituents that exhibit effects opposite to those of fluorine, such as amino or methoxy groups. UoC-7 is of particular interest in this context. The selective CO_2 adsorption of UoC-7 should be further investigated, and its adsorption capacity could potentially be enhanced through the modification of linkers and metal nodes. In any case, its thermal stability and exceptionally high CO_2 uptake capacity suggest promising applications in fields related to climate change mitigation and sustainable energy supply.

6 Experimental Section

6.1 Data Handling

All experiments were performed under the supervision of Prof. Dr. Uwe Ruschewitz at the University of Cologne. They were documented in lab books, which are archived in the research group of Prof. Dr. Uwe Ruschewitz. Data obtained within these experiments and data obtained from collaborations are stored on the server of the research group.

6.2 General Information

Experiments including air and water-sensitive chemicals were carried out under inert conditions using *Schlenk* technique under an argon atmosphere.

The silica gel used in this work was sourced from *Acros Organics* with a particle size of 0.035–0.070 mm and a pore size of 60 Å. For thin-layer chromatography, either TLC Silicagel 60 F254 plates by *Merck* or ALUGRAM Xtra SIL G/UV254 sheets by *Macherey-Nagel* were used. The spots were detected under UV radiation ($\lambda = 254$ nm) or by using a $KMnO_4$ solution as staining agent. Unless stated otherwise, all solvent mixtures are given as volume fractions.

6.3 Solvents and Reagents

Unless otherwise specified, all solvents and reagents of synthetic grade were used as commercially supplied. Table 6.1 summarises all the chemicals with their supply source and purity used in this work. If further purification or drying was required, the procedures used are described by Armarego.[105]

Table 6.1: List of chemicals used, along with their suppliers and purity information.

Chemical	**Purity**	**Source**
Acetic acid	n.s.	n.s.
Acetone	n.s.	VWR Chemicals
Acetonitrile	HPLC grade	Fischer Chemicals
Argon	99.9997 %	Air Products
1,3,5-Benzenetricarboxylic acid	98 %	Merck
5-Bromo-2-fluoroxylene	98.10 %	BLD Pharmatech
4-Bromo-2-fluorobenzaldehyde	98 %	BLD Pharmatech
4-Bromo-3-fluorobenzaldehyde	98 %	BLD Pharmatech
Chloroform-d	99.8 %	Eurisotop
Copper(II) nitrate trihydrate	> 99, 5%	Sigma Aldrich
Cobalt(II) nitrate hexahydrate	> 99%	Fluka
Cyclohexane	n.s.	n.s.
Dichloromethane	n.s.	Biesterfeld
Diethylether	99.5 %	Fischer Scientific
3,5-Difluoro-4-formylphenylic acid	95 %	Fluorochem
2,4-Difluoro-1,3,5-trimethylbenzene	98 %	ABCR
N,N-Dimethylacetamide	99 %	ABCR
N,N-Dimbutylformamide	99 %	ABCR
N,N-Dimethylformamide	99 %	ABCR
3,5-Dimethylphenylboronic acid	99.91 %	BLD Pharmatech
Dimethylsulfoxid-d_6	99.8 %	Eurisotop
1,4-Dioxane	n.s.	Riedel-de-Haën
Ethanol	99.8 %	Biesterfeld
Ethyl acetate	HPLC	Biesterfeld
2-Fluoro-1,3,5-trimethylbenzene	99.9 %	BLD Pharmatech
2,4-Fluoro-1,3,5-trimethylbenzene	99.9 %	BLD Pharmatech
Gallium(III) nitrate hydrate	99.9 %	Alfa Aesar
Hydrochloric acid (37 %)	n.s.	n.s.
Hydrogen peroxide	n.s.	Fischer Scientific

Table 6.1 will be continued on the next page.

Table 6.1: List of the used chemicals with their supply source and information on their purity. - Continued.

Chemical	**Grade**	**Source**
Indium(III) nitrate hydrate	99.99 %	Alfa Aesar
Iodine	n.s.	n.s.
Magnesium chloride	99 %	Alfa Aesar
Magnesium nitrate	n.s.	n.s.
Magnesium sulfate	n.s.	n.s.
Methanol	n.s.	BCD Chemie
2-Methyl-propan-2-ol	99 %	Fischer Scientific
n-Hexan	n.s.	n.s.
Nitric acid	n.s.	n.s.
Orthoperiodic acid	99 %	Fischer Scientific
Potassium hydroxide	98 %	Acros Organics
Potassium carbonate	n.s.	n.s.
Potassium iodide KI	99.9 %	BLD Pharmatech
Potassium permanganate	98 %	Acros Organics
Propan-2-ol	n.s.	Biesterfeld
Pyridine	99 %	Fischer Scientific
Sulfuric acid	n.s.	n.s.
Sodium cloride	n.s.	n.s.
Sodium hydroxide	97 %	Fischer Scientific
Sodium thiosulfate	99 %	Alfa Aesar
Tetrachlormethane	n.s.	n.s.
Tetrahydrofuran	99.8 %	Fischer Scientific
Tetrakis-(tri-phenyl-phosphin)-palladium(0)	n.s.	Carbolution
Triethylamine	99 %	Fischer Scientific
Toluene	HPLC grade	Fischer Chemicals
1,3,5-Trifluorbenzene	97%	Fluorochem
Zinc(II)nitrat hexahydrat	n.s.	n.s.

6.4 Syntheses of the Linkers

Synthesis of Monopotassium-1,3,5-benzenetricarboxylate

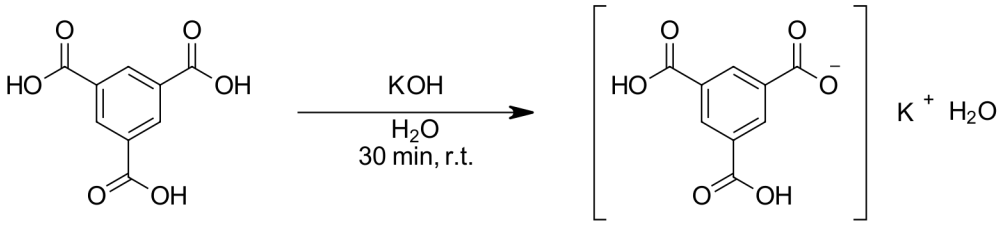

A solution of 0.27 g (4.76 mmol, 1.0 equiv.) KOH in 10 ml of H_2O was slowly added to a suspension of 1.00 g (4.76 mmol, 1.0 equiv.) 1,3,5–benzenetricarboxylic acid and 50 ml of H_2O. The suspension was stirred for 30 min. After removing the solvent under reduced pressure, the product was recrystallised from EtOH:H_2O (3:1). The precipitate was filtered off, washed with cold EtOH:H_2O (3:1) and dried under vacuum giving the product as a colourless solid with a quantitative yield.

MF	$KC_9H_5O_6$
MW	$248.23\,g\,mol^{-1}$

^{1}H–NMR (300 MHz, $CDCl_3$) δ / ppm = 8.58 (s, 3H).

Furthermore, the product was characterised via PXRD (see in the appendix on p. 139).

Synthesis of Monopotassium-2-fluoro-1,3,5-benzenetricarboxylate

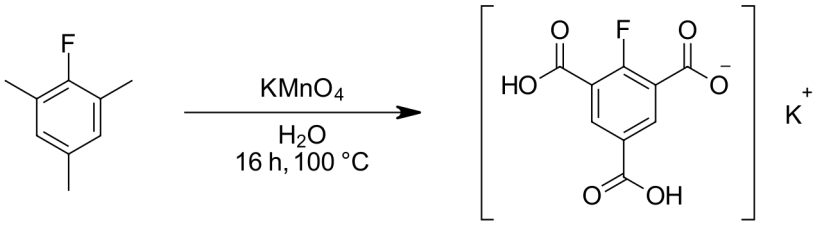

The synthesis followed the main steps described in the literature,[82] but has been modified to improve the yield.

11.90 g (75.3 mmol, 6.9 equiv.) of $KMnO_4$ was dissolved in 200 ml of H_2O. Then, 1.50 g (10.9 mmol, 1.0 equiv.) of 2,4,6–trimethylfluorobenzene was added dropwise. After stirring the suspension at r.t. for 4 h, it was refluxed for 16 h. 5 ml of EtOH was added and the mixture was stirred until it turned colorless. The brown precipitation was filtered off and washed with warm H_2O. The obtained filtrate was concentrated in vacuum, yielding a colorless solid, which was transferred into a Teflon vessel and solved in 10 ml of H_2O. HCl was added dropwise until the precipitation was completed. The precipitate was filtered off, washed with cold H_2O and dried under vacuum, giving 70 % (2.03 g, 7.6 mmol) yield of the product as a colourless solid.

MF	$KC_9H_4FO_6$
MW	266.22 g mol^{-1}
Yield	2.03 g (7.6 mmol, 70 %)

^{1}H–NMR	(300 MHz, D_2O) δ / ppm = 8.48 (d, J = 6.3 Hz, 2H).
^{19}F–NMR	(282 MHz, D_2O) δ / ppm = −108.20 (s, 1F).

The product was also characterised by PXRD (see appendix on p. 140).

Synthesis of Monopotassium-2,4-difluoro–1,3,5-benzenetricarboxylate

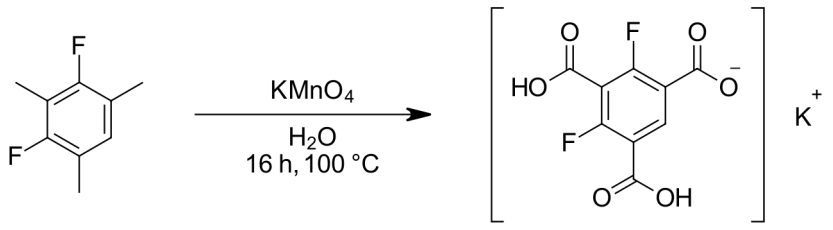

The synthesis followed the main steps described in the literature,[83] but has been modified to improve the yield.

11.00 g (69.6 mmol, 7.3 equiv.) of $KMnO_4$ was dissolved in 200 ml of H_2O. Then 1.50 g (9.6 mmol, 1.0 equiv.) of 2,4–difluoro–1,3,5–trimethylbenzene was added dropwise to the solution. After stirring the reaction mixture at r.t. for 5 h, it was refluxed overnight. 5 ml of EtOH was added, then the mixture was stirred for another 30 min. The brown precipitation was filtered off, and washed with warm H_2O. The colourless filtrate was concentrated in vacuum, yielding a colourless solid. The colourless solid was transferred to a Teflon vessel and solved in 10 ml of H_2O. HCl was added dropwise until the precipitation was completed. The precipitate was filtered off, washed with cold H_2O und dried under vacuum giving 65 % (1.80 g, 6.3 mmol) of the product as a colourless solid.

MF	$KC_9H_3F_2O_6$
MW	284.21 g mol^{-1}
Yield:	1.80 g (6.3 mmol), 66 %

^{1}H–NMR	(300 MHz, D_2O) δ / ppm = 8.40 (t, J = 8.3 Hz, 1H).
^{19}F–NMR	(282 MHz, D_2O) δ / ppm = −108.10 (s, 1F).

The product was also characterised by PXRD (see appendix on p. 140).

Attempted Synthesis of Monopotassium-2,4,6-trifluorobenzene-1,3,5-tricarboxylat

Synthesis of 1,3,5-Trifluoro-2,4,6-triiodobenzene

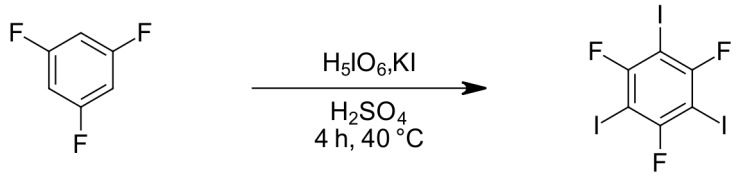

The synthesis followed the steps described in the literature.[85,86]

20 ml of conc. H_2SO_4 were cooled to 0 °C. Then, 3.00 g (13.2 mmol, 1.4 equiv.) of H_5IO_6 were slowly added over a period of 1 h. Subsequently, 6.61 g (39.8 mmol, 4.1 equiv.) of KI and 1.0 ml (9.67 mmol, 1.0 equiv.) of 1,3,5-trifluorobenzene were slowly added to the suspension. The mixture was heated to 40 °C for 4 h. After cooling to r.t., the reaction mixture was poured on 400 ml of ice water. The mixture was extracted four times with 50 ml of methyl-tert-butylether. The combined organic layers were washed four times with a total of 100 ml of sat. $Na_2S_2O_3$ solution before it was dried over $MgSO_4$. After removing the solvent under reduced pressure, the crude product was recrystallized from $EtOH/H_2O$ to yield 4.93 g (9.7 mmol, 97 %) of the product as a colourless solid.

MF	$C_6F_3I_3$
MW	509.71 g mol^{-1}
Yield	4.93 g (9.7 mmol, 97 %)
TLC: R_F (cHex)	0.66
^{13}C-NMR	(75 MHz, $CDCl_3$) δ / ppm = 163.8 (C-1), 160.6 (C-2).
^{19}F–NMR	(282 MHz, $CDCl_3$) δ / ppm = −68.8 (m, F-1).

Attempted Syntheses of 1,3,5-Trifluoro-2,4,6-benzenetricarbonitrile

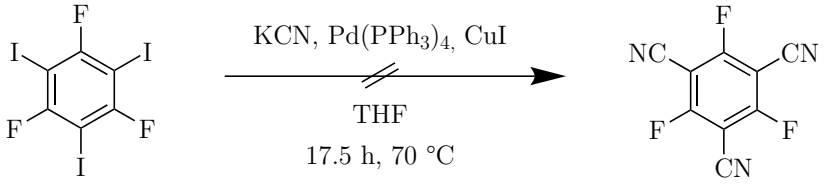

After degassing 10 ml of THF 1.98 g (3.9 mmol, 1.0 equiv.) of 1,3,5-trifluoro-2,4,6-triiodobenzene was added under argon atmosphere. Subsequently, 0.46 g (0.4 mmol) of $Pd(PPh_3)_4$ and 0.075 g (0.4 mmol) of CuI were added followed by the addition of 0.51 g (7.88 mmol, 2.0 equiv.) of KCN in portions. Then, the reaction mixture was heated to 70 °C for 17 h. Then it was allowed to cool to r.t. and 45 ml of EtOAc was added. The resulting suspension was filtered and washed with an aqueous solution of NaCl. 15 ml of THF were added to the combined organic phase dissolving the precipitate. The solvent was removed under reduced pressure to give an orange solid, which is not the desired product.

LR-GC-MS: m/z / % = 382.80 [$C_6F_3I_2^{\cdot}$], 255.90 [$C_6F_3I^{2\cdot}$], 262.09 [PPh_3], 277.07 [$OPPh_3$], 128.99 [$C_6F_3{}^{3\cdot}$].

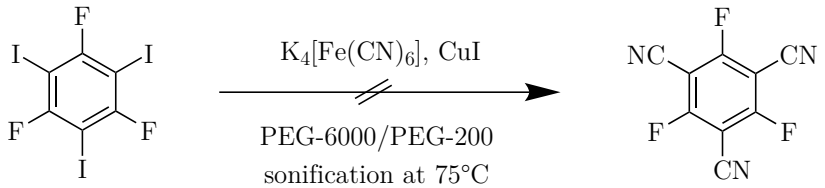

20.00 g of PEG-6000 was slowly melted under argon atmosphere, then 2.04 g (4.0 mmol) of 1,3,5-trifluoro-2,4,6-triiodobenzene, 0.038 g (0.2 mmol) of CuI and 0.88 g (2.4 mmol) of $K_4[Fe(CN)_6]$ were added. The reaction mixture was sonificated at 75 °C. After 20 min. of sonication, 3.0 ml of PEG-200 was added. Then, the mixture was sonicated for 20 min. After the sonication, CH_2Cl_2 was added. The solution was transferred dropwise

into Et_2O. The light grey slurry was kept at -16 °C over night and then filtered. The solvent could not be removed, and no analysis was performed.

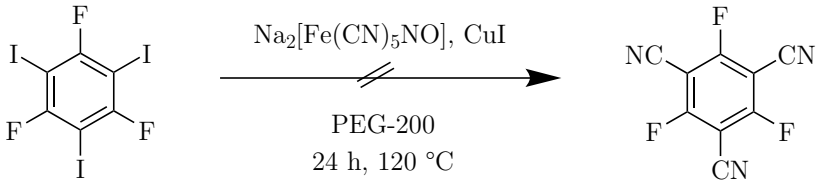

Under argon atmosphere, 0.51 g (1.0 mmol) of 1,3,5-trifluoro-2,4,6-triiodobenzene, 0.089 g (0.3 mmol) of $Na_2[Fe(CN)_5NO] \cdot 2\,H_2O$, 0.080 g (2.0 mmol) of NaOH, 0.019 g (0.1 mmol) of CuI and 2 ml of PEG-200 were heated to 120 °C. After 24 h, the mixture was allowed to cool to r.t. and then extracted with Et_2O. The combined organic layers were dried over $MgSO_4$ and filtrated. The solvent was removed under reduced pressure to obtain a brown oil, which is not the desired product.

LR-GC-MS: m/z / % = 509.70 (M+ $[C_6F_3I_3]$), 382.80 $[C_6F_3I_2^{\cdot}]$, 255.90 $[C_6F_3I^{2\cdot}]$, 126.90 $[I^{\cdot}]$.

Synthesis of 1,3,5-Triiodo-2,4,6-trimethylbenzene

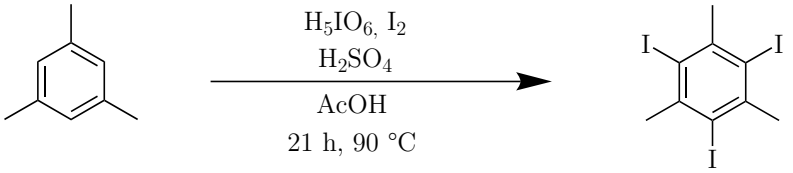

2.00 g (16.6 mol, 1.0 equiv.) of mesitylene, 2.36 g (10.32 mmol, 0.6 equiv.) of H_5IO_6, and 6.46 g (25.46 mmol, 1.5 equiv.) of iodine were dissolved in 17 ml of AcOH and 1 ml of H_2O. Then, 0.92 g (9.38 mmol, 0.6 equiv.) of conc. H_2SO_4 was added dropwise. Subsequently, the mixture was heated to 90 °C and stirred for 21 h. The yellow mixture was cooled to r.t. and NaOH was added until it became almost colourless. The resulting suspension was filtered, washed with H_2O and dried. The pale yellow powder was dissolved in EtOH and precipitated with H_2O. The precipitate was filtered off to obtain 4.47 g (8.97 mmol, 54 %) of the product as a colourless solid (4.47 g, 8.97 mmol, 54 %).

MF	$C_9H_9I_3$
MW	$497.78\,\mathrm{g\,mol^{-1}}$
Yield	4.47 mg (8.97 mmol, 54 %)

^{1}H–NMR	(300 MHz, $CDCl_3$) δ / ppm = 3.01 (s, 3H, H-3).
^{13}C–NMR	(75 MHz, $CDCl_3$) δ / ppm = 144.4 (C–2), 101.3 (C–1), 39.7 (C–3).

Synthesis of Triiodobenzene-1,3,5-tricarboxylic acid via Oxidation

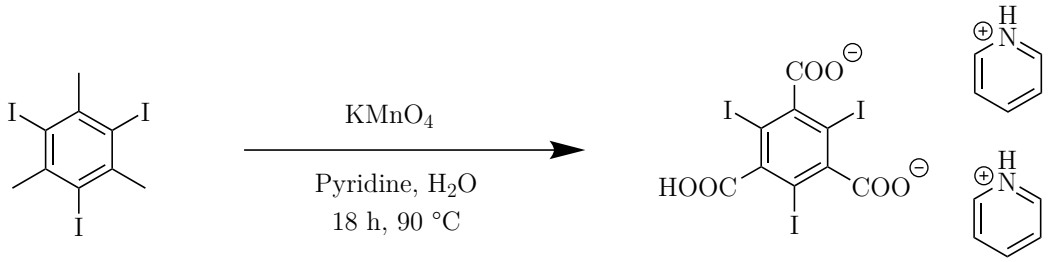

4.40 g (8.3 mmol, 1.0 equiv.) of 1,3,5-Triiodo-2,4,6-trimethylbenzene was suspended in a mixture of 60 ml of pyridine and 22 ml of H_2O. This mixture was heated to 90 °C. 52.80 g (33.4 mmol, 3.8 equiv.) $KMnO_4$ was added in portions over 6 h. After the addition of $KMnO_4$, the mixture was stirred for 18 h at 90 °C. To the hot mixture, EtOH was added. The suspension was filtered and washed with H_2O followed by aq. KOH (5 %). The filtrate was acidified with HCl to pH = 1 and extracted with EtOAc. The combined organic layers were dried over $MgSO_4$ and the solvent was removed under reduced pressure to give 5.98 g of the product as a yellow solid.

x of $H_3 - 3I - BTC \cdot py_x$ could not be determined. As a result, the exact yield could not be determined.

^{1}H–NMR (300 MHz, $CDCl_3$) δ [ppm] = 7.82–7.93 (m, 1H, 2´–H), 8.37 (tt, J = 7.8, 1.7 Hz, 1H, 3´–H), 8.83 (dt, J = 5.0, 1.6 Hz, 2H, 1´–H).

^{13}C–NMR (126 MHz, DMSO – d_6) δ [ppm] = 169.4 (RCOO), 167.8 (RCOO), 148.4 (Cq), 144.0 (C–3‘), 143.9 (C– ‘), 139.3 (Cq), 126.5 (C–2‘), 93.2 (C–I), 88.7 (C–I).

Attempted Synthesis of Triiodobenzene-1,3,5-tricarboxylic acid via Iodination

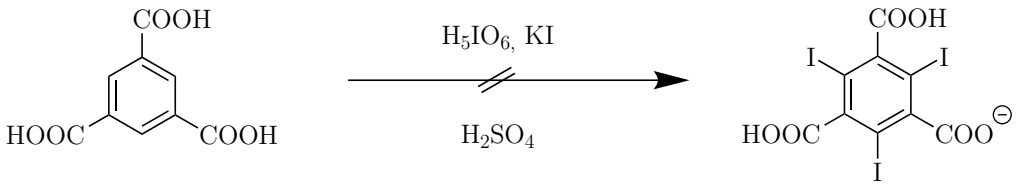

20 ml of conc. H_2SO_4 were cooled to 0 °C. Then, 3.00 g (13.2 mmol, 1.4 equiv.) of H_5IO_6 were added over a period of 1 h. Afterwards, 6.61 g (39.8 mmol, 4.1 equiv.) of KI was added in small portions. Then, 2.03 g (9.67 mmol, 1.0 equiv.) of trimesic acid was slowly added. The reaction mixture was stirred at 40 °C for 4 h and was then allowed to cool down to room temperature. The mixture was poured on approx. 300 ml of ice. When the ice had melted, the precipitated black solid was separated by filtration. Residue and filter were washed with sat. NaOH(aq) in a glass bowl until the residue turned pale yellow. It was separated by filtration, dissolved in hot EtOH, and precipitated with H_2O. The precipitate was again separated by filtration to obtain a colourless solid.
The product could not be dissolved in all solvents, we tried, thus no NMR or GC-MS data were measured.

Synthesis of *N*-Mesitylacetamide

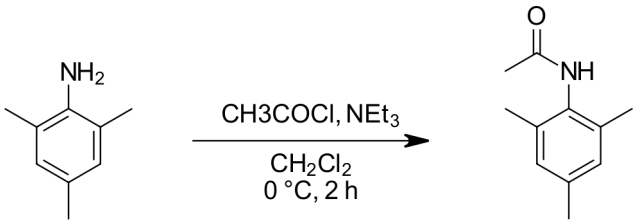

Under an argon atmosphere, 10.5 ml of 2,4,6-trimethylaniline (75 mmol, 1.0 eq.) and 100 ml of dichloromethane were added to a three-necked flask and cooled to 0 °C. Then, 5.64 ml of acetyl chloride (79 mmol, 1.05 eq.) was added dropwise, followed by 11.01 ml of triethylamine (79 mmol, 1.05 eq.). The reaction was monitored by thin-layer chromatography (TLC). After approximately 2 h, no starting material was detectable, and the reaction mixture was filtered. The solid was suspended in water for 30 min, collected by filtration again, and dried overnight under reduced pressure. The crude material was used in further reactions without additional purification.

MF	$C_{11}H_{15}NO$
MW	$177.25\,g\,mol^{-1}$

^{1}H–NMR	(300 MHz, $CDCl_3$) δ / ppm = 6.93 (s, 2H), 2.29 (s, 3H), 2.25 (s, 6H), 1.73 (s, 3H).

Synthesis of 2-Amino-1,3,5-benzenetricarboxylic acid

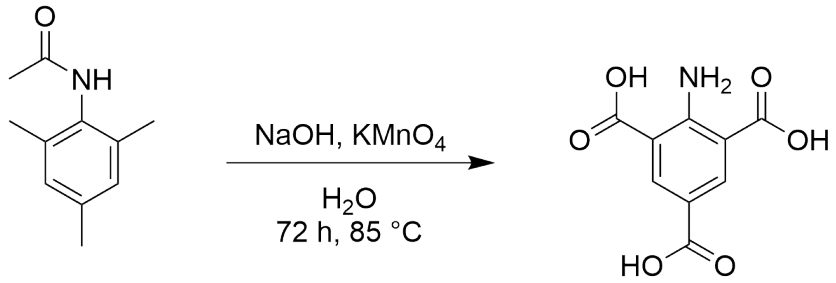

5 g of *N*-mesitylacetamide (28.2 mmol, 1.0 eq.) was added to 165 ml of distilled H_2O and slowly treated with 0.55 g (0.1 g portions) (14 mmol, 0.5 eq.) NaOH. Subsequently, 34 g (215 mmol, 7.8 eq) of $KMnO_4$ was added in 5 g portions over 2 h at room temperature. Once the $KMnO_4$ addition was complete, the reaction was stirred at room temperature for 1 h and then for 72 h at 85 °C. The resulting brown suspension was filtered and washed with 200 ml of hot water. The filtrate was acidified to a pH of 1–2 with 20 ml of concentrated HCl while stirring. The reaction mixture was refluxed overnight at 100 °C. Upon cooling to room temperature, a colourless solid crystallised out. The solid was filtered and washed with 200 ml of ice-cold water, yielding 3.19 g (14.18 mmol, 50 %) of the product.

MF	$C_{11}H_{15}NO$
MW	177.25 g mol^{-1}

^{1}H–NMR	(300 MHz, DMSO – d_6) δ / ppm = 13.19 (s, 3H, –COOH), 8.60 (s, 2H, –NH), 8.56 (s, 2H, H–3).
^{13}C–NMR	(75 MHz, DMSO – d_6) δ / ppm = 169.2 (C–6), 166.7 (C–5), 155.6 (C–2), 138.8 (C–3), 115.70 (C–4), 112.0 (C–1).

Synthesis of of 2-Fluoro-3',5'-dimethyl-[1,1'-biphenyl]-4-aldehyde

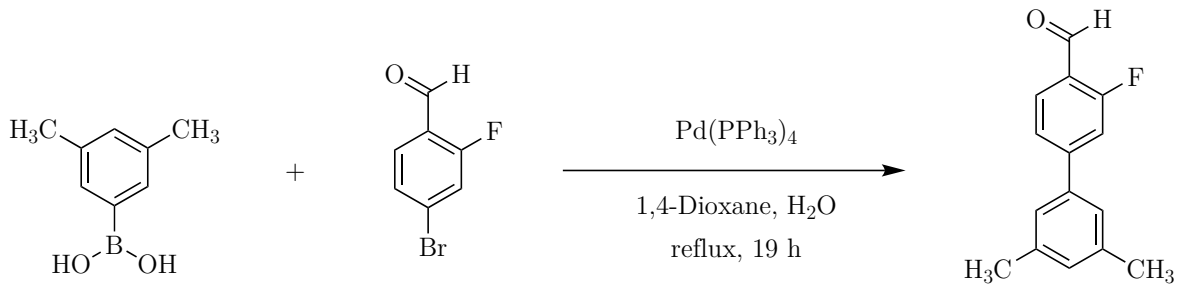

1.93 g (12.87 mmol, 1.4 equiv.) of 3,5-dimethylphenyboronic acid, 2.05 g (8.98 mmol, 1. equiv.) 4-bromo-2-fluorobenzaldehyde and 2.61 g of K_2CO_3 were added to a three-neck flask. The solid mixture was flushed with argon for 30 min. Then 20 ml of H_2O and 50 ml of 1,4-dioxane were added. The reaction mixture was degassed using Ar for 1.5 h before adding 0.31 g (0.20 mmol) of $Pd(PPh_3)_4$. The reaction mixture was refluxed for 19 h, then it was allowed to cool down to r.t. A mixture of H_2O:1,4-dioxane (5:1) was added. The resulting precipitate was filtered and washed with a cooled mixture of H_2O:1,4-dioxane (5:1). After drying under atmospheric conditions, the product was obtained as a colorless powder.

MF	$C_{15}H_{13}FO$
MW	$228.27\,g\,mol^{-1}$
Yield	1.31 g (4.38 mmol, 58 %).

^{1}H–NMR	(300 MHz, $CDCl_3$) δ / ppm = 10.40 (d, 1H), 7.93 (dd, 1H), 7.51 (ddd, 1H), 7.40 (dd, 1H), 7.25 (d, 2H), 7.14 – 7.07 (m, 1H), 2.42 (d, 6H).
^{13}C–NMR	(75 MHz, $CDCl_3$) δ / ppm= 186.97, 186.89, 138.77, 130.72, 128.96, 125.10, 123.31, 123.27, 114.84, 114.55, 67.10.
^{19}F–NMR	(282 MHz, $CDCl_3$) δ / ppm= −121.83 (dd, 1F).

Synthesis of 3'-Fluoro-[1,1'-biphenyl]-3,4',5-tricarboxylic acid

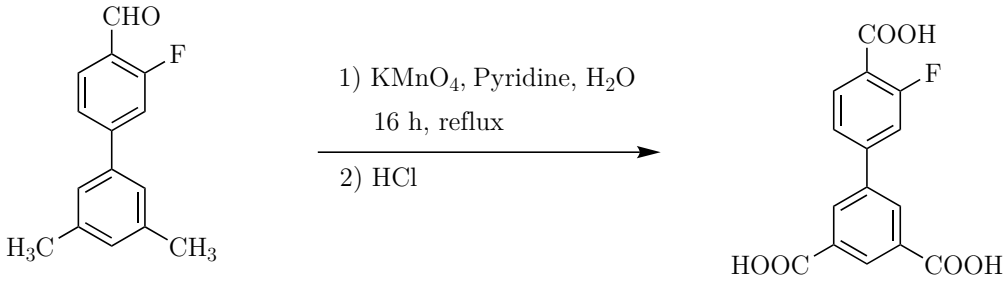

2.15 g (10.04 mmol, 1.0 equiv.) of 3-fluoro-3',5'-dimethyl-[1,1'-biphenyl]-4-aldehyde and 4.78 g (30.25 mmol, 3.2 equiv.) of $KMnO_4$ were dissolved in in 25 ml of H_2O and 75 ml of acetone. The reaction mixture was heated to 72 °C for 24 h. After the mixture had cooled down to r.t., 5.17 g (32.71 mmol, 3.5 equiv.) of $KMnO_4$ was added and refluxed for 24 h. On the next day, the mixture was allowed to cool down to r.t. 15.55 g (98.40 mmol, 10.5 equiv.) of $KMnO_4$ had been added to the mixture before it was heated again to reflux. After 24 h, the mixture was allowed to cool down to r.t. Then was filtered and washed with cold H_2O:acetone (1:3). The filtrate was reduced under pressure and acidified with HCl. The resulting precipitate was filtered, washed with cold H_2O and air dried.

MF	$C_{15}H_9FO_6$
MW	$304.23\,g\,mol^{-1}$
Yield	1.31 g (4.38 mmol, 58 %).

^{1}H–NMR	(300 MHz, DMSO–d_6) δ / ppm = 8.94 (dt, J = 5.1, 1.5 Hz, 4H), 8.61 (tt, J = 7.8, 1.6 Hz, 2H).
^{13}C–NMR	(75 MHz, DMSO–d_6) δ / ppm = 146.54, 142.23, 134.08, 127.73.
^{19}F–NMR	(282 MHz, DMSO–d_6) δ / ppm = – – 109.51 (dd, J = 12.2, 7.9 Hz), –109.66 (dd, J = 12.4, 7.8 Hz), –110.74 (t, J = 6.2 Hz).

6.5 Syntheses of the MOFs and the Coordination Polymers

(a) Teflon Inlay (b) Pressure Vessel (c) screw-cap Glass Vessel (d) Screw Lid Glas

Figure 6.1: Photographs of the reaction vessels.

The reactants and solvents were either placed in a screw-cap glass vessel or a 23 ml Teflon inlay (see Figure 6.1). The Teflon inlay was securely tightened within a pressure vessel (*Parr Instrument Company*). The reaction vessels were then placed in an oven (*Memmert*), where the reaction mixtures were heated to a target temperature, maintained at that temperature for a specified duration, and then gradually cooled to r.t. This heating program was pre-programmed using the *AtmoCONTROL* software by *Memmert*.

Syntheses of the Anionic MOFs

Synthesis of Zn-UoC-7(1F)[1]

50.0 mg (0.19 mmol, 1.0 equiv.) of K(H_2*mF*BTC) and 55.8 mg (0.19 mmol, 1.0 equiv.) of $Zn(NO_3)_2 \cdot 6\,H_2O$ were dissolved in a mixture of 3.0 ml of DMA and 6.0 ml of EtOH in a 23 ml Teflon lined pressure vessel. The mixture was heated to 100 °C within one hour, maintained at 100 °C for 72 h, then cooled down to r.t. within 12 h. The resulting pale yellow crystals were washed several times with DMA:EtOH (1:2) and dried in air.

Synthesis of Zn-UoC-7(2F)[1]

62.5 mg (0.22 mmol, 1.0 equiv.) of K(H_2*dF*BTC) and 65.0 mg (0.22 mmol, 1.0 equiv.) of $Zn(NO_3)_2 \cdot 6\,H_2O$ were dissolved in a mixture of 3.0 ml of DMA and 6.0 ml of EtOH in a 23 ml Teflon lined pressure vessel. The mixture was heated to 95 °C within one hour, maintained at 95 °C for 48 h, and cooled down to r.t. within 48 h. The precipitate was washed several times with DMA:EtOH (1:2) and dried in air leading to pale yellow crystals.

Table 6.2: Variation of Reaction Conditions for the Synthesis of Zn-UoC-7(2F).

Solvent mixture	Volume	$(CH_3)_2NH_2Cl$	$Zn(NO_3)_2 \cdot 6\,H_2O$	K(H_2*dF*BTC)
DMA:EtOH	3 ml:6 ml	–	0.22 mmol	0.22 mmol
DEF:EtOH	3 ml:6 ml	–	0.22 mmol	0.22 mmol
DBF:EtOH	3 ml:6 ml	–	0.22 mmol	0.22 mmol
PC:EtOH	3 ml:6 ml	0.22 mmol	0.22 mmol	0.22 mmol

Synthesis of Co-UoC-7(2F)

62.5 mg (0.22 mmol, 1.0 equiv.) of K(H_2*dF*BTC) and 65.0 mg (0.22 mmol, 1.0 equiv.) of $Co(NO_3)_2 \cdot 6\,H_2O$ were dissolved in a mixture of 3.0 ml of DMA and 6.0 ml of EtOH in a 23 ml Teflon lined pressure vessel. The mixture was heated to 95 °C within one hour, maintained at 95 °C for 48 h, and cooled down to r.t. within 72 h. The precipitate was washed several times with DMA:EtOH (1:2) and dried in air leading to pale yellow crystals.

Synthesis of UoC-13(1F) as crystalline powder

26.6 mg (0.1 mmol, 1.0 equiv) of K(H_2*mF*BTC) and 23.0 mg (0.1 mmol, 1.0 equiv) of $InCl_3$ were mixed with 3.0 ml of DMF in a screw lid glass. The reaction mixture was heated to 110 °C within one hour, the temperature had been held for 24 h before cooled down to r.t. within 12 h. The colourless powder was washed with DMF and dried in air.

Synthesis of the single crystal of UoC-13(1F)

26.6 mg (0.10 mmol, 1.0 equiv) of K(H_2*mF*BTC) and 35.4 mg (0.16 mmol, 1.6 equiv) of $InCl_3$ were mixed with 2.0 ml of DMA and 0.5 ml H_2O in a screw lid glass. The reaction mixture was heated to 100 °C within one hour. This temperature had been held for 48 h before the mixture was cooled down to r.t. within 72 h. The colourless powder was washed with DMF and dried in air.

Synthesis of GaMOF-1(1F)

26.8 mg (0.1 mmol, 1.0 equiv) of K(H_2*mF*BTC) and 17.5 mg (0.1 mmol, 1.0 equiv) of $GaCl_3$ were mixed with 3.0 ml of DMF in a screw lid glass. The reaction mixture was

heated to 100 °C within one hour. 100 °C had been held for 48 h, before the mixture was cooled to r.t. within 72 h. The colourless crystals were washed with DMF and dried in air.

Synthesis of Zn-UoC-5(1F)[4], Zn-UHM-33(1F), $^{2}_{\infty}[Zn_2(BTC)(NO_3)(DMF)_3]$, $^{3}_{\infty}[Zn_3(mF{-}BTC)(DMA)_3]$ and $^{3}_{\infty}[CoZn_2(mF{-}BTC)(DMA)_3]$

A screw-cap glass vessel were loaded with 12.0 mg (0.05 mmol, 1.0 equiv) of K(H_2mFBTC) and 16.0 mg (0.05 mmol, 3.1 equiv) of $Zn(NO_3)_2 \cdot 6\,H_2O$ and 1.0 ml DMA. The reaction mixture was heated to 100 °C within 2 h. This temperature was maintained for 48 h, after which the mixture was cooled down to room temperature over 12 h. The crystals were washed with DMA and dried in air.

Syntheses of M,Zn-UoC-5(1F) and M,Zn-UoC-5(2F) (M = Cu, Zn)

Synthesis of Cu,Zn-UoC-5(1F) as crystalline powder

12.5 mg (0.05 mmol, 1.0 equiv) K(H_2mF-BTC) and 42.0 mg (0.16 mmol, 3.1 equiv) $Zn(NO_3)_2 \cdot 6\,H_2O$ and 15.6 mg (0.05 mmol, 1.0 equiv) $Cu(NO_3)_2 \cdot 3\,H_2O$ were mixed with 1.0 ml DMA in a screw-cap glass vessel. The reaction mixture was heated to 120 °C within 2 h. This temperature was maintained for 48 h, before the mixture was cooled to r.t. within 12 h. The green crystals were washed with DMA and dried in air.

Synthesis of Cu,Zn-UoC-5(2F) as crystalline powder

13.7 mg (0.05 mmol, 1.0 equiv) K(H_2dFBTC) and 46.7 mg (0.16 mmol, 3.1 equiv) $Zn(NO_3)_2 \cdot 6\,H_2O$ and 15.4 mg (0.05 mmol, 1.0 equiv) $Cu(NO_3)_2 \cdot 3\,H_2O$ were mixed with 1.0 ml DMA in a screw-cap glass vessel. The reaction mixture was heated to 120 °C within 2 h. This temperature was maintained for 48 h, before the mixture was cooled to r.t. within 12 h. The green crystals were washed with DMA and dried in air.

Synthesis of Co,Zn-UoC-5(1F) as crystalline powder

13.7 mg (0.05 mmol, 1.0 equiv) K(H_2*mF*BTC) and 46.7 mg (0.16 mmol, 3.1 equiv) $Zn(NO_3)_2 \cdot 6\,H_2O$ and 18.5 mg (0.06 mmol, 1.3 equiv) $Co(NO_3)_2 \cdot 6\,H_2O$ were mixed with 3.0 ml DMA in a screw-cap glass vessel. The reaction mixture was heated to 120 °C within 2 h. This temperature was maintained for 48 h, before the mixture was cooled to r.t. within 24 h. The pink crystals were washed with DMA and dried in air.

Synthesis of Co,Zn-UoC-5(2F) as crystalline powder

13.7 mg (0.05 mmol, 1.0 equiv) K(H_2*dF*BTC) and 46.7 mg (0.16 mmol, 3.1 equiv) $Zn(NO_3)_2 \cdot 6\,H_2O$ and 18.2 mg (0.06 mmol, 1.3 equiv) $Co(NO_3)_2 \cdot 6\,H_2O$ were mixed with 3.0 ml DMA in a screw-cap glass vessel. The reaction mixture was heated to 120 °C within 2 h This temperature was maintained for 48 h, before the mixture was cooled to r.t. within 24 h. The pink crystals were washed with DMA and dried in air.

Synthesis of $^{3}_{\infty}[CoZn_2(mF\text{–}BTC)(DMA)_3]$

13.7 mg (0.05 mmol, 1.0 equiv) of K(H_2mFBTC), 46.7 mg (0.16 mmol, 3.1 equiv) of $Zn(NO_3)_2 \cdot 6\,H_2O$, and 18.5 mg (0.064 mmol, 1.0 equiv) of $Co(NO_3)_2 \cdot 6\,H_2O$ were mixed with 3.0 ml of DMA in a screw-cap glass vessel. The solution was heated to 100 °C within two hours. This temperature was maintained for 48 h, after which the mixture was cooled down to room temperature over 12 h. The pink crystals were washed with DMA and dried in air.

Synthesis of $^{3}_{\infty}[Co_2(mfBTC)(NO_3)(DMA)_3]$

12.0 mg (0.05 mmol, 1.0 equiv) of K(H_2mFBTC) and 16.0 mg (0.05 mmol, 3.1 equiv) of $Zn(NO_3)_2 \cdot 6\,H_2O$ were mixed with 1.0 ml of DMA in a screw-cap glass vessel. The solution was heated to 100 °C within two hours. This temperature was maintained for 48 h, after which the mixture was cooled down to room temperature over 12 h. The colorless crystals were washed with DMA and dried in air.

6.6 Characterisation Methods

Nuclear Magnetic Resonance (NMR) Spectroscopy

Nuclear magnetic resonance spectra presented in this work were measured on a *Bruker Avance II 300*. All ^{1}H-NMR spectra were measured at 300 MHz, ^{13}C-NMR spectra at 75 MHz and ^{19}F-NMR spectra at 282 MHz. The ^{1}H-NMR and ^{13}C-NMR shifts in ppm are given in reference to TMS. The ^{19}F-NMR shifts in ppm are given in reference to $CFCl_3$. The spectra were processed using the program *TopSpin 3.2*[106] by *Bruker* and further

analyzed using the program *MestReNova*[107] by *Mestrelab*. The chemical shifts are given in ppm followed by the multiplicity, the coupling constant (if applicable), the integral, and the assignment. Multiplicities are denoted as s (singlet), d (doublet), t (triplet), q (quartet), and m (multiplet).

Laboratory Powder X-ray Diffraction (PXRD)

Laboratory measurements were carried out on either a *STOE Stadi P* powder diffractometer (Debye-Scherrer geometry, Ge(111) monochromator, Dectris Mythen1K detector), on a *Huber G670* powder diffractometer (Guinier geometry, Ge(111) monochromator, image plate detector) or on a *Rigaku MiniFlex600-C* powder diffractometer (Ni filter, D/teX Ultra detector). Previous to the measurement, all samples were ground. For measurements on the *Rigaku MiniFlex600-C* powder diffractometer, the ground samples were placed on a silicon sample carrier, on which the samples were irradiated with Cu Kα radiation ($\lambda = 1.5418$ Å). PXRD data were collected at RT. Typical recording times were approx. 20 min with a step size of 0.005° (2θ). For measurements on the *STOE Stadi P* powder diffractometer, the ground samples were filled approximately 2 cm high into *Glas W. Müller* glass capillaries (diameter of 0.7 to 1.0 mm). These filled capillaries were closed with pizine. After this preparation, they were adjusted on a goniometer head so that the substance was centered inside the beam. During rotation, the samples were irradiated with Mo Kα_1 ($\lambda = 0.71069$ Å) radiation. Data were collected at RT between 4° and 80.70° in 2θ with steps of 0.01° and a measurement time of 5 s/step. For measurements on the *Huber G670* diffractometer, the ground samples were placed between polymer foil in a flat sample holder. The samples were irradiated with Cu Kα_1 ($\lambda = 1.5406$ Å) radiation. All PXRD data were processed and analyzed with the *WinXPow* program package.[108] Theoretical patterns were generated from the *Crystallographic Information Files* of the corresponding substances with *WinXPow*.[108]

High Resolution Synchrotron Powder Diffraction

High resolution synchrotron powder diffraction data were recorded at BL9 at the *Dortmund Electron Accelerator* (*DELTA*). Data were collected at r. t. with a wavelength of 0.49594 Å using a *PILATUS100K* detector between 2.8° and 25° in 2θ with steps of 0.01° and 10 s integration time per data point. For the measurements, the respective samples were ground and filled approximately 2 cm high into *Hilgenberg* glass capillaries (diameter of 0.7 - 1.0 mm). These filled capillaries were closed airtight with pizine and adjusted horizontally on a goniometer head so that the substance was centered inside the beam.

Single Crystal X-ray Structure Analysis

Single crystals were prepared selected with the aid of a polarization filter of a light microscope. The crystals were taken directly from the mother liquor and mounted on a goniometer using silicone oil on a nylon loop. The crystals were cooled depending on the sensitivity of the compound to either 100 K, 200 K or 280 K before irradiation.
Single-crystal data of UoC-7(1F) and UoC-7(2F) was collected at beamline P24.1 of the PETRA III facility at the German Electron Synchrotron (DESY), Hamburg, Germany. For each measurement, one single crystal was positioned in the nitrogen gas stream (100.0(2) K) of the single crystal diffractometer (Huber 4-circle Kappa, beamline P24.1) and intensity data was collected. The collected intensity data for UoC-7(1F) was reduced, and unit cell refinements were carried out using the XDS software.[109]
Absorption correction was applied to the respective reflection data by SADABS[110] (Zn-UoC-7(1F)) or CrysAlis^{PRO} (Zn-UoC-7(2F)).
To determine the space group and to create an initial model, the program SHELXT[111] was used. The structural model was refined by least squares methods using SHELXL-18.[99]

All other SCXRD measurements has been performed on a *Bruker D8 VENTURE KAPPA* diffractometer with a microfocus sealed tube using a multilayer mirror as monochromator and a *Bruker PHOTON III* detector. Mo Kα(λ = 0.71069 Å) radiation was used as

the X-ray source. The intensity data were collected and the images processed using *APEX4*.[112] The integration was done with *SAINT*[113] and a multi-scan absorption correction using *SADABS*[110] was applied.
The quality of the resulting structure may be assessed from the following metrics:

$$GooF = \sqrt{\frac{\sum_{hkl} \omega ||F_o^2| - |F_c^2||^2}{m - n}} \tag{6.1}$$

$$R_{int} = \frac{\sum_{hkl} |F_o^2 - F_{o,\mathrm{mean}}^2|}{\sum_{hkl} F_o^2} \tag{6.2}$$

$$R_1 = \frac{\sum_{hkl} ||F_o| - |F_c||}{\sum_{hkl} |F_o|} \tag{6.3}$$

$$wR_2 = \sqrt{\frac{\sum_{hkl} w(F_o^2 - F_c^2)^2}{\sum_{hkl} w(F_o^2)^2}} \tag{6.4}$$

with

m	=	number of measured reflexes,
n	=	number of refined reflexes,
F_o	=	observed structural factors,
F_c	=	calculated structural factors,
w	=	weighting factor.

Continuous Shape Measures (CShM)

All *CShM* values were calculated with the *Shape* program package.[92] The divergence from ideal regular polyhedra are calculated by entering the coordinates of the central

atom as well as the atoms of the first coordination sphere, the *CShM* values (continuous shape measure) for the relevant polyhedron types are calculated using the equation below.

$$CShM_Q(P) = \min\left[\frac{\sum_{i=1}^{N}|\vec{q}_i - \vec{p}_i|^2}{\sum_{i=1}^{N}|\vec{q}_i - \vec{q}_0|^2}\right] \cdot 100 \tag{6.5}$$

mit

with

Q	=	observed coordination polyhedron,
P	=	reference polyhedron,
$\vec{q}_0$	=	centroid of Q,
$\vec{q}_i$	=	position of atom i,
$\vec{p}_i$	=	position of polyhedral vertex i.

The magnitude of the value ranges from 0 to 100 may be used to asses the similarity of the observed polyhedron to an ideal one with an equal number of vertexes. Values close to zero correspond to nearly ideal polyhedra. All polyhedra with values above 3 may not be described by their reference polyhedron.

Hirshfeld Surface Analysis

Hirshfeld surfaces were generated using the *CrystalExplorer* program package using the structure data of the here elucidated structures. Hydrogen bond lengths are adjusted by the *CrystalExplorer* program package to C–H = 1.083 Å, N–H = 1.009 Å and O–H = 0.983 Å. All surfaces were generated on the *Very High* setting for the grid size. In this work, the basis sets of *Koga et al.*[114] were used for all calculations, which is the recommended default in the *CrystalExplorer* program package.

X-ray Photoelectron Spectroscopy (XPS)

For XPS measurements, the respective samples were ground and placed on adhesive copper foil.
XPS spectra were recorded using an ESCA M-Probe from Surface Science Instruments equipped with a monochromatic Al Kα X-ray source (1486.6 eV, λ = 8.33 Å) in a range of 0-1000 eV in ultra-high vacuum of 10^{-9} mbar.
Survey spectra were recorded with a detector pass energy of 158.3 eV (0.5 eV step size, 125 ms dwell time, averaged over seven scans) and high-resolution spectra with 55.2 eV (0.05 eV, step size, 175 ms dwell time, averaged over 25 scans).
The spectral calibration was achieved by referencing the main C 1s component to the adventitious carbon signal at 284.8 eV. For data processing, the *CasaXPS* software from *Casa Software Ltd.* was used to quantify the signals using the integrated peak areas and the corresponding Scofield relative sensitivity factors. Background corrections were applied using a Shirley line shape. For peak fitting of the C=C bonds, an asymmetric line shape (LA(1,2,0)) was employed, while all other peaks were fitted with a symmetric GL(30) line shape.

Elemental Analysis (CHNS)

Elemental analysis of carbon, hydrogen and nitrogen was carried out with a *HEKAtech GmbH EuroEA 3000* analyser. Approximately 2 mg of each sample was filled with V_2O_5 into a tin cartridge under an argon atmosphere. For each sample, three measurements were carried out, from which a mean value was calculated.

Differential Scanning Calorimetry/Thermogravimetry (DSC/TGA)

DSC/TGA measurements were carried out on a *METTLER TOLEDO StarR DSC1* coupled with a *TGA/DSC1* (*Star System*). 1-6 mg of the substance was weighted in an Al_2O_3 crucible. The measurements were performed under argon flow (40 ml/min). The samples were initally heated to 30 °C, where the temperature was held for 10 min, then they were heated to 1000 °C with a heating rate of 10 °C/min. Evaluation of the data was done with the *STARe* program package.

Differential Scanning Calorimetry/Thermogravimetry/Mass (DSC/TGA/MS)

DSC/TGA/MS analyses of the samples were performed on a thermal analyser *STA 409 (Netzsch)* coupled with a quadrupole mass spectrometer (*QMS 421, BALZERS*). 1-6 mg of the samples were weighted in Al_2O_3 crucibles under ambient conditions. The measurements were performed under argon flow (80 ml/min). Mass analysis was carried out in a scanning mode with predefined *m/z* values. Collected data was processed by the program *Proteus version 6.1.* For graphical depiction of the results *OriginPro 2021b* was used.[115]

Gas Chromatography with Mass Spectrometry (GC-MS)

Strongly diluted solutions of the GC-MS samples were injected into *HP 6890 Series GC-System* coupled with a 5973 Mass Selective Detector, both by Hewlett Packard using H_2 as carrier gas.

Sorption Measurements

N_2 and CO_2 sorption measurements were conducted using an *Autosorb1-MP* device from *Quantachrome*. The N_2 measurements were performed at a temperature of 77 K, while the CO_2 measurements took place at temperatures of 293 K or 273 K. The purity of the N_2, CO_2, and He gases used was 99.999 %. Prior to measurement, the samples were heated under high vacuum conditions (1×10^{-7} mbar). Data analysis was carried out using the *AS1win* software.[116]

The determination of the specific surface areas was based on the N2 gas sorption measurements using the multipoint BET method, which is founded on the model developed by *Brunauer*, *Emmett*, and *Teller* (BET model).[117] The Brunauer–Emmett–Teller (BET) surface area was calculated based on the pressure region p/p0 = 0.0005 - 0.03.

The calculation of the pore size distribution and pore volume was carried out using the methods of non-local density functional theory (NLDFT) and quenched solid density functional theory (QSDFT), integrated into the software *Quantachrome AS1win*.[116] The method with the lowest fitting error was selected. Results with a fitting error of up to 5 % are considered by the equipment manufacturer *Quantachrome* to provide an adequate description of the pore size distribution.

Bibliography

[1] S. Wenzel, A. E. L. Cammiade, R. K. Christoffels, S. S. Sebastian, T. Mattick, U. Ruschewitz, *Chemistry – A European Journal* **2024**, *30*, DOI 10.1002/chem.202400445.

[2] J. A. Mason, K. Sumida, Z. R. Herm, R. Krishna, J. R. Long, *Energy & Environmental Science* **2011**, *4*, 3030.

[3] A. E. L. Cammiade, *Bachelorarbeit*, **2018**.

[4] S. Wenzel, *Master thesis*, **2019**.

[5] W. Westendorf, *Erwachen der Heilkunst: Die Medizin im Alten Ägypten*, Artemis und Winkler, **1992**.

[6] H. von Deines, H. Grapow, W. Westendorf, *Grundriss der Medizin der alten Ägypter*, Akademie-Verlag, **1958**.

[7] C. W. Scheele, *Chemische Abhandlung von der Luft und dem Feuer*, Magn. Swederus, **1777**.

[8] F. Fontana, *Memorie Mat. Soc. Ital. Sci* **1777**, *679*.

[9] E. Harris, *Industrial & Engineering Chemistry* **1942**, *34*, 1057–1060.

[10] C. J. Rhodes, *Annual Reports Section "C" (Physical Chemistry)* **2007**, *103*, 287.

[11] C. J. Rhodes, *Science Progress* **2010**, *93*, 223–284.

[12] H. Li, M. Eddaoudi, M. O'Keeffe, O. M. Yaghi, *Nature* **1999**, *402*, 276.

[13] S. S. Y. Chui, S. M. F. Lo, J. P. H. Charmant, A. G. Orpen, I. D. Williams, *Science* **1999**, *283*, 1148–1150.

[14] P. Horcajada, T. Chalati, C. Serre, B. Gillet, C. Sebrie, T. Baati, J. F. Eubank, D. Heurtaux, P. Clayette, C. Kreuz, J.-S. Chang, Y. K. Hwang, V. Marsaud, P.-N. Bories, L. Cynober, S. Gil, G. Férey, P. Couvreur, R. Gref, *Nature Materials* **2009**, *9*, 172–178.

[15] P. Horcajada, C. Serre, M. Vallet-Regí, M. Sebban, F. Taulelle, G. Férey, *Angewandte Chemie* **2006**, *118*, 6120–6124.

[16] C. Yang, X. Wang, M. A. Omary, *Journal of the American Chemical Society* **2007**, *129*, 15454–15455.

[17] P. Pachfule, Y. Chen, S. C. Sahoo, J. Jiang, R. Banerjee, *Chemistry of Materials* **2011**, *23*, 2908–2916.

[18] P. Pachfule, Y. Chen, J. Jiang, R. Banerjee, *Chemistry – A European Journal* **2011**, *18*, 688–694.

[19] S. R. Batten, N. R. Champness, X.-M. Chen, J. Garcia-Martinez, S. Kitagawa, L. Öhrström, M. O'Keeffe, M. P. Suh, J. Reedijk, *CrystEngComm* **2012**, *14*, 3001.

[20] S. R. Batten, N. R. Champness, X.-M. Chen, J. Garcia-Martinez, S. Kitagawa, L. Öhrström, M. O'Keeffe, M. Paik Suh, J. Reedijk, *Pure and Applied Chemistry* **2013**, *85*, 1715–1724.

[21] A. F. Wells, *Acta Crystallographica* **1956**, *9*, 23–28.

[22] D. Banerjee, S. J. Kim, H. Wu, W. Xu, L. A. Borkowski, J. Li, J. B. Parise, *Inorganic Chemistry* **2010**, *50*, 208–212.

[23] M. J. Kalmutzki, N. Hanikel, O. M. Yaghi, *Science Advances* **2018**, *4*, DOI `10.1126/sciadv.aat9180`.

[24] M. O'Keeffe, O. M. Yaghi, *Chemical Reviews* **2011**, *112*, 675–702.

[25] O. M. Yaghi, Q. Li, *MRS Bulletin* **2009**, *34*, 682–690.

[26] M. O'Keeffe, M. A. Peskov, S. J. Ramsden, O. M. Yaghi, *Accounts of Chemical Research* **2008**, *41*, 1782–1789.

[27] O. Delgado-Friedrichs, M. O'Keeffe, O. M. Yaghi, *Acta Crystallographica Section A Foundations of Crystallography* **2006**, *62*, 350–355.

[28] O. Delgado-Friedrichs, M. O'Keeffe, O. M. Yaghi, *Phys. Chem. Chem. Phys.* **2007**, *9*, 1035–1043.

[29] N. W. Ockwig, O. Delgado-Friedrichs, M. O'Keeffe, O. M. Yaghi, *Accounts of Chemical Research* **2005**, *38*, 176–182.

[30] O. Yaghi, M. O'Keeffe, M. Kanatzidis, *Journal of Solid State Chemistry* **2000**, *152*, 1–2.

[31] M. Eddaoudi, D. B. Moler, H. Li, B. Chen, T. M. Reineke, M. O'Keeffe, O. M. Yaghi, *Accounts of Chemical Research* **2001**, *34*, 319–330.

[32] O. M. Yaghi, M. O'Keeffe, N. W. Ockwig, H. K. Chae, M. Eddaoudi, J. Kim, *Nature* **2003**, *423*, 705–714.

[33] A. Schoedel, A. J. Cairns, Y. Belmabkhout, L. Wojtas, M. Mohamed, Z. Zhang, D. M. Proserpio, M. Eddaoudi, M. J. Zaworotko, *Angewandte Chemie* **2013**, *125*, 2974–2977.

[34] S. K. Elsaidi, M. H. Mohamed, L. Wojtas, A. J. Cairns, M. Eddaoudi, M. J. Zaworotko, *Chemical Communications* **2013**, *49*, 8154.

[35] A. Schoedel, L. Wojtas, S. P. Kelley, R. D. Rogers, M. Eddaoudi, M. J. Zaworotko, *Angewandte Chemie International Edition* **2011**, *50*, 11421–11424.

[36] F. Nouar, J. F. Eubank, T. Bousquet, L. Wojtas, M. J. Zaworotko, M. Eddaoudi, *Journal of the American Chemical Society* **2008**, *130*, 1833–1835.

[37] A. J. Cairns, J. A. Perman, L. Wojtas, V. C. Kravtsov, M. H. Alkordi, M. Eddaoudi, M. J. Zaworotko, *Journal of the American Chemical Society* **2008**, *130*, 1560–1561.

[38] M. Eddaoudi, J. Kim, N. Rosi, D. Vodak, J. Wachter, M. O'Keeffe, O. M. Yaghi, *Science* **2002**, *295*, 469–472.

[39] M. Eddaoudi, J. Kim, M. O'Keeffe, O. M. Yaghi, *Journal of the American Chemical Society* **2001**, *124*, 376–377.

[40] Z. Chen, Ł. J. Weseliński, K. Adil, Y. Belmabkhout, A. Shkurenko, H. Jiang, P. M. Bhatt, V. Guillerm, E. Dauzon, D.-X. Xue, M. O'Keeffe, M. Eddaoudi, *Journal of the American Chemical Society* **2017**, *139*, 3265–3274.

[41] O. K. Farha, I. Eryazici, N. C. Jeong, B. G. Hauser, C. E. Wilmer, A. A. Sarjeant, R. Q. Snurr, S. T. Nguyen, A. Ö. Yazaydin, J. T. Hupp, *J. Am. Chem. Soc.* **2012**, *134*, 15016–15021.

[42] I. M. Hönicke, I. Senkovska, V. Bon, I. A. Baburin, N. Bönisch, S. Raschke, J. D. Evans, S. Kaskel, *Angewandte Chemie International Edition* **2018**, *57*, 13780–13783.

[43] H. Deng, S. Grunder, K. E. Cordova, C. Valente, H. Furukawa, M. Hmadeh, F. Gándara, A. C. Whalley, Z. Liu, S. Asahina, H. Kazumori, M. O'Keeffe, O. Terasaki, J. F. Stoddart, O. M. Yaghi, *Science* **2012**, *336*, 1018–1023.

[44] S. Kitagawa, S.-i. Noro, T. Nakamura, *Chem. Commun.* **2006**, 701–707.

[45] G. Avci, C. Altintas, S. Keskin, *The Journal of Physical Chemistry C* **2021**, *125*, 17311–17322.

[46] R. A. Fischer, C. Wöll, *Angewandte Chemie International Edition* **2008**, *47*, 8164–8168.

[47] C. Serre, *Angewandte Chemie International Edition* **2012**, *51*, 6048–6050.

[48] D.-S. Zhang, Z. Chang, Y.-F. Li, Z.-Y. Jiang, Z.-H. Xuan, Y.-H. Zhang, J.-R. Li, Q. Chen, T.-L. Hu, X.-H. Bu, *Sci. Rep.* **2013**, *3*, 3312.

[49] Z. Hulvey, E. H. L. Falcao, J. Eckert, A. K. Cheetham, *Journal of Materials Chemistry* **2009**, *19*, 4307–4309.

[50] L. Zhang, Q. Wang, Y.-C. Liu, *J Phys Chem B* **2007**, *111*, 4291–4295.

[51] P. Z. Moghadam, J. F. Ivy, R. K. Arvapally, A. M. dos Santos, J. C. Pearson, L. Zhang, E. Tylianakis, P. Ghosh, I. W. H. Oswald, U. Kaipa, X. Wang, A. K. Wilson, R. Q. Snurr, M. A. Omary, *Chemical Science* **2017**, *8*, 3989–4000.

[52] K. Peikert, F. Hoffmann, M. Fröba, *CrystEngComm* **2015**, *17*, 353–360.

[53] H. Chun, D. N. Dybtsev, H. Kim, K. Kim, *Chemistry – A European Journal* **2005**, *11*, 3521–3529.

[54] Z. Hu, B. J. Deibert, J. Li, *Chemical Society Reviews* **2014**, *43*, 5815–5840.

[55] D. Smets, U. Ruschewitz, *Zeitschrift für Anorganische und Allgemeine Chemie* **2020**, *646*, 1157–1167.

[56] J. Krautwurst, D. Smets, R. Lamann, U. Ruschewitz, *Inorg. Chem.* **2019**, *58*, 8622–8632.

[57] C. R. Groom, I. J. Bruno, M. P. Lightfoot, S. C. Ward, *Acta Crystallographica Section B Structural Science Crystal Engineering and Materials* **2016**, *72*, 171–179.

[58] A. Karmakar, A. V. Desai, S. K. Ghosh, *Coordination Chemistry Reviews* **2016**, *307*, 313–341.

[59] S.-N. Zhao, Y. Zhang, S.-Y. Song, H.-J. Zhang, *Coordination Chemistry Reviews* **2019**, *398*, 113007.

[60] A. D. Burrows, K. Cassar, R. M. W. Friend, M. F. Mahon, S. P. Rigby, J. E. Warren, *CrystEngComm* **2005**, *7*, 548.

[61] M. J. Manos, E. E. Moushi, G. S. Papaefstathiou, A. J. Tasiopoulos, *Crystal Growth & Design* **2012**, *12*, 5471–5480.

[62] Q. Zhai, Q. Lin, T. Wu, S.-T. Zheng, X. Bu, P. Feng, *Dalton Transactions* **2012**, *41*, 2866.

[63] Y.-X. Tan, Y.-P. He, J. Zhang, *Chemistry of Materials* **2012**, *24*, 4711–4716.

[64] D. F. Sava, V. C. Kravtsov, F. Nouar, L. Wojtas, J. F. Eubank, M. Eddaoudi, *Journal of the American Chemical Society* **2008**, *130*, 3768–3770.

[65] F. Nouar, J. Eckert, J. F. Eubank, P. Forster, M. Eddaoudi, *Journal of the American Chemical Society* **2009**, *131*, 2864–2870.

[66] A. L. Spek, *Acta Crystallographica Section C Structural Chemistry* **2015**, *71*, 9–18.

[67] H. He, L. Hashemi, M.-L. Hu, A. Morsali, *Coordination Chemistry Reviews* **2018**, *376*, 319–347.

[68] P. Kumar, A. Pournara, K.-H. Kim, V. Bansal, S. Rapti, M. J. Manos, *Progress in Materials Science* **2017**, *86*, 25–74.

[69] Y. Noori, K. Akhbari, *RSC Advances* **2017**, *7*, 1782–1808.

[70] B. Parmar, K. K. Bisht, G. Rajput, E. Suresh, *Dalton Transactions* **2021**, *50*, 3083–3108.

[71] S. Dutta, Y. D. More, S. Fajal, W. Mandal, G. K. Dam, S. K. Ghosh, *Chemical Communications* **2022**, *58*, 13676–13698.

[72] R. Christoffels, C. B. (Stastny), J. P. Weber, L. Körtgen, C. Tobeck, M. Wilhelm, S. Mathur, J.-M. Neudörfl, M. S. Z. Farid, M. Maslo, E. Strub, U. Ruschewitz, *Crystal Growth & Design* **2021**, *22*, 681–692.

[73] D. W. Lee, V. Jo, K. M. Ok, *Journal of Solid State Chemistry* **2012**, *194*, 369–374.

[74] Z. Zhang, M. J. Zaworotko, *Chem. Soc. Rev.* **2014**, *43*, 5444–5455.

[75] L. Ding, A. O. Yazaydin, *Microporous and Mesoporous Materials* **2013**, *182*, 185–190.

[76] H. Furukawa, N. Ko, Y. B. Go, N. Aratani, S. B. Choi, E. Choi, A. Ö. Yazaydin, R. Q. Snurr, M. O'Keeffe, J. Kim, O. M. Yaghi, *Science* **2010**, *329*, 424–428.

[77] M. Thommes, K. Kaneko, A. V. Neimark, J. P. Olivier, F. Rodriguez-Reinoso, J. Rouquerol, K. S. Sing, *Pure and Applied Chemistry* **2015**, *87*, 1051–1069.

[78] M. Peplow, *Nature* **2015**, *520*, 148–150.

[79] Z. Chen, M. C. Wasson, R. J. Drout, L. Robison, K. B. Idrees, J. G. Knapp, F. A. Son, X. Zhang, W. Hierse, C. Kühn, S. Marx, B. Hernandez, O. K. Farha, *Faraday Discussions* **2021**, *225*, 9–69.

[80] S. Gökpinar, S.-J. Ernst, E. Hastürk, M. Möllers, I. El Aita, R. Wiedey, N. Tannert, S. Nießing, S. Abdpour, A. Schmitz, J. Quodbach, G. Füldner, S. K. Henninger, C. Janiak, *Industrial and Engineering Chemistry Research* **2019**, *58*, 21493–21503.

[81] S.-F. Li, L. Hu, R.-L. Tang, Y. Ma, F.-F. Mao, J. Zheng, X.-D. Zhang, D. Yan, *Inorganic Chemistry* **2022**, *61*, 14880–14886.

[82] J. Krautwurst, R. Lamann, U. Ruschewitz, *Zeitschrift für anorganische und allgemeine Chemie* **2017**, *643*, 1397–1405.

[83] J. Krautwurst, *Dissertation*, Universität zu Köln, **2017**.

[84] R. Lamann, *Dissertation*, Universität zu Köln, **2012**.

[85] H. H. Wenk, W. Sander, *European Journal of Organic Chemistry* **2002**, *2002*, 3927–3935.

[86] G. Finger, F. Reed, J. Finnerty, *Journal of the American Chemical Society* **1951**, *73*, 153–155.

[87] C.-H. Liu, Q.-L. Guan, X.-D. Yang, F.-Y. Bai, L.-X. Sun, Y.-H. Xing, *Inorganic Chemistry* **2020**, *59*, 8081–8098.

[88] H. N. Rubin, M. M. Reynolds, *Inorganic Chemistry* **2017**, *56*, 5266–5274.

[89] T.-H. Park, K. A. Cychosz, A. G. Wong-Foy, A. Dailly, A. J. Matzger, *Chem. Commun.* **2011**, *47*, 1452–1454.

[90] V. A. Blatov, A. P. Shevchenko, D. M. Proserpio, *Crystal Growth & Design* **2014**, *14*, 3576–3586.

[91] N. Li, Z. Chang, H. Huang, R. Feng, W.-W. He, M. Zhong, D. G. Madden, M. J. Zaworotko, X.-H. Bu, *Small* **2019**, *15*, DOI `10.1002/smll.201900426`.

[92] M. Llunell, D. Casanova, J. Cirera, P. Alemany, S. Alvarez, *University of Barcelona: Barcelona Spain* **2013**.

[93] A. L. Spek, *Journal of Applied Crystallography* **2003**, *36*, 7–13.

[94] T. Cottineau, M. Richard-Plouet, J.-Y. Mevellec, L. Brohan, *The Journal of Physical Chemistry C* **2011**, *115*, 12269–12274.

[95] A. L. Spek, *Structure validation in chemical crystallography*, *Vol. 65*, International Union of Crystallography, **2009**, pp. 148–155.

[96] P. Nugent, Y. Belmabkhout, S. D. Burd, A. J. Cairns, R. Luebke, K. Forrest, T. Pham, S. Ma, B. Space, L. Wojtas, M. Eddaoudi, M. J. Zaworotko, *Nature* **2013**, *495*, 80–84.

[97] A. Nuhnen, C. Janiak, *Dalton Transactions* **2020**, *49*, 10295–10307.

[98] P. Jurzick, *Bachelorarbeit*, **2018**.

[99] G. M. Sheldrick, **1997**.

[100] W. Massa, *Kristallstrukturbestimmung*, *Vol. 3*, Springer, **2007**.

[101] S.-J. Liu, C. Cao, F. Yang, M.-H. Yu, S.-L. Yao, T.-F. Zheng, W.-W. He, H.-X. Zhao, T.-L. Hu, X.-H. Bu, *Crystal Growth & Design* **2016**, *16*, 6776–6780.

[102] M. Oh, L. Rajput, D. Kim, D. Moon, M. S. Lah, *Inorganic Chemistry* **2013**, *52*, 3891–3899.

[103] M. Cullmann, *Bachelorarbeit*, **2018**.

[104] R. D. Shannon, *Acta Crystallographica Section A* **1976**, *32*, 751–767.

[105] W. Armarego, *Purification of Laboratory Chemicals: Part 2 Inorganic Chemicals, Catalysts, Biochemicals, Physiologically Active Chemicals, Nanomaterials*, Elsevier Science, **2022**.

[106] Bruker, *Top Spin Version 4.1.1.* **2020**.

[107] V. 6.-5. MestReNova, *Mestrelab Santiago de Compostela* **2009**.

[108] S. WinXpow, version 3.12, G. Cie GmbH, Darmstadt, **2010**.

[109] W. Kabsch, *Acta Crystallographica Section D Biological Crystallography* **2010**, *66*, 125–132.

[110] G. Sheldrick, *Google Scholar There is no corresponding record for this reference* **1995**.

[111] G. M. Sheldrick, *Acta Crystallogr* **2015**, *71*, 3–8.

[112] A. Bruker, *Bruker AXS Inc.* **2002**.

[113] Bruker AXS Inc., *SAINT*, Madison Wisconsin USA, **2016**.

[114] T. Koga, K. Kanayama, T. Watanabe, T. Imai, A. J. Thakkar, *Theoretical Chemistry Accounts: Theory Computation and Modeling (Theoretica Chimica Acta)* **2000**, *104*, 411–413.

[115] O. V. 2021b, *OriginLab Corporation* **2021**.

[116] AS1Win, *Version 2.11, Quantachrome, Odelzhausen*, **2009**.

[117] S. Brunauer, P. H. Emmett, E. Teller, *Journal of the American Chemical Society* **1938**, *60*, 309–319.

7 Appendix

NMR Spectra

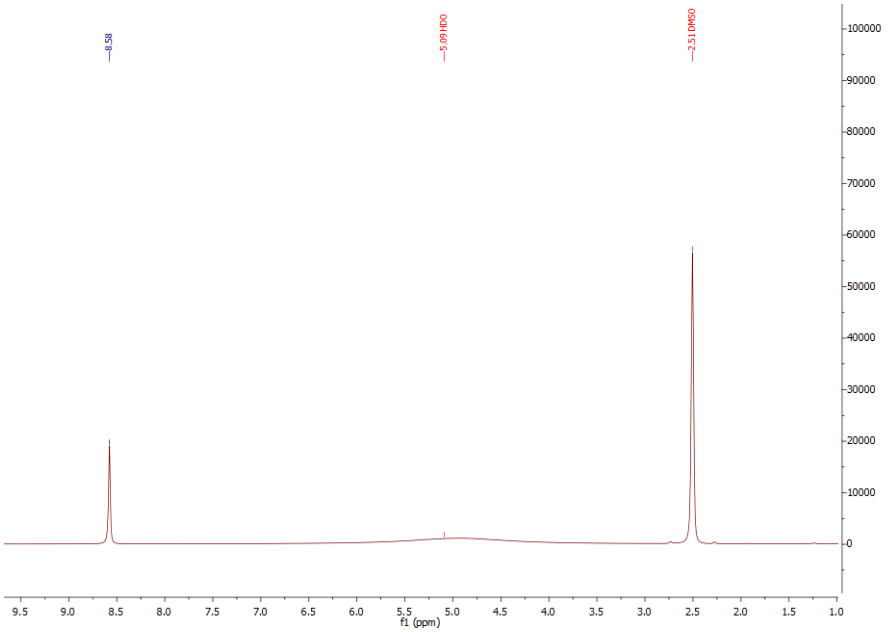

Figure 7.1: ^{1}H–NMR spectrum of [K(H_2BTC)] in DMSO.

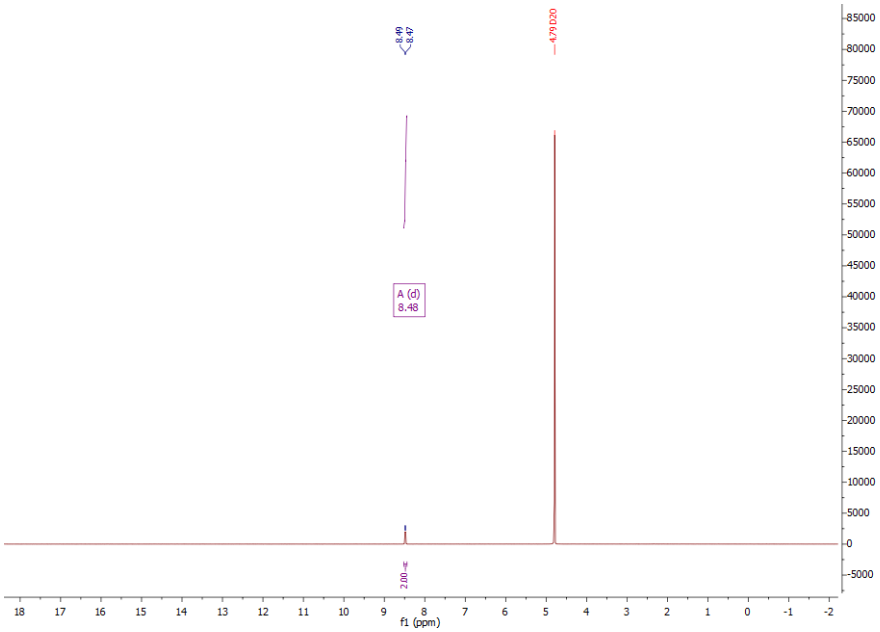

Figure 7.2: ^{1}H–NMR spectrum of [K(H_2*mF*-BTC)] in D_2O.

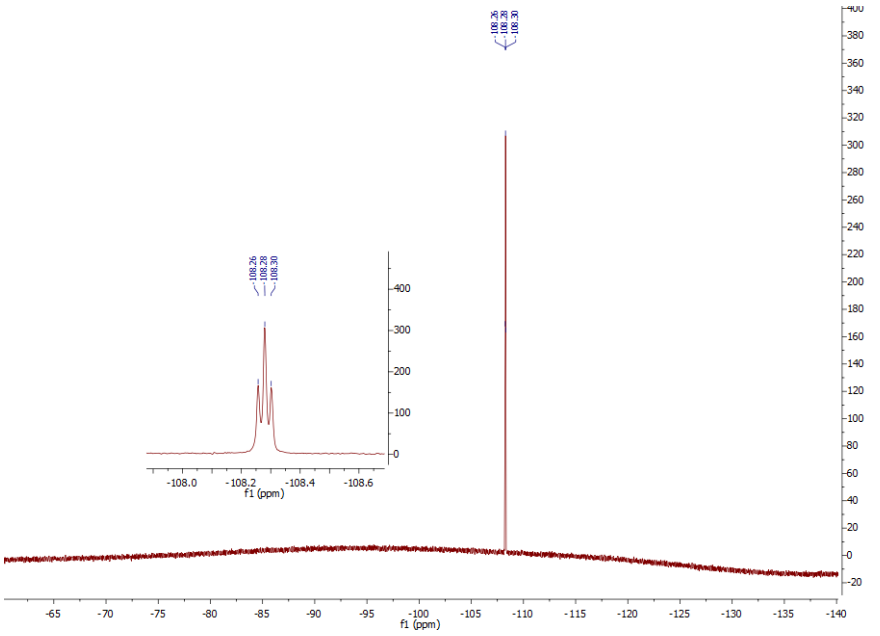

Figure 7.3: ^{19}F–NMR spectrum of [K(H_2*mF*-BTC)] in D_2O.

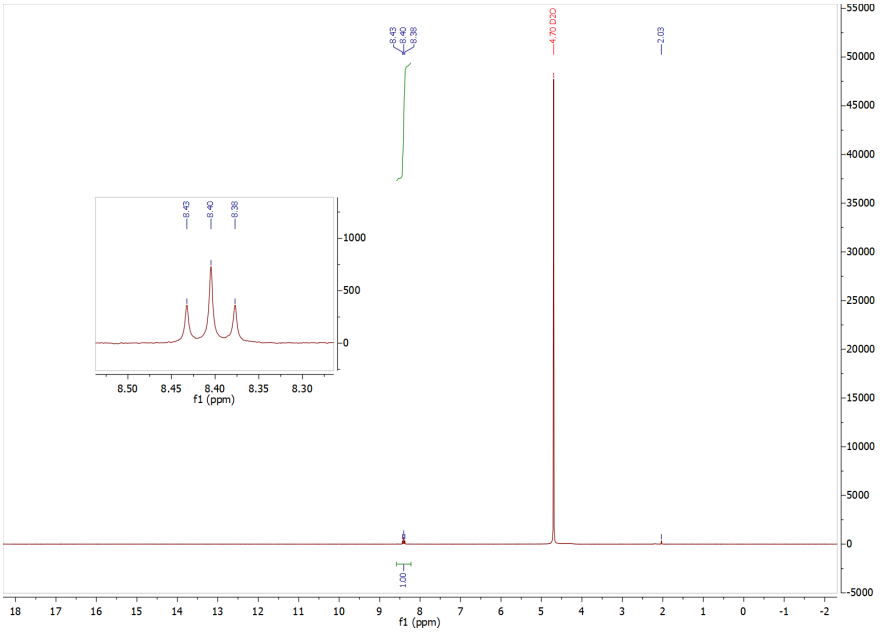

Figure 7.4: ^{1}H–NMR spectrum of [K(H_2*dF*-BTC)] in D_2O.

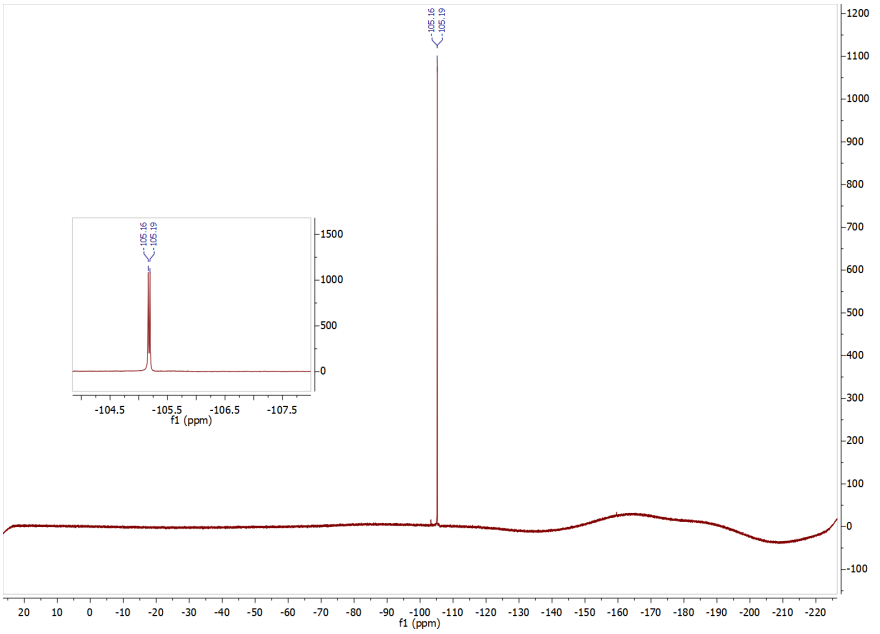

Figure 7.5: ^{19}F–NMR spectrum of [K(H_2*dF*-BTC)] in D_2O.

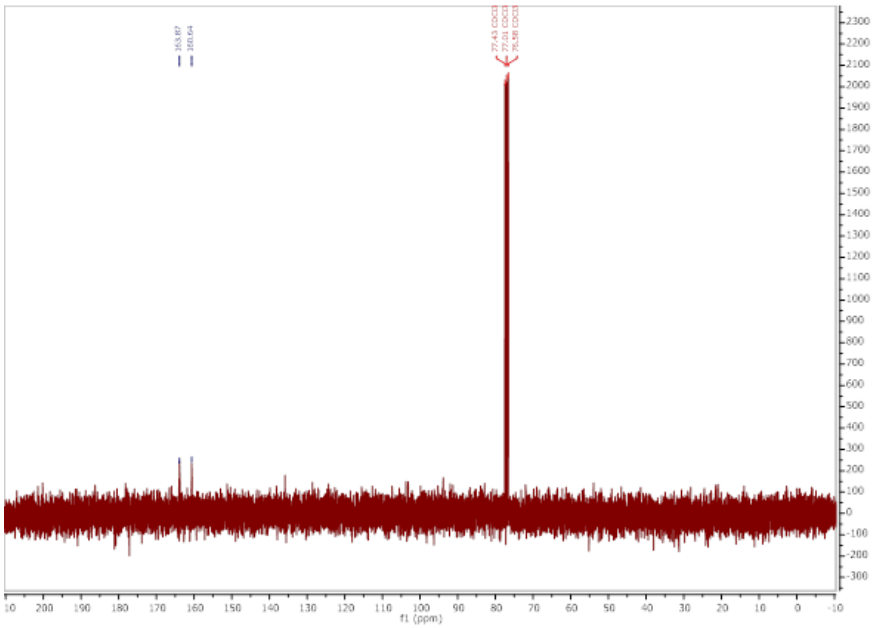

Figure 7.6: ^{13}C–NMR spectrum of 1,3,5-Trifluoro-2,4,6-triiodo-benzene in $CDCl_3$.

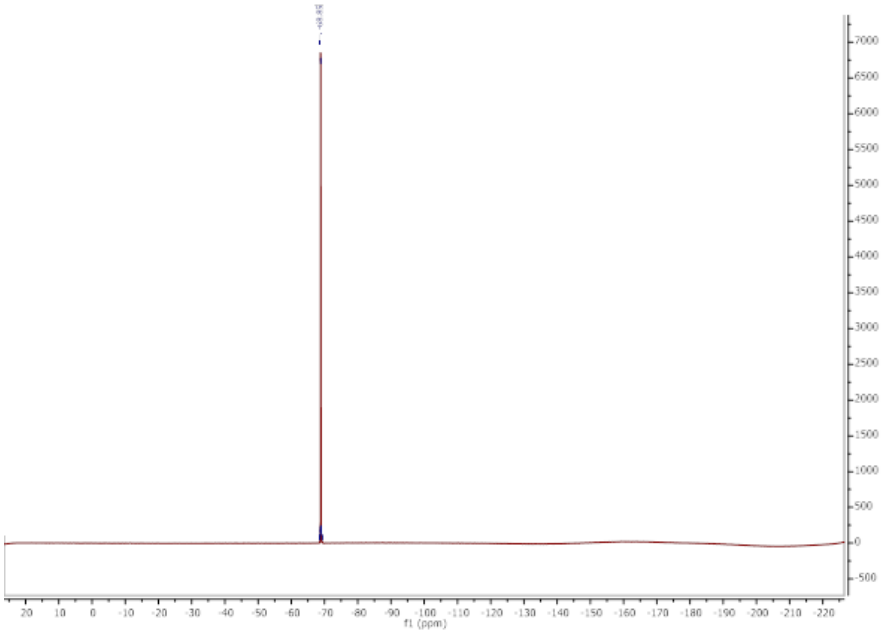

Figure 7.7: ^{19}F–NMR spectrum of 1,3,5-Trifluoro-2,4,6-triiodo-benzene in $CDCl_3$.

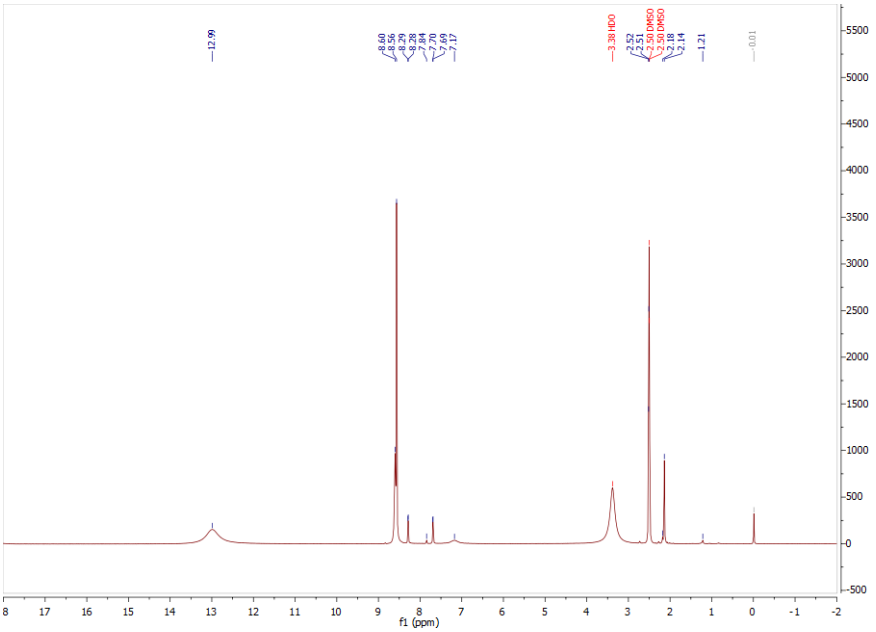

Figure 7.8: ^{1}H–NMR spectrum of NH_2-BTC in DMSO.

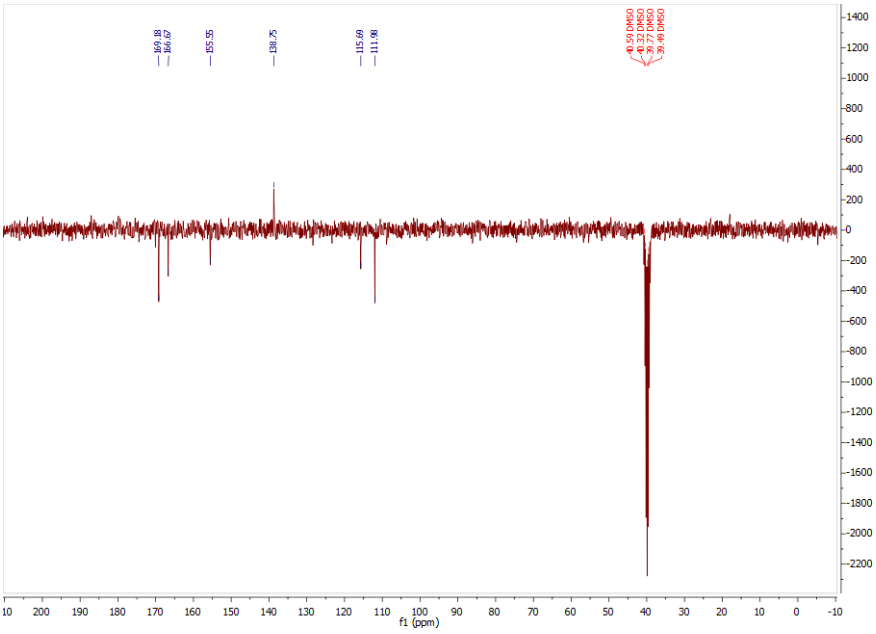

Figure 7.9: ^{13}C–NMR spectrum of NH_2-BTC in DMSO.

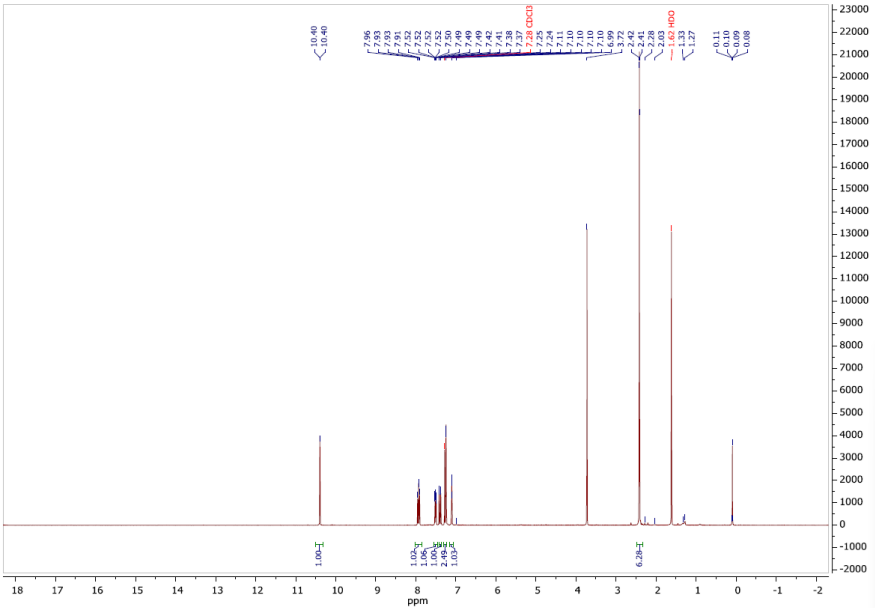

Figure 7.10: ^{1}H–NMR spectrum of 2-Fluoro-3,5-dimethylbenzaldehyde in $CDCl_3$.

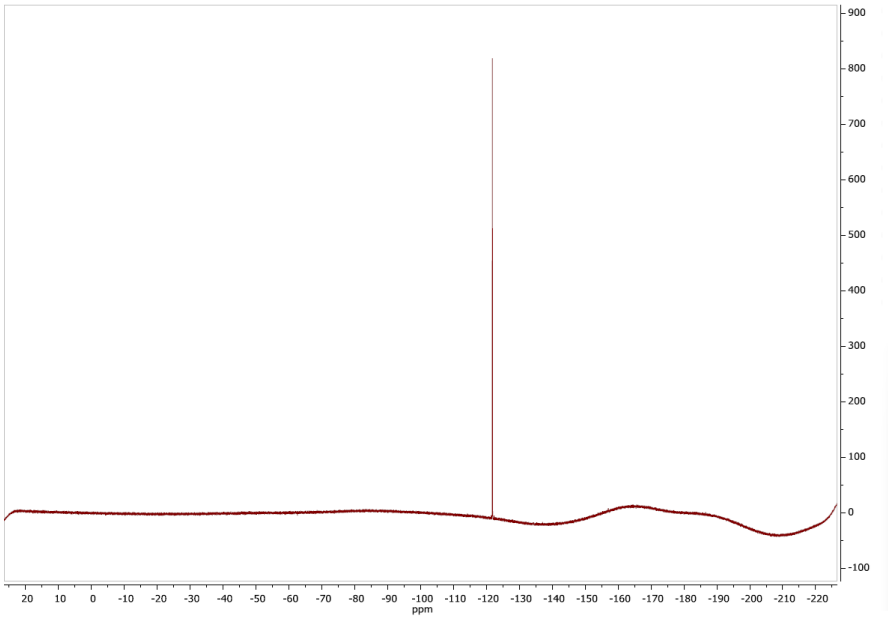

Figure 7.11: ^{19}F–NMR spectrum spectrum of 2-Fluoro-3,5-dimethylbenzaldehyde in $CDCl_3$.

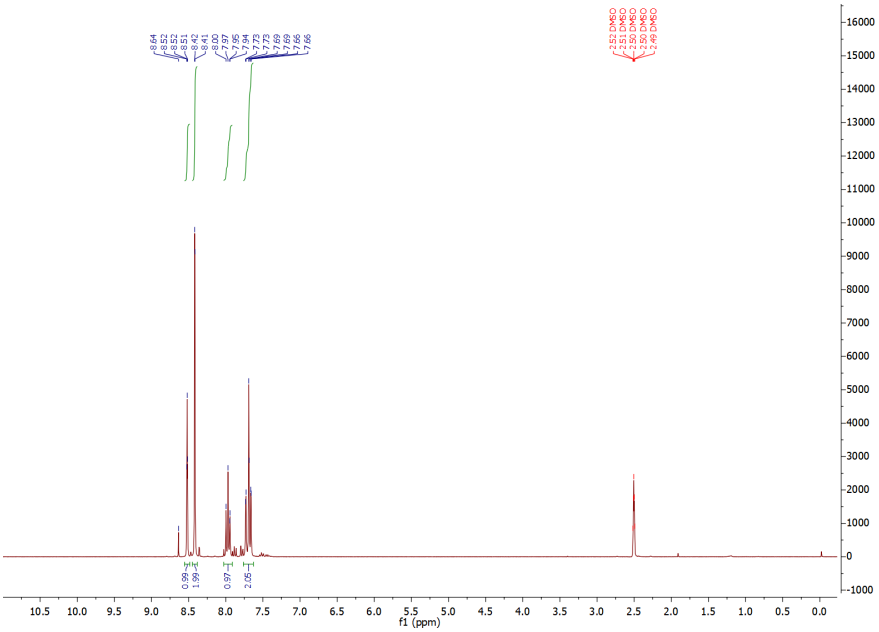

Figure 7.12: ^{1}H–NMR spectrum of 3'-Fluoro-[1,1'-biphenyl]-3,4',5-tricarboxylic acid in DMSO – d_6.

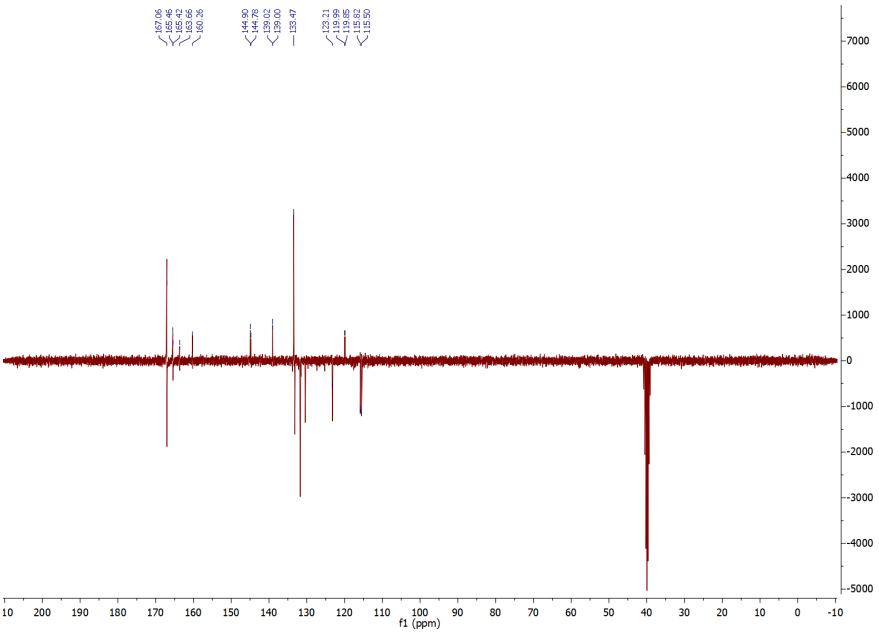

Figure 7.13: ^{1}H–NMR spectrum of 3'-Fluoro-[1,1'-biphenyl]-3,4',5-tricarboxylic acid in DMSO – d_6.

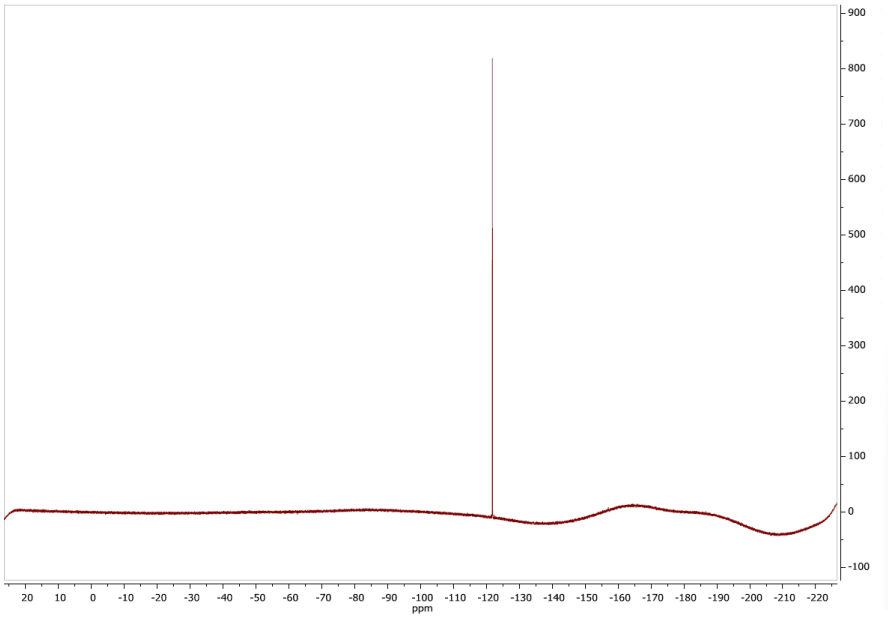

Figure 7.14: ^{19}F–NMR spectrum of 3'-Fluoro-[1,1'-biphenyl]-3,4',5-tricarboxylic acid in DMSO – d_6.

PXRD

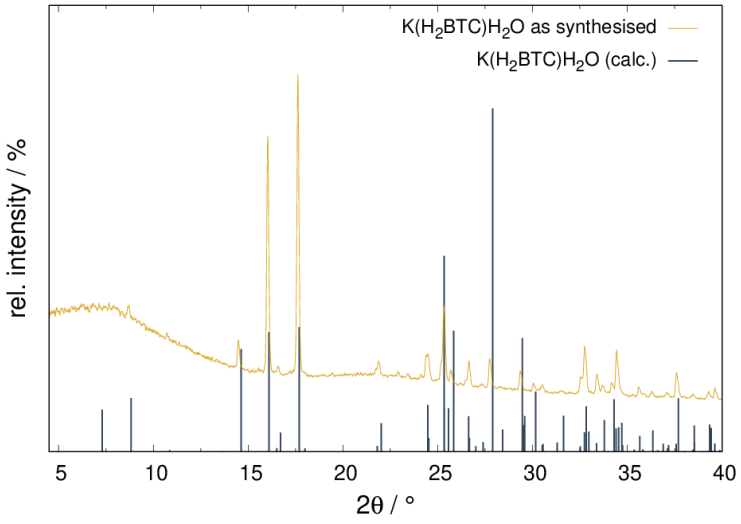

Figure 7.15: Measured powder diffraction pattern of $K(H_2BTC)$ (orange) (298 K, *Rigaku MiniFlex600-C*, flat samples, Cu Kα radiation , $\lambda = 1.54060$ Å). Calculated data taken from *Li et al.*[81]

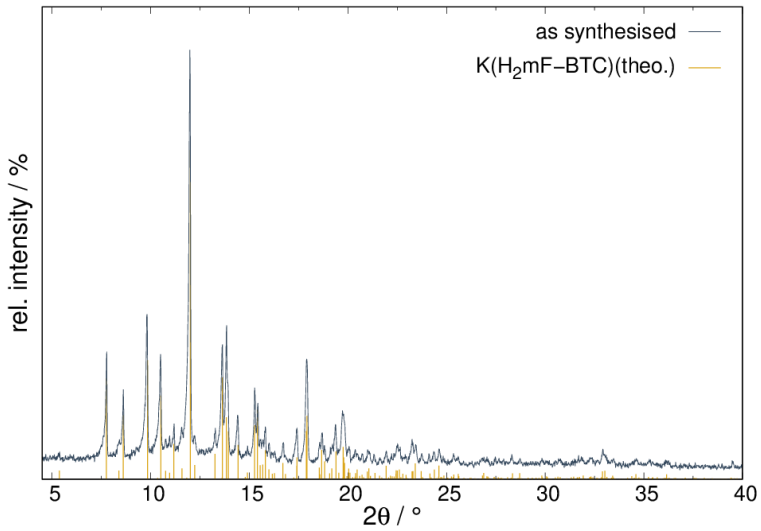

Figure 7.16: PXRD pattern of K(H_2*mF*-BTC) (298 K, *Stoe Stadi P*, Mo Kα_1-radiation (λ = 0.71069 Å).

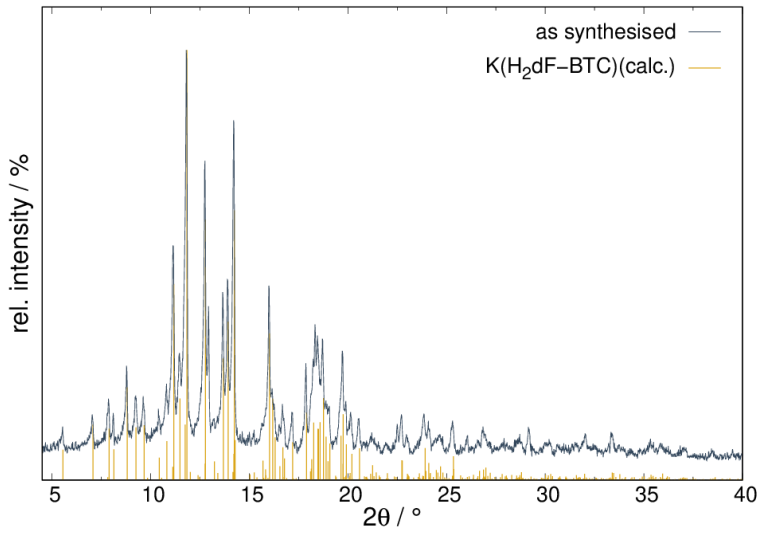

Figure 7.17: PXRD pattern of K(H_2*dF*-BTC) (298 K, *Stoe Stadi P*, Mo Kα_1-radiation (λ = 0.71069 Å).

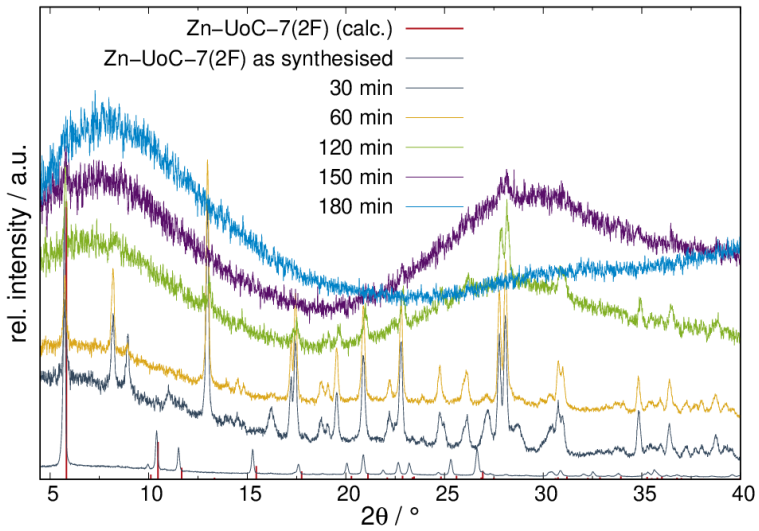

Figure 7.18: PXRD patterns of Zn-UoC-7(2F) after suspension in water for various durations (298 K, *Rigaku MiniFlex600-C*, flat samples, Cu Kα radiation , $\lambda = 1.54060$ Å).

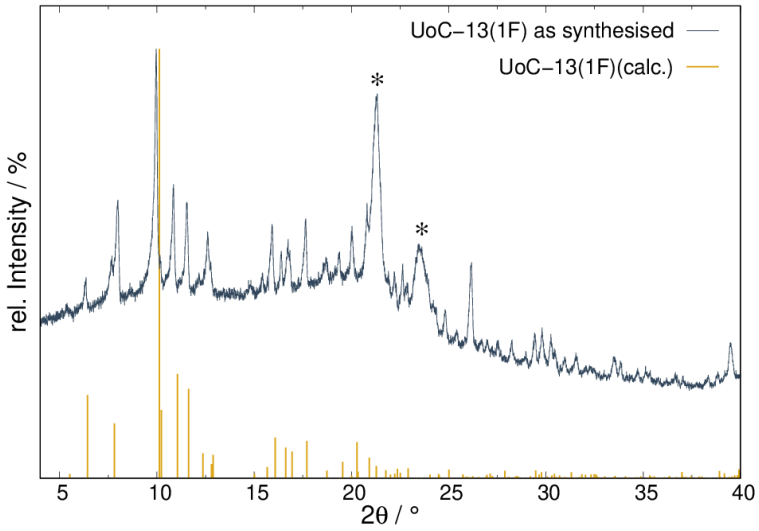

Figure 7.19: PXRD pattern of UoC-13(1F) synthesised in DEF (*Huber G670*, Cu Kα_1 radiation, $\lambda = 1.54060$ Å, *: additional reflections due to the foil of the sample holder).

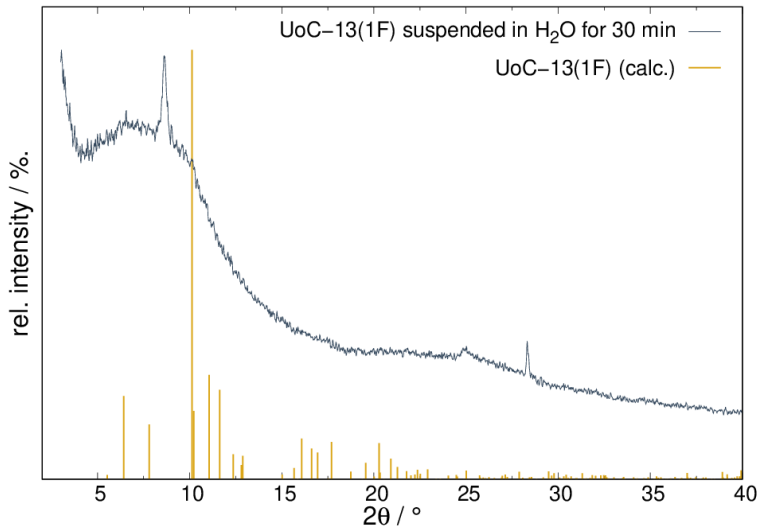

Figure 7.20: PXRD pattern of UoC-13(1F) after suspension in water for 30 min (*Huber G670*, Cu Kα_1 radiation, $\lambda = 1.54060$ Å, *: additional reflections due to the foil of the sample holder).

DSC/TGA/MS

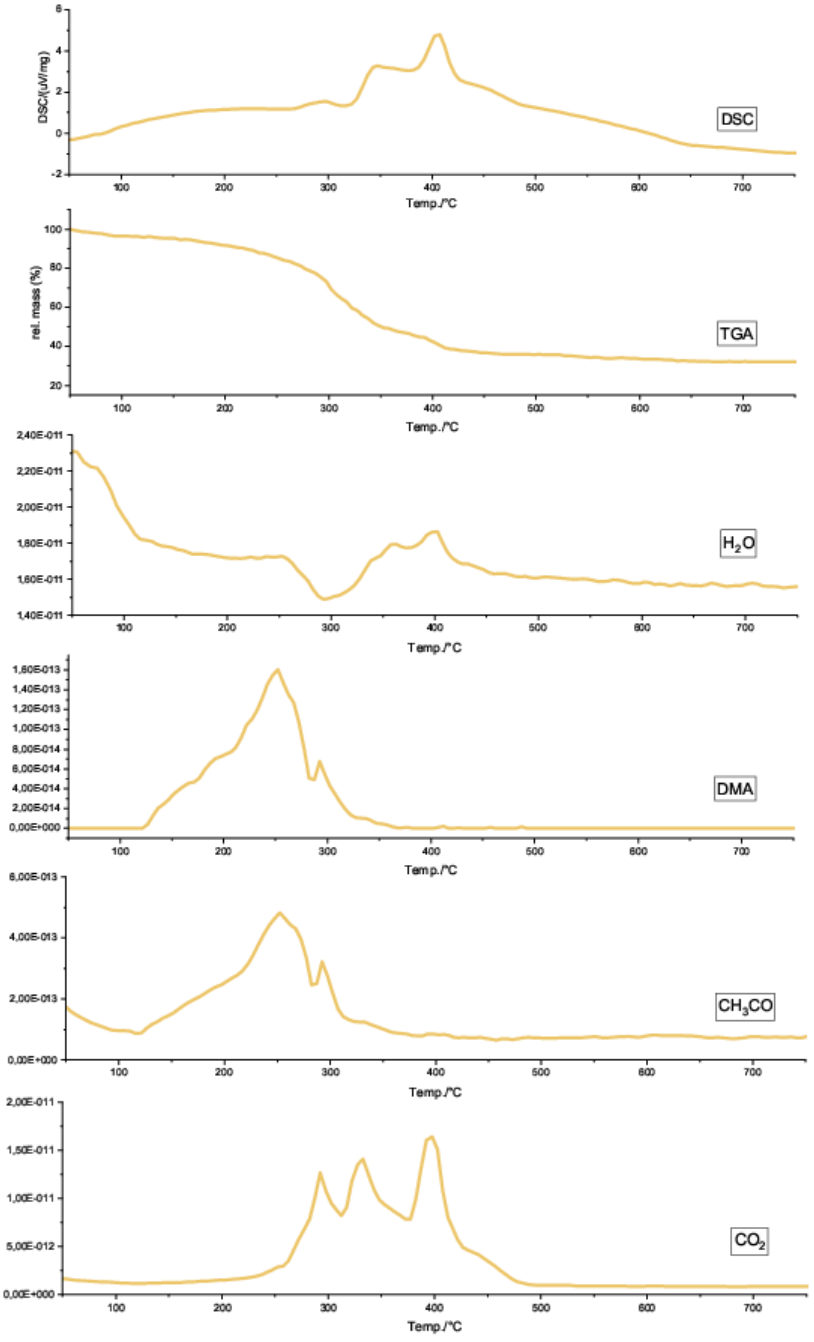

Figure 7.21: Coupled DSC-TGA-MS analysis of Zn-UoC-7(2F).

DTG

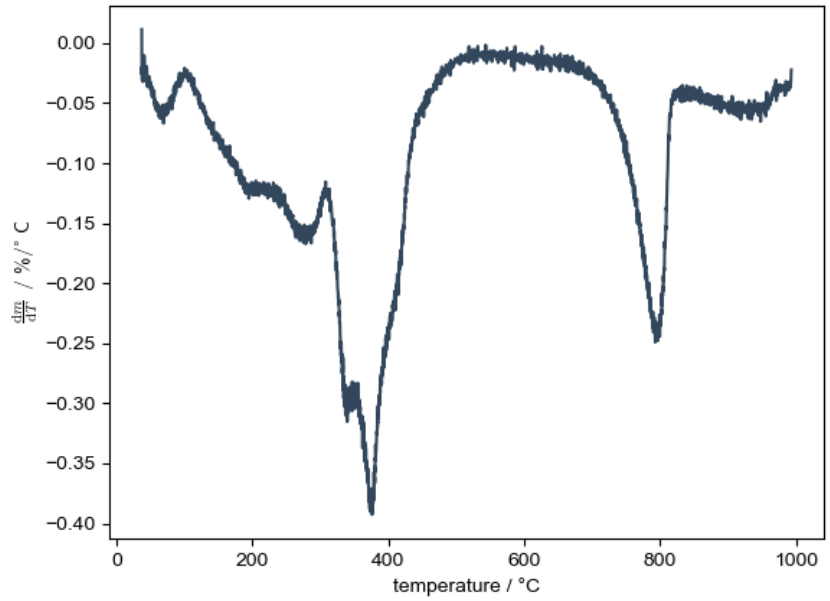

Figure 7.22: DTG curve of Zn-UoC-7(1F).

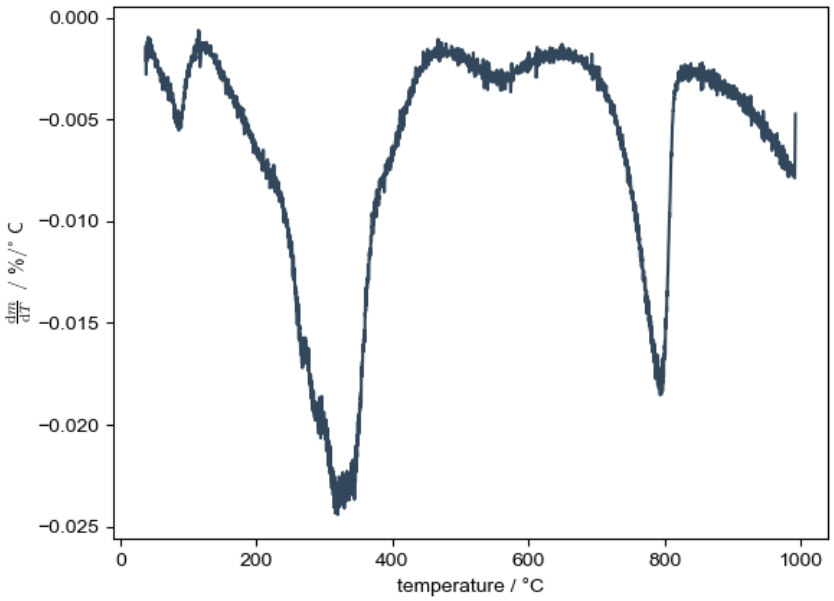

Figure 7.23: DTG curve of Zn-UoC-7(2F).

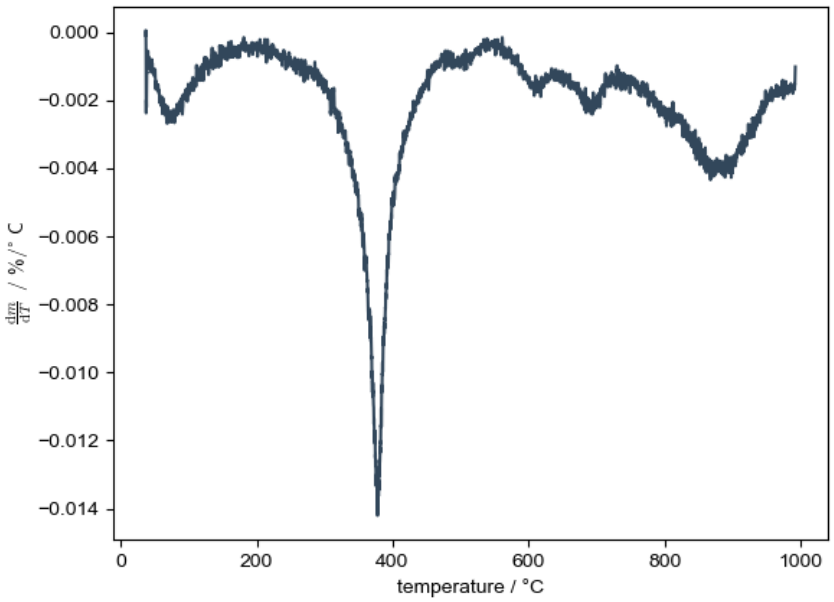

Figure 7.24: DTG curve of UoC-13(1F).

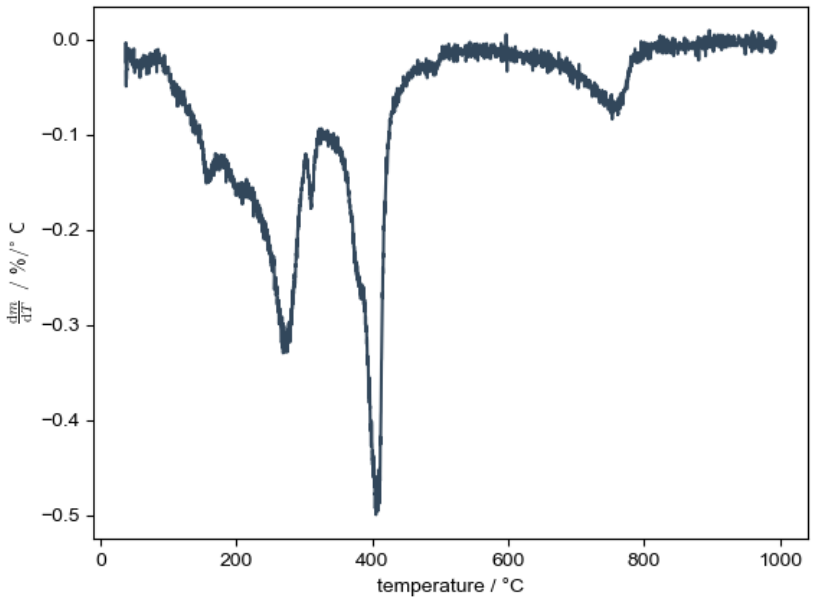

Figure 7.25: DTG curve of Cu,Zn-UoC-5(1F).

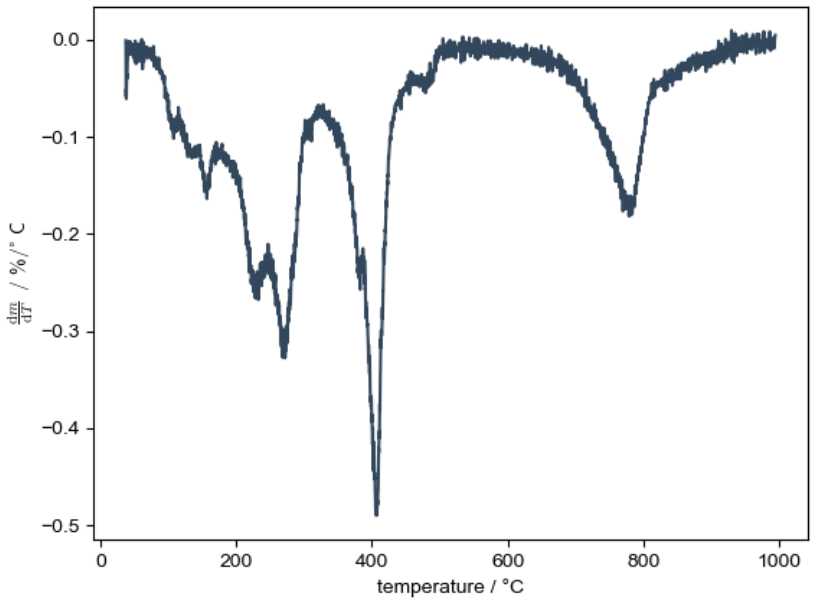

Figure 7.26: DTG curve of Cu,Zn-UoC-5(2F).

BET

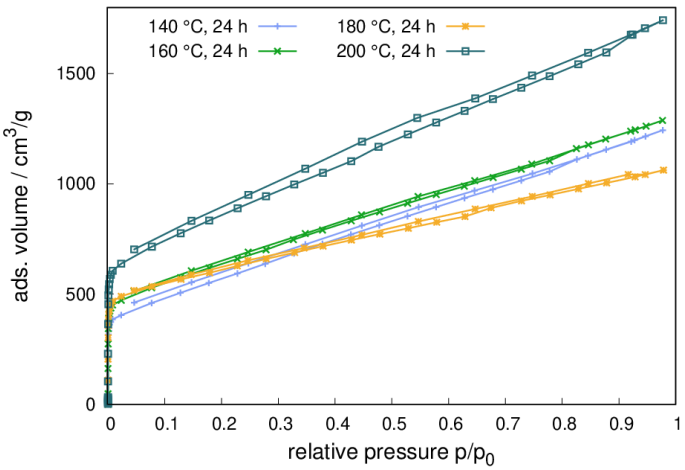

Figure 7.27: N_2 sorption isotherms of Zn-UoC-7(1F) measured at 77 K after activation at different temperatures for 24 h in high vacuum.

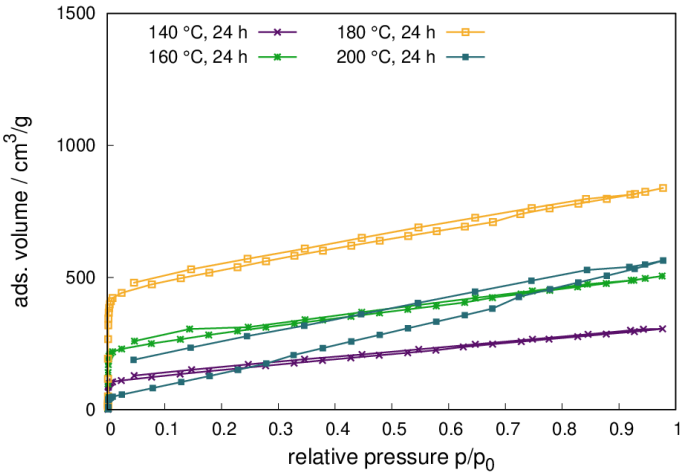

Figure 7.28: N_2 sorption isotherm of Zn-UoC-7(2F) measured at 77 K after activation at different temperatures for 24 h in high vacuum.

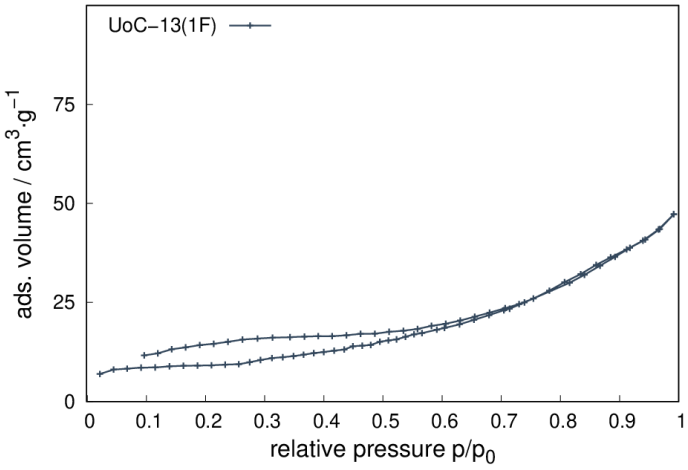

Figure 7.29: N_2 sorption isotherms of UoC-13(1F) measured at 77 K after activation at 120 °C for 24 h in high vacuum.

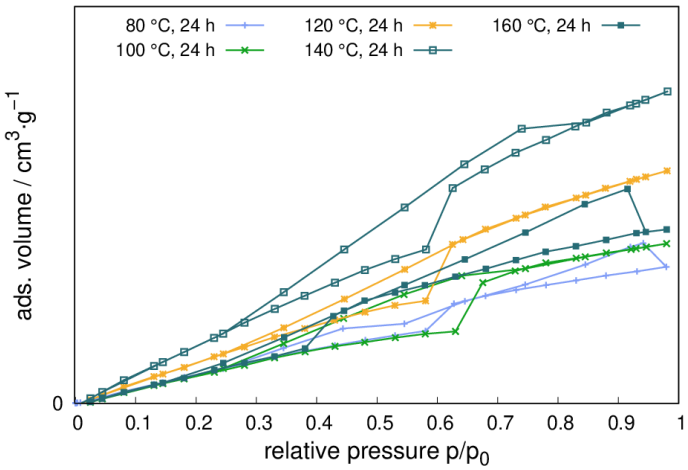

Figure 7.30: N_2 sorption isotherms of GaMOF-1(NH_2) measured at 77 K after activation at different temperatures for 24 h in high vacuum.

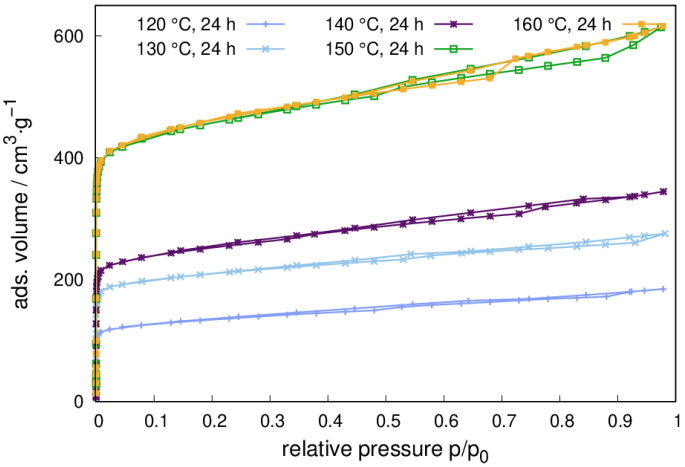

Figure 7.31: N_2 sorption isotherms of Cu,Zn-UoC-5(1F) measured at 77 K after activation at different temperatures for 24 h in high vacuum.

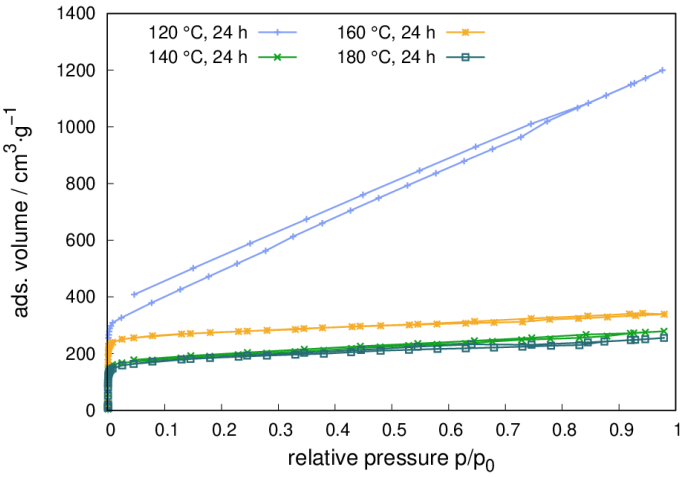

Figure 7.32: N_2 sorption isotherms of Cu,Zn-UoC-5(2F) measured at 77 K after activation at different temperatures for 24 h in high vacuum.

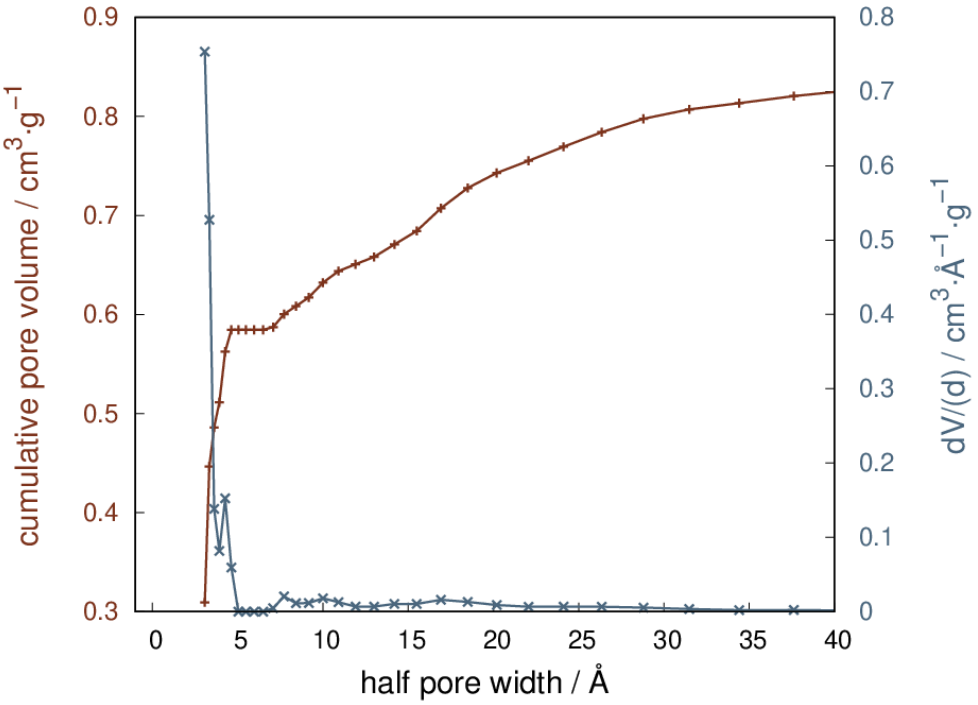

Figure 7.33: Pore size distribution of Cu,Zn-UoC-5(1F).

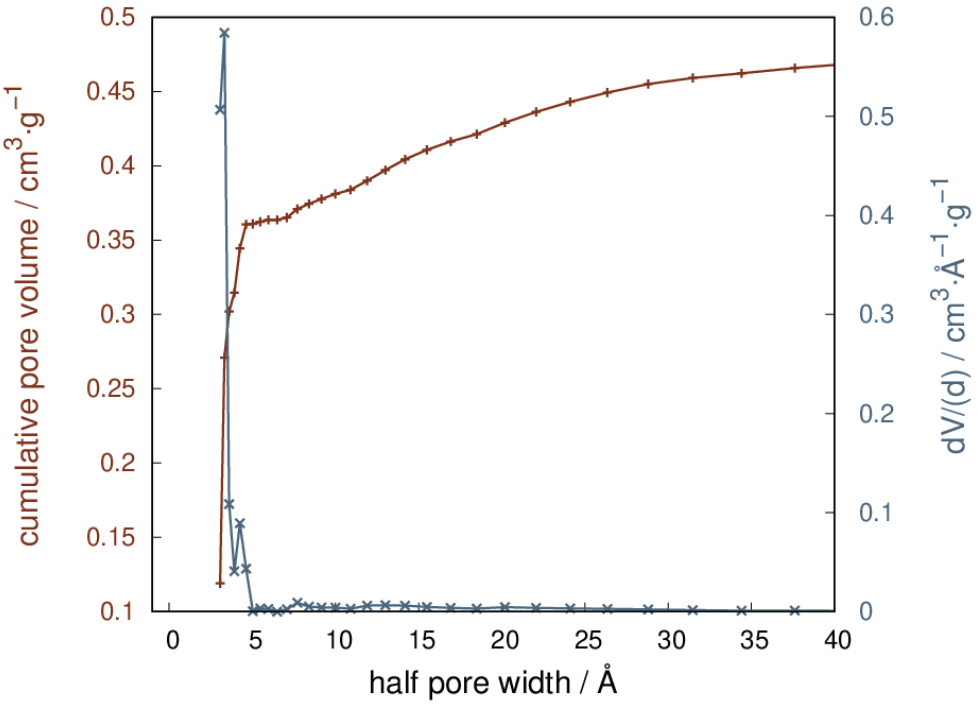

Figure 7.34: Pore size distribution of Cu,Zn-UoC-5(2F).

SCXRD

Table 7.1: Selected crystallographic data of $^{3}_{\infty}[Zn_3(mF\text{–}BTC)_2(DMA)_3]$ taken from a previous bachelor's thesis[103] and of $^{3}_{\infty}[Zn_3(mF\text{–}BTC)_2(DMA)_3]$.

	$^{3}_{\infty}[Zn_3(mF\text{–}BTC)_2(DMA)_3]$[103]	$^{3}_{\infty}[CoZn_2(mF\text{–}BTC)_2(DMA)_3]$
Crystal system	monoclinic	monoclinic
Space group (no.), Z	P 21/n (14), 4	P 21/n (14), 4
Lattice parameter		
a / Å	12.459(5)	12.0022(11)
b / Å	12.984 (5)	13.1723(12)
c / Å	27.674 (5)	27.0801
β / °	93.467(5)	92.847(3)
V / Å^3	4469(6)	4389.8(7)
R_{int}	n.s.	0.0601
R_1	0.2301	0.0865
wR_2	0.3933	0.3036
GooF	1.039	1.304

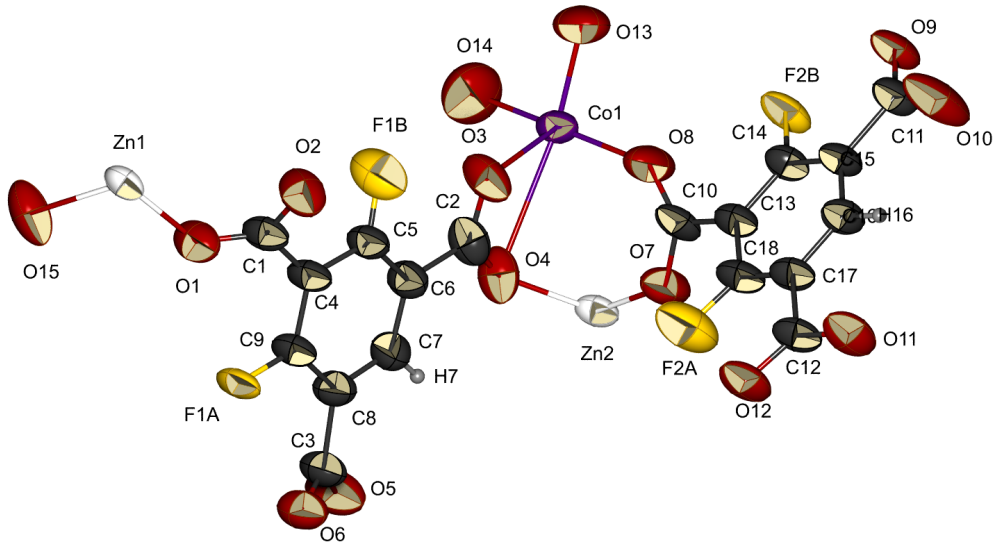

Figure 7.35: Asymmetric unit of $^{3}_{\infty}[CoZn_2(mF\text{–}BTC)_2(DMA)_3]$ with thermal ellipsoids drawn at the 50 % probability level. Colour code: Zn (white), Co (purple), O (dark red), C (black), F (yellow), and H (light grey).

Acknowledgments

Wenn ich eines gelernt habe, dann, dass Wissenschaft nicht im Alleingang betrieben wird. In diesem Sinne möchte ich all jenen danken, die mich bei der Erstellung dieser Arbeit begleitet und unterstützt haben.

Zunächst möchte ich meinem Doktorvater, *Prof. Dr. Uwe Ruschewitz*, meinen tief empfundenen Dank aussprechen. Ich schätze es sehr, dass ich die Möglichkeit hatte, meine Dissertation in seinem Arbeitskreis zu verfassen. Sein kontinuierliches fachliches und persönliches Feedback hat sowohl mich als auch diese Arbeit maßgeblich geprägt und wachsen lassen.

Mein besonderer Dank gilt ebenfalls *Prof. Dr. Mathias Wickleder* für die freundliche Übernahme des Zweitgutachtens.

Für die Übernahme des Amtes der Prüfungsvorsitzenden bei meiner Disputation spreche ich meinen herzlichen Dank *Prof.'in Dr. Katharina Groß* aus. Ebenso danke ich *Dr. Corinna Hegemann* für die Protokollführung.

Mein Dank außerdem gilt der NMR- und Röntgenabteilung der Universität zu Köln. Besonders möchte ich mich bei *Dr. Ingo Pantenburg*, *Silke Kremer*, *Dr. Jörg Neudörfl* und *Daniel Moog* für die Aufnahme von Röntgenpulverdiffraktogrammen und für die Einkristallmessungen bedanken. Ebenfalls für die Aufnahmen von Röntgenpulverdiffraktogrammen möchte ich *Dr. Daniel Smets*, *Dr. Markus Krüger*, *Sean S. Sebastian* und *Tim Mattick* meinen herzlichen Dank aussprechen. Bei *Sean S. Sebastian* und *Tim Mattick* möchte ich mich außerdem für Berechnungen bedanken, insbesondere der Hirschfeld-Analyse bzw. den Enthalpie-Rechnungen für UoC-7.
Ein weiteres Dankeschön geht an *Dirk Pullem* für die Elementaranalysen sowie an *Dr. Christian Tobeck*, *Lisa Körtgen* und *Tim Kleinöder* für die Unterstützung bei den DSC/TGA-Messungen. Für die DSC/TG/MS-Messung danke ich herzlichst *Tobias Rennebaum* und für die XPS-Messungen *Dr. Michael Wilhelm*. Außerdem gebührt *Ronja Christoffels* und *Aimée E. Cammiade* ein Dank für die Sorptions-Messungen.

Meinen engagierten Praktikant*innen *Katrin Eppers*, *Daria Iakovleva*, *Diana Obretenova* und *Charline Aubourg* für ihre Mitarbeit während ihrer Forschungspraktika bedanken. Ihr Engagement und ihre harte Arbeit haben mich im Rahmen dieser Arbeit sehr unterstützt.

Darüber hinaus möchte ich mich bei *Peter Müller, Thomas Dautert, Robert Hempel, Franz Röttgen* und *„Johnny" Demirbilek*, sowie den Mitarbeiter*innen der Chemikalienausgabe und der Glasbläserei für ihre Unterstützung im Arbeitsalltag bedanken.

Von Herzen danke ich *Aimée E. Cammiade, Caroline Hoverath, Tim Mattick, Tim Kleinöder, Ronja Christoffels, Sean S. Sebastian, Lisa Körtgen, Robert Vigelius, Dr. Alisha Mertens, Dr. Christian Tobeck, Dr. Markus Krüger, Dr. Marc Hetzert* und *Helena Wenzel* für das gewissenhafte Korrekturlesen dieser Arbeit. Euer Feedback, die wertvollen fachlichen Diskussionen und die vielen unterhaltsamen Gespräche haben nicht nur mein Wissen bereichert, sondern mir auch stets ein Lächeln ins Gesicht gezaubert.

Mein tiefster Dank gilt dem gesamten Arbeitskreis – sowohl den ehemaligen als auch den aktuellen Mitgliedern – und darüber hinaus auch den Nachbararbeitskreisen *Wickleder*, *Klein* und *Mathur*. Die gemeinsame Zeit mit euch war nicht nur arbeitsintensiv, sondern geprägt von herzlichen Freundschaften, die weit über das berufliche Miteinander hinausgehen. Jede*r von euch hat auf wunderbare Weise zu dieser Arbeit beigetragen. Durch die unzähligen gemeinsamen Stunden – ob am Arbeitsplatz oder in privaten Momenten – sind wertvolle Freundschaften entstanden, die ich über alles schätze.

Besonders möchte ich mich bei *Marc* und *Ronja*; mit euch hat diese Reise erst richtig angefangen.

Dann danke ich meinem Laborpartner *Daniel* und *Sean*, nicht nur für unzählige fachliche Gespräche, sondern auch für eure Spotify-Playlisten, mit denen sich die Laborarbeit oft wie eine riesige Party angefühlt hat.

Dann danke ich von ganzem Herzen meinen lieben Freund*innen im Frontoffice. Danke, dass ihr mir in den stressigen Phasen des Schreibens immer wieder ein offenes Ohr geschenkt habt. Ihr habt mir Mut gemacht und mich motiviert, immer weiterzumachen. In diesem Sinne danke ich besonders dir, *Aimée*, für deine immer passenden Worte. Du hast mir mit ihnen viele Tränen getrocknet. Ich danke dir, *Tim*, dass du mir das Zählen bis zehn beigebracht hast und meine emotionalen Gedanken das ein oder andere Mal ins

rechte Licht gerückt hast. Ein besonderes Dankeschön geht an dich, *Caro*, für unsere unvergesslichen Taylor-Swift-Late-Night-Sessions – sie haben mich durch so manche lange Nacht begleitet. Und *Robert*, du kannst jetzt deinen Monitor wiederhaben – danke!

An alle weiteren Freunde und an meine Familie, danke, dass ihr mich während meines Studiums und meiner Promotion immer unterstützt habet.
Ein besonders großer Dank gilt *Alisha, Feray, Alex, Valeria, Micha, Eray, Buki, Ilyas, Niewen, Tugce* und *Mira*. Ihr seid die Familie, die ich mir selbst ausgesucht habe! Ihr habt mir immer mit Rat und Tat zur Seite gestanden, und ich danke euch von Herzen für eure Hilfe, eure Ermutigung und die vielen kostbaren Stunden, die wir sowohl innerhalb als auch außerhalb der Universität miteinander verbringen durften. Eure Präsenz hat mein (Uni-)Leben bereichert.

Ein ganz besonderer Dank geht außerdem an *Valle* und *Ilyas* für unser gemeinsames erstes Semester und an *Alex* und *Feray*, dass ich mit euch gemeinsam erwachsen werden durfte. Ohne euch wäre ich sicherlich nicht die Person, die ich heute bin.

Danke *Basti*, dass du mir zum Abschluss meiner Promotion den Rücken frei gehalten hast, sodass ich mich auf diese Arbeit konzentrieren konnte.

Zum Schluss danke ich meiner Schwester *Helena* und meinen Eltern *Linda* und *Karl*. Danke, *Heli*, dass du immer für mich da bist, wenn ich dich brauche. Es gibt sicherlich kein Universum, in dem wir nicht Schwestern oder beste Freundinnen sind.

Meine Eltern verdienen meinen tiefsten Dank für ihre unerschütterliche und liebevolle Unterstützung in jeder Situation und Lebenslage. Eure Liebe, Fürsorge und euer Vertrauen haben mir geholfen, diesen Weg zu beschreiten.

Danke!

Erklärung zur Dissertation

gemäß der Promotionsordnung vom 12. März 2020

Hiermit versichere ich an Eides statt, dass ich die vorliegende Dissertation selbstständig und ohne die Benutzung anderer als der angegebenen Hilfsmittel und Literatur angefertigt habe. Alle Stellen, die wörtlich oder sinngemäß aus veröffentlichten und nicht veröffentlichten Werken dem Wortlaut oder dem Sinn nach entnommen wurden, sind als solche kenntlich gemacht. Ich versichere an Eides statt, dass diese Dissertation noch keiner anderen Fakultät oder Universität zur Prüfung vorgelegen hat; dass sie - abgesehen von unten angegebenen Teilpublikationen und eingebundenen Artikeln und Manuskripten - noch nicht veröffentlicht worden ist sowie, dass ich eine Veröffentlichung der Dissertation vor Abschluss der Promotion nicht ohne Genehmigung des Promotionsausschusses vornehmen werde. Die Bestimmungen dieser Ordnung sind mir bekannt. Darüber hinaus erkläre ich hiermit, dass ich die Ordnung zur Sicherung guter wissenschaftlicher Praxis und zum Umgang mit wissenschaftlichem Fehlverhalten der Universität zu Köln gelesen und sie bei der Durchführung der Dissertation zugrundeliegenden Arbeiten und der schriftlich verfassten Dissertation beachtet habe und verpflichte mich hiermit, die dort genannten Vorgaben bei allen wissenschaftlichen Tätigkeiten zu beachten und umzusetzen. Ich versichere, dass die eingereichte elektronische Fassung der eingereichten Druckfassung vollständig entspricht.

Teilpublikationen:
S. Wenzel, A. E. L. Cammiade, R. K. Christoffels, S. S. Sebastian, T. Mattick, U. Ruschewitz, *Chem. Eur. J.* **2024**, *30*, e202400445. `https://doi.org/10.1002/chem.202400445`.

02.09.2024, Susanna Wenzel
Datum, Name und Unterschrift